Flow Characteristics of a Bubbling Fluidized Bed with Nonspherical Particles

A dissertation submitted to

Gunma University / University of Chinese Academy of Sciences

in partial fulfillment of the requirement

for the degree of

Doctor of Philosophy

in Mechanical Engineering and Technology

By

Chuanpeng Zhang (T192B602)

Supervisor : Professor Wei Wang

Professor Tomohiko Furuhata

Assist Supervisor : Associate Professor Yanpei Chen

Gunma University, Japan

Institute of Process Engineering, Chinese Academy of Sciences

May 2023

Authorization Statement for Thesis/Dissertation Use

I understand and abide by the regulations of the Gunma University regarding the preservation and use of theses/dissertations, i.e. the Gunma University has the right to preserve the copies of students' theses/dissertations, allow the theses/dissertations to be consulted, publish all or part of the theses/dissertations in accordance with the principles of openness in academic research and protection of intellectual property rights, and preserve and compile the theses/dissertations by photocopying, reprinting in a reduced format or other means of reproduction. This statement shall apply to classified and delayed theses/dissertations after the declassification or delay period.

Signature of the author：　　Date：

Signature of the supervisor：　　Date：

Abstract

Among the various types of fluidized beds, bubbling fluidized beds have long been a focus for both practical applications and theoretical research. In practical applications, particles in a bubbling fluidized bed are usually nonspherical in shape. Nonspherical particles have a significant impact on the gas-solid flow characteristics in the bed compared to spherical particles. However, traditional research methods often assume that particles in a bubbling fluidized bed are spherical to simplify calculations. This assumption fails to accurately represent the fluidization behavior of particles in the system, which seriously affects the design, optimization, and actual operation of the fluidized bed reactor. Therefore, studying the dynamic characteristics of gas-solid two-phase flow of nonspherical particles in bubbling fluidized beds is crucial. In this study, we employed experimental methods to investigate the gas-solid two-phase hydrodynamic characteristics of nonspherical particles in a bubbling fluidized bed.

In this study, we constructed a bubbling fluidized bed experimental system and used rod-like particles with nonspherical characteristics as the research object. Our main objective was to investigate the effects of particle shape and superficial gas velocity on the dynamic characteristics of gas-solid two-phase fluid. The main contents and results of this paper are as follows:

(1) As the particle shape deviates gradually from the spherical, particles tend to form a channeling flow instead of a smooth transition to the bubbling fluidization. The minimum velocity and bed expansion rate initially decrease and subsequently increase with an increase in the aspect ratio. The vertical velocity profiles are sensitive to the aspect ratio at low gas velocity, but not sensitive at high gas velocity. The velocity distribution, especially the rotational velocity distribution, deviates from the Maxwellian distribution.

(2) We identify two high-probability particle configurations, two particles in a parallel or vertical arrangement, by calculating the radial distribution function, nematic correlation function and coordination number. We further explain the cause of this order appearance through entropy theory. By comparing the drag force of the above two configurations at various angles and Re, we demonstrate that it is necessary to put forward a configuration-dependent drag force for nonspherical particle fluidization.

(3) This study examines the impact of particle shape and superficial gas velocity on bubble dynamics and identifies that particle configuration affects the movement and development of bubbles. Specifically, the rising of bubbles is found to first break the particle configuration, causing the particles to rotate towards their preferred direction. Above the bubble, particles tend to be horizontally oriented, while on either side, they tend to be vertically oriented. Furthermore, compared to spherical particles, rod-like

particles exhibit a larger bubble aspect ratio and a lower bubble velocity.

In summary, the fluidization characteristics of nonspherical particles were studied in this paper, and the macro-scale characteristics of nonspherical particles was revealed from the aspects of pressure drop, minimum fluidization velocity and bed expansion rate. The study also examined the particle flow characteristics by particle velocity, orientation, particle kinetic energy, and granular temperature, and the interlocking phenomenon inside the bed, with the radial distribution function and order parameters used to identify two types of particle configurations and to quantitatively analyze the dynamics of particle configuration. Furthermore, an analysis of the drag force of different particle configurations indicated that the particle shape significantly affects the drag force and thus the flow characteristics of nonspherical particles. Additionally, the study highlighted the significant influence of the particle shape on bubble dynamics. Collectively, these findings are helpful to reveal the fluidization characteristics of nonspherical particles and promote the understanding of the mechanism of gas-solid flow characteristics of rod-like particles, thus provide a guidance for the design, optimization, and control of fluidized beds.

Key Words: Rod-like particle; Particles configuration; PTV; Experiment; Gas-solid two phase flow

Table of Contents

Figure List

Table List

Annotations of Symbols

Symbols	Annotations
$A_{\perp}$	The projected face area
C_d	The drag efficient
d_p	Particle diameter
d_v	Equal volume equivalent diameter
d_s	Equal surface area equivalent diameter
d_{sv}	Equivalent surface area equivalent diameter
$\mathrm{E_r}$	The rotational kinetic energy
$\mathrm{E_t}$	The translational kinetic energy
F_c	Time fraction
f_c	The super-particles frequency
F_d	The drag force
g(r)	Radial distribution function
g	The gravity acceleration
$G_2(r)$	The local nematic-order correlation function
G_4	The tetraic-order correlation function
h_S	Height
H	Bed height
H/H_{mf}	Bed expansion ratio
k	A slope
$\mathrm{I_p}$	The particle moment of inertia
l_p	Particle length

Symbols	Annotations
$\mathrm{m_p}$	The particle mass
N	The number of particles
N_c	The number of super-particles
n_c	The particle number contained in a super-particles
Re	The reynolds number
r_{ij}	The distance between particles i and j
$\mathrm{S}_{i,t}$	Particle location
S_2	The global nematic-order correlation function
S_p	The surface area of the particle
t	Time
t_i	The existence time of super-particles i
u	The gas velocity
U_{mf}	The minimum fluidization velocity
U_{mb}	The minimum bubbling velocity
v	The instantaneous velocity
$\bar{v}$	The average velocity
$\mathrm{V_r}$	Particle rotation velocity
v_{RMS}	Rms of the particle velocity
V	Volume
V_{ex}	Excluded volume
v_c	Super-particles velocity
V_B	Bubble volume
V_b	Bubble velocity
$\mathrm{T_t(t)}$	The translational granular temperatures

Symbols	Annotations
$T_r(t)$	The rotational granular temperatures
y_i	The vertical coordinate of the centre of mass of particle i

Greek symbols	Annotations
Δt	Time step
ΔP	The pressure drop
ΔP_0	The effective pressure drop
ε	Voidage fraction
ρ_0	The average number of rod-particles per unit area
ξ_2	The order correlation length
$\emptyset_{\parallel}$	The lengthwise sphericity
$\emptyset$	The particle sphericity
$\emptyset_{\perp}$	The crosswise sphericity
χ	Aspect ratios
χ_b	The aspect ratio of the bubble
ε_{s0}	The particle concentration at the initial accumulation
ρ_s	The particle density
φ	The angle between the long axis of the particle and the direction of the airflow
θ_i	The angles of particles i
σ	The standard deviation of the increasing pressure drop

Symbols	Annotations
ψ_N	Particle number fraction
Subscripts	
p	Particle
x	Horizontal
y	Vertical
r	Rotational
t	Translational
mf	Minimum fluidization
Abbreviation	
CFD-DEM	Computational fluid dynamics-discrete element method
PTV	Particle tracking velocimetry
DIA	Digital image analysis
MPT	Magnetic particle tracking
PEPT	Positron emission particle tracking
RPT	Radioactive particle tracking
PIV	Particle image velocity
XPTV	X-ray particle tracking velocimetry

1 Introduction

1.1 Background and significance

Gas-solid fluidization[1,2] is an essential branch of chemical engineering technology which plays a very important role in industrial processes such as in food, chemistry, medicine, metallurgy, coal and petroleum industries[3-7]. To optimize the design and operation of these industrial processes, the flow behavior in fluidized beds have been studied extensively[8-10]. The assumption made in the majority of studies on the fluidization properties of fluidized beds is that the particles are spherical[11-13] for the sake of simplicity. However, particles in realistic industrial processes, such as biomass combustion and gasification[14,15], granulation[16,17], and fluid catalytic cracking in petrochemical refinerys[18], are nonspherical. In particular, application of the biomass, such as wood chips, wood pellets, and straws characterized by elongated particles[19], can reduce the greenhouse gas CO_2 emissions[20], and thus has attracted increasing attention from scholars in many fields. The biomass combined heat and power has emerged as a significant heating approach in Europe, the United States, and other regions. Therefore, the research on the flow characteristics of nonspherical particles has important significance in both theoretical and practical senses.

In principle, the complex fluidization behavior of nonspherical particles can be

attributed to their complex dependence on inter-particle interactions (say, the stress and interlocks between particles) and particle-fluid interactions[21-24] (say, the drag force).The two-phase flow, mass and heat transfer and chemical reactions over nonspherical particles diffe greatly from those of spherical ones[24,25]. On the one hand, due to the effects of the particle shape, the interparticle interaction becomes more complicated. There may be various contact situations between points, lines, and surfaces when nonspherical particles come into contact. On the other hand, nonspherical particles show a variety of heterogeneity and orientations in fluids because of the interaction between non-spherical particles and fluids. In addition, the particle configuration arises inside the bed as a result of the the anisotropic shape of nonspherical particles. Here, particle configuration refers to a specific set and spatial arrangement of particles. The interparticle or particle-fluid interactions underlying various configurations of nonspherical particles may lead to complex fluidization behavior, e.g., interlocking[26] and channeling[24], beyond typically encountered bubbling[27-31]. So, quantitative analysis of such configurations of nonspherical particles is fundamental to understanding the underlying mechanism of complex fluidization behavior of nonspherical particles, although relevant researches are rather few. The shape characteristics of nonspherical particles affect the gas-solid flow structure in a fluidized bed, and will inevitably affect the heat and mass transfer and chemical

reactions between the particle-particle or the particle-fluid.

Currently, simulations and experiments of nonspherical-particle fluidized beds are still in a early research stage. Further researches about the internal mechanism of gas-solid two-phase flow of nonspherical particles are in urgent need. In particular, the particle-level dynamic characteristics of nonspherical particles in a dense gas-solid two-phase flow are needed, which is helpful for the design, operation and optimization of gas-solid fluidized bed reactors. In this work, rod-like, nonspherical particles are chosen to be fluidized, as they are widely encountered in energy, chemical and pharmaceutical industries such as the biomass combustion and gasification, plastic pellet processing and pesticide pellets preparation processes[32-35].

1.2 Fluidization

Fluidization is a unit operation in which solid particles behave like fluids when a stream of gas or liquid flows upwards through solid particles, causing them to be lifted and suspended[36]. The fundamental characteristic of two-phase flow is the coexistence of the particle-rich dense phase and the fluid-rich dilute phase. An increase in gas velocity causes a noticeable change in the flow regime in a fluidized bed. Fluidization can be broadly categorized into the following flow regimes, including the delayed bubbling or fixed bed, bubbling regime, slugging regime, turbulent regime, fast

fluidization, and pneumatic conveying, as shown in Figure 1.1.

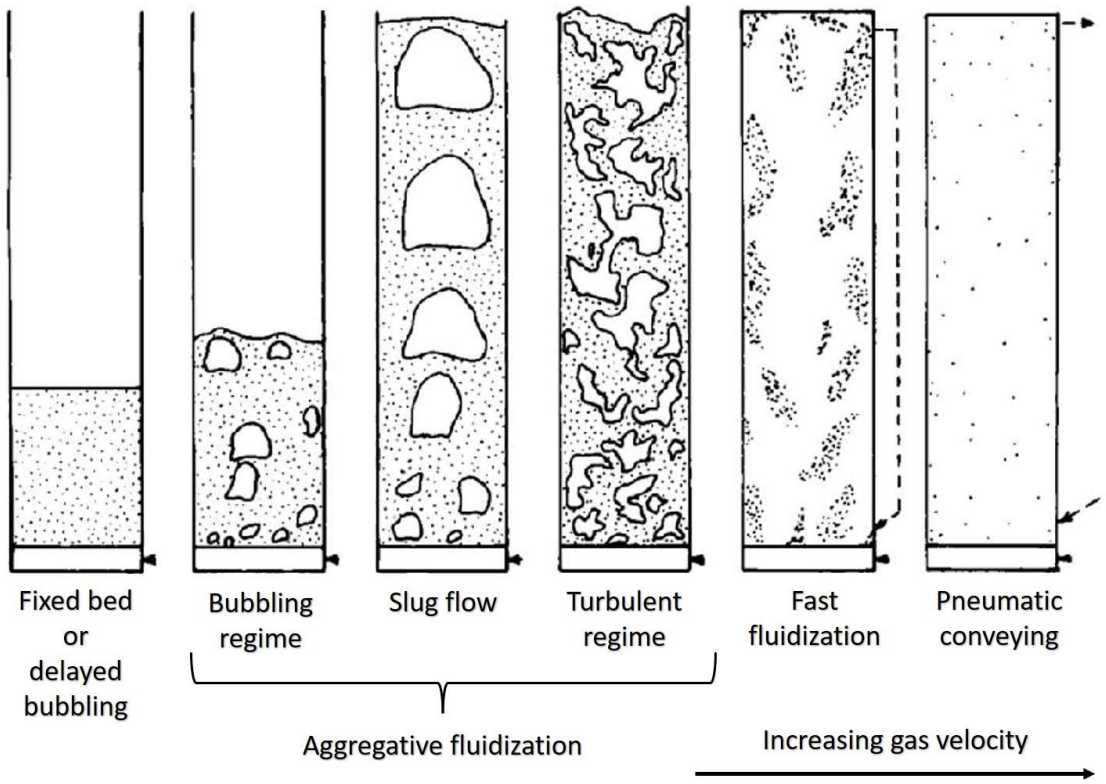

Figure 1.1 Schematic representation showing appearance of flow regimes relevant to gas-solid fluidization[37].

As a type of reactor, the fluidized bed is widely used in industrial processes. Among the flow regimes as presented above, the bubbling regime is one of the most widely encountered in industrial practice and also in academic research. The bubbling fluidized bed is characterized by several features[38,39]: (1) The particles are in contact with the gas in a suspended state, in forms of the dense emulsion and dilute bubbles, and the gas-solid interface area is large; (2) It has better particle mixing and gas-solid contact, higher heat and mass transfer rate; (3) The particle flow behavior within the

bed resembles that of a fluid; (4) Changes in porosity within the gas-solid system can significantly impact the drag coefficient of particles. Additionally, this technology offers a wide range of operating densities, simple equipment structure, and low cost, making it an attractive choice for various industrial applications.

Due to global warming, climate change and the depletion of fossil resources, there is an increasing interest around sustainable, environmentally friendly and renewable resources. As one of the renewable resources, the biomass is advantageous due to its wide distribution and high storage, and is environmentally friendly[40-44]. The bubbling fluidized bed has gradually demonstrated its advantages in the gasification and combustion of biomass[45,46], and combustion of waste[47-49], and has obtained a broad range of applications. Radmanesh et al.[45] developed a model of biological gasification in a bubble fluidized bed, with consideration of the pyrolysis and various heterogeneous and homogeneous reaction kinetics and hydrodynamics. Kong et al.[50] analyzed the particle behaviour of biomass gasification, and discussed the contribution of different heat transfer models in a bubble fluidized bed. Tokmurzin et al.[51] used simulation to study the gasification process of solid waste, explored the gasification mechanism of solid recovered fuel at the macroscale and studied the effect of the change in feed location. The bubble fluidized bed has also been widely used in processes of chemical, metallurgy, food, medicine, petrochemical, and agriculture industries. However, in

realistic industrial processes, most of the particles are nonspherical. Therefore, it is necessary to study the dynamic characteristics of gas-solid two-phase flow in bubbling fluidized beds with nonspherical particles, which can be expected to provide theoretical basis for the optimal design and operation of gas-solid bubbling fluidized beds in industries.

1.3 Description of nonspherical particles

The most basic characteristics of granular matter are geometric characteristics, including particle size, shape, etc. The geometric characteristics of particles can be described by the external dimensions of particles. Nonspherical particles can be divided into regular (cylindrical, cubic, ellipsoidal; see Figure 1.2) and irregular (non-symmetric rough surfaces) shaped particles, and artificially defined parameters such as the equivalent diameter and particle shape factor are required to describe their size and external shape.

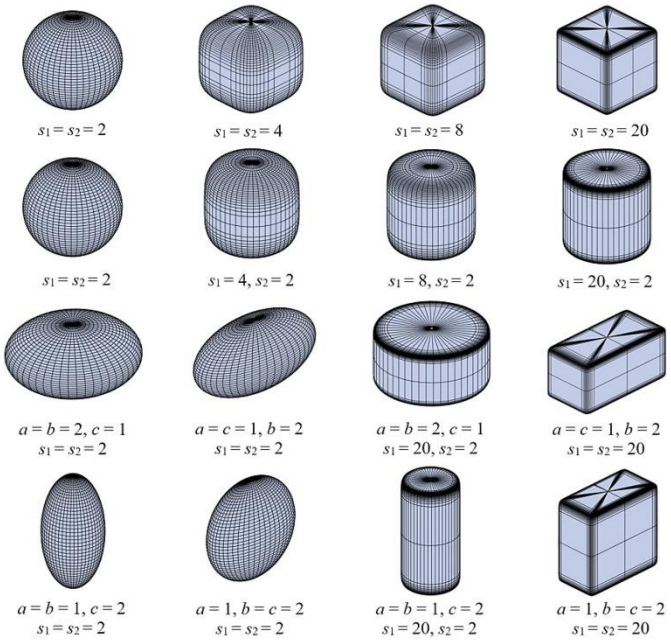

Figure 1.2 Different particle shapes[52].

1.3.1 Equivalent diameter

The equivalent diameter of particles is normally determined based on the following three definitions:

(1) Volume equivalent diameter d_v

$$V = \frac{1}{6}\pi {d_v}^3 \tag{1.1}$$

$$d_v = (\frac{6V}{\pi})^{\frac{1}{3}} \tag{1.2}$$

where V is the particle volume.

(2) Surface area equivalent diameter d_s

$$S_p = \pi {d_s}^2 \tag{1.3}$$

$$d_s = (\frac{S_p}{\pi})^{\frac{1}{2}} \tag{1.4}$$

where S_p is the surface area of the particle.

(3) Specific surface area equivalent diameter d_{sv}

$$\frac{S_p}{V} = \frac{\pi {d_{sv}}^2}{\frac{1}{6}\pi {d_{sv}}^3} \tag{1.5}$$

$$d_{sv} = \frac{6V}{S_p} \tag{1.6}$$

There is a certain relationship between them. When a particle is spherical, the three equivalent diameters are equal. When a particle is nonspherical, there are:

$$d_s \geq d_v \geq d_{sv} \text{ and } d_{sv} = \frac{{d_v}^3}{{d_s}^2} \tag{1.7}$$

1.3.2 Particle shape factor

The shapes of nonspherical particles can be described by the particle shape factor, as follows:

(1) Particle sphericity $\emptyset$[53-56]

Sphericity refers to the extent to which their shape approximates that of a sphere. It is a dimensionless parameter defined as the ratio of the surface area S_v of a sphere equal to the volume of the particle under investigation to the surface area S_p of the particle under investigation:

$$\emptyset = \frac{S_v}{S_p} = \frac{d_{sv}}{d_v}\left(\frac{d_v}{d_s}\right)^2 \tag{1.8}$$

(2) Aspect Ratio χ[57-59]

Aspect ratio is defined as the ratio of its length (l_p) to width (d_p):

$$\chi = \frac{l_p}{d_p} \tag{1.9}$$

In addition, there are other definitions of particle shape factor such as the zingg factor[60], corey shape factor[61,62].

1.4 Research progress of nonspherical particles

There are mainly two methods in the study of dense gas-solid two-phase flow: numerical simulation and experiment. One of the most direct methods to research the fluidization characteristics of gas-solid two-phase flow is through experimental methods. Many experimental techniques, such as magnetic particle tracking(MPT)[25,63,64], positron emission particle tracking(PEPT)[65-67], radioactive particle tracking(RPT)[68-70], particle tracking velocimetry(PTV)[24,71,72] and particle image velocity (PIV)[73-75] have been used to research dense gas-solid two-phase flow systems. With the help of various instruments, the fluidization information within the bed can be easily and intuitively obtained by the experimental method (see Table 1.1).

Table 1.1 Reference of experiments of nonspherical particles.

Author	Particle shape	Measurement method	Aspect ratio	Research content
Chen[76]	Cylindrical	XPTV	1.56; 5.33	Particles orientation distribution
Mema[25]	Spherocylindrical	MPT	4	Fluidization of spherical versus elongated particles
Mema[77]	Cylindrical	X-ray tomography	4; 6	Fluidization of spherical versus elongated particles
Cai[78]	Cylindrical	PTV	6; 8; 10, 12; 14	Orientation of cylindrical particles
Boer[79]	Cylindrical	PTV	10	Orientation and de-mixing phenomena of elongated particles
Vinay[24]	Spherocylindrical	PTV	4	The effect of particle shape on fluidization behavior

As computer technology advances rapidly, numerical simulation has also become a crucial approach for investigating gas-solid two-phase flows.In particular, the combination of computational fluid dynamics (CFD) and the discrete element method (DEM) is a useful tool for describing the fluidization of particles[27-29,80-84] . In recent years, different approaches to modelling nonspherical particles have also been employed to research the fluidization behavior of nonspherical particles, such as the multi-sphere model[85-87], the real geometry model[88,89], polygons/polyhedrons[80,90-92] and super-quadrics[2,93,94].

1.4.1 Macro-scale flow description

Researchers revealed experimentally and numerically the significant impact of

particle shape on the macro-scale flow description [24,95], including the fluidization regime transitions, pressure drop, the minimum fluidization/bubbling velocity[23,60,96-98], particle circulation patterns[99], bed expansion, etc. These characteristics are the key and directly related to the structure and operating parameters of key equipment such as fluidized beds in industrial applications. Most of the research on nonspherical particles is focused on this part. Particle shape significantly impacts the packing properties, fluidization behavior can be observed with varying particle shapes[60,96,100-102].

The impact of shape on the minimum fluidization velocity is significant. The minimum fluidization velocity of nonspherical particles[60,96,97] decreases at first, approaching a minimum, then increases inversely as the aspect ratio (i.e., the ratio of axial length to diameter) increases from unity (corresponding to a sphere) to higher values. Liu et al.[60] examined the impact of particle shape on pressure drop and minimum fluidization velocity by distinct particle shapes: circular plate-like, cylinder, and square cylinder. They found that the fluidization velocity of nonspherical particles was lower compared to spheres of the same equivalent diameter. Gan et al.[98] investigated the effect of shape on pressure drop, minimum fluidization velocity, and bubbling velocity by CFD-DEM. The findings indicate that as the aspect ratio increases, the minimum fluidization velocity initially decreases and subsequently increases. The impact of particle shape on the minimum fluidization velocity are investigated by

ellipsoidal particles [103,104]. Ma et al.[105] demonstrated the connection between pressure drop and gas velocity using rod-like particles by CFD-DEM. The study results indicate that both the drag force and the interlocking between rod-like particles have a notable impact on the minimum fluidization velocity.

The fluidized bed tends to form channels rather than undergos smooth fluidization when the particle shape deviates more from being spherical[24,95,102,106,107] (see Figure 1.3 and Figure 1.4). Two types of channeling can be further distinguished as the passive and the active[24,95]. Once a passive channeling is formed, the neighbouring particles will reach a stable state, and no further movement can be observed. However, many particles are sucked into the channel for an active channeling, forming a fountain[24,95]. Vollmari et al.[95,102,107] investigated the imapct of particle shape on the pressure drop and flow regime transitions by experiments and simulations using various regularly shaped particles. Hilton et al.[100] examined the imapct of particle shape on pneumatic conveying through CFD-DEM, and discovered that particle shape had a substantial influence on flow under identical conditions. Spherical or near-spherical particles transit to slug flow at high gas flow rates, while nonspherical particles transit to dilute flow.

Mema et al.[25] also analyzed the impact of particle shape on the particle circulation mode. For spherical particles, the particles tend to rise in the center of bed and fall on

the side wall. At low gas velocity, there are two counter-rotating vortices, but as the gas velocity increases, the counter-rotating vortices disappear. However, for elongated particles, there are different circulation modes, and there is always a circulation mode of rising particle boundary and falling in the middle. With an increase in gas velocity, the spherical cylindrical particles show a more obvious double circulation mode, and the vortex is much larger than in the case of spherical particles.

A higher bed expansion rate indicates a more favorable gas-solid contact mode, and is significantly influenced by particle shape. For a spouted bed, Liu et al.[108] used thirteen types of particles to study the imapct of particle shape on fountain height of nonspherical particles. Ignoring the impact of particle shape, they discovered that the predicted fountain height was significantly lower than the experimental data. Liu et al.[88] used a real geometric model to study the effect of shape on the spouted bed. They found that the stability of the fountain decreases as the particle shape gradually deviates from a sphere, as does its height. Zhong et al.[101] further studies cylindrical particles flow by using the multi-sphere model. The results showed that the porosity of nonspherical particles is larger than that of spherical particles, resulting in a larger bed expansion rate. Emden et al.[95] also found a similar phenomenon by experiments.

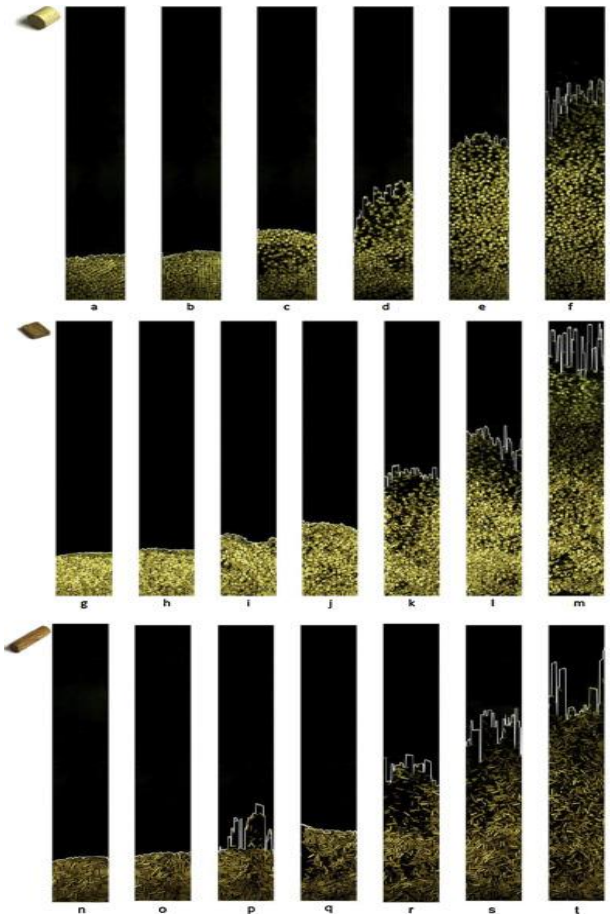

Figure 1.3 Flow regimes and the computed bed expansion (white line) of particles for different shapes[95].

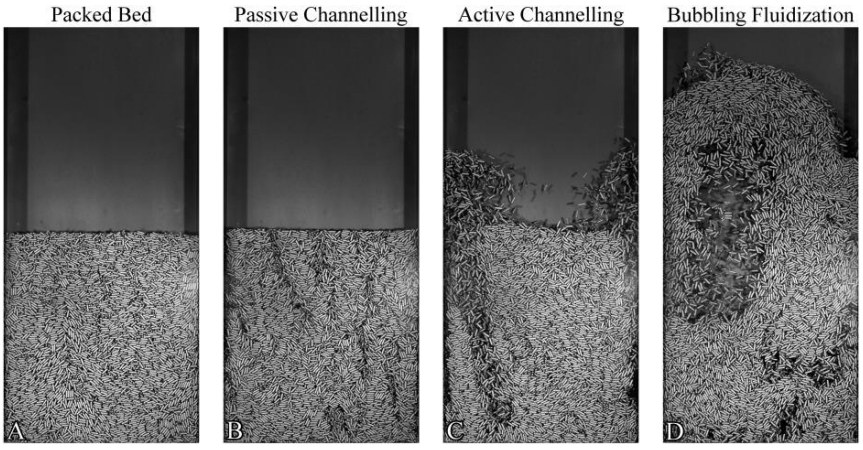

Figure 1.4 Examples of the different fluidization regimes observed in the bed with increasing gas velocity.

Additionally, some scholars have studied the macro-scale characteristics of multi-

component system, consisting of nonspherical particles and fluidized media[92,109-116], as shown in Figure 1.5. Fluidized media typically consist of inert materials such as silica sand, alumina, or calcite. Researchers have primarily focused on studying the onset of minimal fluidization of multi-component particle systems.

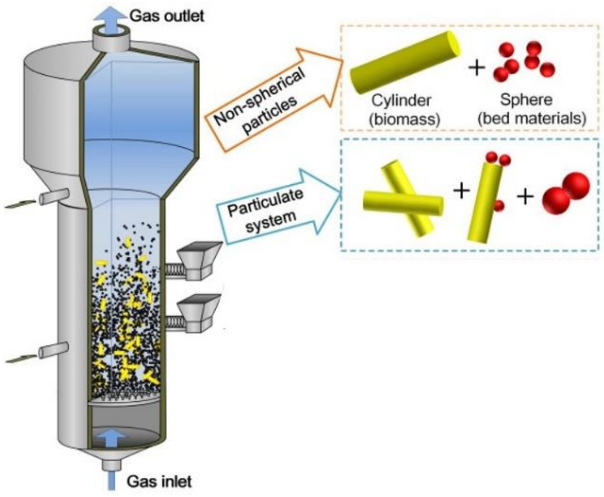

Figure 1.5 A typical dense and multi-shape particle-fluid systems[2].

Abdullah et al.[109] investigated the fluidization behavior of various types of biomass, including the palm fibe, sawdust, peanut shell, coconut shell, and rice husk. For each particle type, they measured the pressure drop and compared the minimum fluidization velocity with several empirical correlations. They found that the fluidization of both Geldart-D (rich husk) and Geldart-A (palm fiber) particles is poor. The minimum fluidization velocity obtained from the experiment did not align with the predicted value, except for the rice husk. Zhong et al.[92] employed an experimental approach to study fluidization of biomass particles such as cotton stalk, millet, mung

beans, and wood chips. The results showed that the minimum fluidization velocity of long thin biomass types such as corn stalk was proportional to transection diameters and aspect ratio of the particles.

1.4.2 Micro-scale flow description

The research on nonspherical particles mainly focuses on the macroscopic scale. However, the mirco-scale laws which have been extensively researched in the fluidization of spherical particles[117,118], are much less known about nonspherical particle fluidization. The micro-scale characteristics of nonspherical particles mainly involves issues with velocity, orientation, contact forms between particles, and so on. Due to the anisotropy of rod-like particles in the flow field, their orientation and rotation must be considered and the contact between particles is more complex and diverse (see Figure 1.6), which makes their hydrodynamic characteristics more complicated.

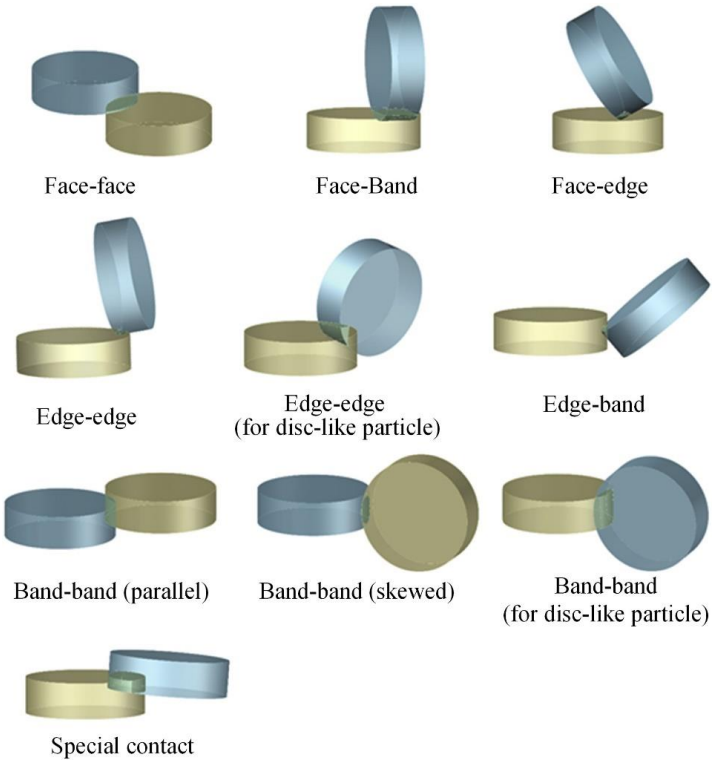

Figure 1.6 Contact scenario between cylindroid particles used in the literature[89,119,120].

The drag force model is regarded as the coupling term between the gas phase and the solid phase, which is the basis for describing the flow behavior of particles. For nonspherical particles, the drag coefficient is not constant and can vary depending on the orientation of the particle with respect to the flow direction. This makes the problem of predicting the behavior of fluidized beds with nonspherical particles more complicated. Hilton et al.[96] reported that particle shape affects the drag. Two main categories exist in the study of drag force on nonspherical particles [2]: the first category involves developing specific drag force models based on fixed shapes and orientation, such as polyhedron[121,122], cylinder[123-131], disk[132-136], cube[137-140] and other shapes[141-

143]. The other is a drag model that covers as many shapes and orientations as possible[21,144-152] (see Table 1.2). For example, Hölzer et al.[21] proposed the standard drag coefficient of any shape based on a comprehensive analysis of literature data. The formula takes into account the Reynolds number, particle shape, and orientation. It is verified that the drag model can well predict the fluidization behavior of various nonspherical particles.

Table 1.2 General expressions of C_D for nonspherical particles[2].

Authors	Equations	Conditions
Chien[145]	$C_D = \left(\frac{30}{Re}\right) + 67.289, \exp(-5.03\emptyset)$	$0.2 \le \emptyset \le 1$ $Re < \sim 5000$
Leith[149]	$C_D = \frac{8}{Re}\frac{1}{\sqrt{\emptyset_{\parallel}}} + \frac{16}{Re}\frac{1}{\sqrt{\emptyset_{\perp}}}$	Stokes region
Ganser[146]	$C_D = 0.42 \cdot 10^{1.8148}(-\log\emptyset)^{0.5743}$	Stokes region
Swamee[150]	$C_D = [\frac{48.5}{\left(1 + 4.5{C_0}^{0.35}\right)^{0.8} Re^{0.64}} + \{(\frac{Re}{Re + 100 + 100C_0})^{0.32} \frac{1}{{C_0}^{18} + 1.05{C_0}^{0.8}}\}c]$ $C_0 = c/(ab)^{1/2}$	$0.3 < C_0 < 1$ $1 < Re < 10^4$
Tran-Cong[151]	$C_D = \frac{24}{Re}\frac{d_n}{d_A}\left[1 + \frac{0.15}{\sqrt{C_{ir}}}\left(\frac{d_A}{d_n}Re\right)^{0.687}\right] + \frac{0.42(\frac{d_A}{d_n})^2}{\sqrt{C_{ir}}[1 + 4.25 \times 10^4(\frac{d_A}{d_n}Re)^{-1.16}]}$	Cubes, cylinders and so on. $0.1 < Re < 1500$
Hölzer [21]	$C_d = \frac{8}{Re}\frac{1}{\sqrt{\emptyset_{\parallel}}} + \frac{16}{Re}\frac{1}{\sqrt{\emptyset}} + \frac{3}{\sqrt{Re}}\frac{1}{\emptyset^{\frac{3}{4}}} + 0.42 \times 10^{0.4(-\log\emptyset)^{0.2}}\frac{1}{\emptyset_{\perp}}$	

In addition to the drag, nonspherical particles also experience the lift force, pitching torque, and rotational torque[22,153-159]. Compared with spherical particles, the lift can change significantly the particle orientation and further affect the trajectories of nonspherical particles. Therefore, the lift of nonspherical particles cannot be ignored[106,153-155]. Mema et al.[155] employed CFD-DEM approach to study the impact of the lift force and hydrodynamic torque on nonspherical particles. The findings indicate that the velocity of particles parallel to the gravity direction is significantly affected by lift, and the hydrodynamic torque determines particle orientation.

In addition to the above, a big difference between nonspherical particles and spherical particles is that nonspherical particles are directional[76,78,160-178] and have preferred orientation order and flow alignment[24,97,105,179]. Hidalgo et al.[180] observed that particle shape has an impact on particle packing performance, with elongated particles showing a tendency to align perpendicular to gravity. Ma et al.[26,105,181] used the super-ellipsoid model to research the fluidization characteristics of disc-like particles and rod-like particles. The preferred orientation of particles differs between fixed beds and fluidized states. In fluidized states, particles tend to align their long axis parallel to the gas flow direction, while in fixed beds, the preferred orientation is perpendicular to the gas flow direction. In addition, they found that particle orientation

was affected by the aspect ratio. With an increase in gas velocity, the tendency of the long axis of the particle to be parallel to the gas flow direction is higher, but the aspect ratio has no obvious effect on the particle orientation at very high gas velocities. And near the boundary, the long axis of particles tends to align with the vertical direction, with larger aspect ratio particles exhibiting more pronounced wall effects. Oschmann et al.[172] also found, through numerical investigations of nonspherical particles, that cylindrical particles in the near-wall region tend to orient themselves parallel to the wall.

In addition to studying the distribution of particle orientation in multicomponent systems. Ma et al.[182] used the super-ellipsoid model to account for particle shape in their investigation of fluidization in a binary mixture of rod-like and spherical particles. Compared to a monodisperse particle system, the orientation distribution of particles in a binary particle system is distinct. It is noteworthy that there is always an apparent wall effect on the particle orientation, regardless of whether it is a monodisperse particle system or a binary particle system.

At the same time, the particle velocity distribution is also different. Particle velocity is a critical parameter that directly affects the solids mixing, heat and mass transfer, and particle wear in a fluidized bed. Additionally, the study of particle velocity is essential to understand the fundamental laws of gas-solid two-phase flow. A study by Yan et al.[183] employed an artificial neural network-based drag coefficient correlation

to investigate the hydrodynamic behavior of particles.The study found that the particle shape has a negligible effect on the horizontal velocity, but it has a significant impact on the vertical velocity. However, this effect is not a monotonic function. Wang et al.[184] found that ellipsoidal particles with higher sphericity have larger vertical velocity than ellipsoidal particles with lower sphericity. The lower sphericity of ellipsoidal particles results in the formation of more bridges, hindering bed permeability and particle motions. Therefore, for ellipsoidal particles with low sphericity, higher superficial gas velocity is needed to make the particles fluidize well. This phenomenon was also found in the fluidization process of nonspherical particles in spouted bed[185].

For binary particle system, Fotovat et al.[186,187] analyzed the velocity distribution characteristics and particle circulation patterns in the co-fluidization process of cylindrical particles and bed material particles by experiments and simulations. At the same gas velocity, the rising velocity of spherical particles is greater compared to that of cylindrical particles. At low gas velocity, cylindrical particles cannot form a complete circulation mode in the bed and are concentrated in the upper part. Chen et al.[188] analyzed the distribution and velocity of cylindrical particles though stereo XPTV technology. Cylindrical particles tend to aggregate on the side wall. With an increase in gas velocity, the distribution of cylindrical particles becomes more uniform. Moreover, the particle velocity increases with increasing gas velocity. Ren et al.[189,190] employed

the CFD-DEM method to investigate the mixing behavior of particles. Their findings indicated that the average translation velocity of slender particles and spherical particles are similar when fully mixed, but the average rotation velocity of spherical particles is higher.

1.4.3 Meso-scale characteristics: particle configuration and bubbles

1.4.3.1 Particle configuration

In a qualitative sense, the interlocking in granular materials can be described as the state in which particles or grains lock into each other and provide additional resistance to deformation. The interlocking is purely a geometric feature of any particle assembly[191]. The interlocking between nonspherical particles will hinder the movement of particles, making the fluidity of nonspherical particles worse than that of spherical particles, and the mutual support between particles becomes stronger, which leads to the higher bed height of nonspherical particles. At the same time, the interlocking phenomenon between particles is generally more obvious with the increase of particle aspect ratio.[26,97,98,105]. A localized structure is formed inside the bed as a result of particles interlocking. The particle configuration can strongly affect the fluidization behavior of particles. Analyzing these particle structures can significantly enhance our understanding of the mechanisms underlying the fluidization behavior of

nonspherical particles.

The imapct of particle shape on particle configuration was further analyzed from the structural parameters such as coordination number[24,88,96,97,104,192-198], radial distribution function[104,180,194,198-205] and nematic correlation function[161,200,206-215].

Particle shape has an a significant impact on the packing structure of particles, which in turn affects the transport properties of the bed. For example, elongated particles tend to form ordered structures compared to spherical particles[104,180,198,200,201,204]. Zhou et al.[104] studied the packing characteristics of ellipsoid particles by employing coordination number and radial distribution function analysis. The results show that ellipsoids tend to form locally ordered structures (see Figure 1.7). Zhao et al.[198] studied the random packing of elongated particles and observed that with an increase in aspect ratio, the contact between spheres decreases, and the contact between cylinders increases. There are three different local ordered structures in the bed: the shortest contact between the centroids of the two spherocylinders, the vertical contact between the two spherocylinders, and an additional particle between a pair of spherocylinders.

Nonspherical particles in fluidized beds tend to form locally ordered structures and clusters, which move as a large lump and exhibit hydrodynamic interactions. The coordination number increases as the aspect ratio deviates from a sphere, and ellipsoidal

particles tend to form aggregates. Hamid et al.[216] observed that at a lower volume fraction, the inhomogeneity in the microstructure of particles also leads to the formation of clusters, and rods have a larger settling velocity than isolated particles. In addition, due to the formation of clusters, the velocity fluctuation is greater than that of spherical particles. These clusters move as a large lump, causing obvious hydrodynamic interactions. In further research on fluidized particles, Gan et al.[197] found that as the aspect ratio deviates from that of the sphere, the average coordination number increases. In a fluidized bed, ellipsoidal particles tend to form clusters or aggregates. Mahajan et al.[24] found that rod-like particles tend to be coaligned within a distance of approximately one particle length(see Figure 1.8), and even at the highest flow rate, particles exhibit interlocking behavior and move in a large lump. However, the local structure of particles is also susceptible to fragmentation, resulting in a decrease in the coordination number. Boer et al.[79] studied the de-mixing phenomenon of rod-like particles. The result showed the shape-driven separation between particles occurs by studying the de-mixing phenomena of rod-like particles. This dominance is assured by the fact that alignment and aggregation of rod-like particles reduce the drag force per unit mass compared to spherical particles, allowing rod-like particles to sink to the bottom of the bed.

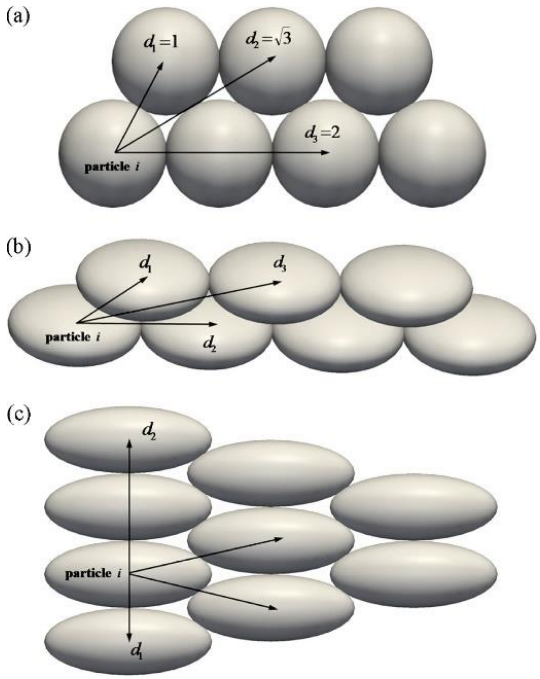

Figure 1.7 Ordered packing structures for (a)spheres; (b)oblate spheroids; (c)prolate spheroids[104].

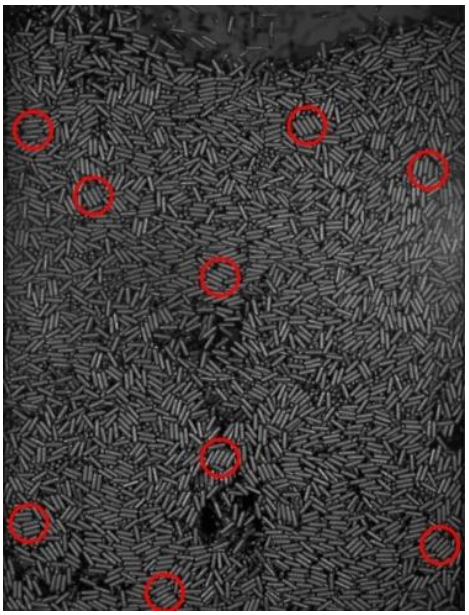

Figure 1.8 An example of particle coalignment[24].

1.4.3.2 Bubble

The formation and dynamics[30,217-219] of bubbles in a fluidized bed are important in understanding the behavior of particles in the bed. Bubbles are formed near the distributor and interact with each other during their rise, causing coalescence and fragmentation. The shape, size, and rising velocity of bubbles[220-223] affect the fluidization quality of particles. However, most studies on bubble dynamics have focused on spherical particles[75,224-226], and the impact of particle shape on bubble dynamics needs further investigation to improve the design and operation of fluidized beds.

The number of studies investigating the impact of particle shape on bubble dynamics, whether experimental or numerical, is not as high as anticipated. Shrestha et al.[227] investigated the impact of particle shape on bubble dynamics in fluidized bed using a continuous central jet. The results showed that the particle shape affects the mechanism of bubble fragmentation and coalescence. The equivalent diameter distribution of bubbles for the ellipsoid is wider compared to that of the sphere. At any position of the bed, spheres have more circular bubbles than ellipsoids. Esgandari et al.[228] also found that elongated sphero-cylindrical particles have a lower leakage fraction compared to spherical particles. The bubble shape of spherical cylindrical particles is slender, while for spherical particles, it is more rounded.

The bubble dynamics[226] of ellipsoidal particles were studied and compared to spherical particles. There was a significant difference in the average value of the corresponding bubble diameter between the two particle morphologies. Ellipsoidal particles have an asymmetrical particle flow pattern due to non-uniform bubble flow, resulting in a decrease in the velocity of bubbles. Furthermore, it has been observed that ellipsoid particles exhibit lower bubble velocities than spherical particles. This can be attributed to the fact that bubbles need to overcome the particle interlocking. The influence of particle aspect ratio[229] on bubble dynamics was also discussed, showing that the equivalent diameter of the bubbles gradually increases as the aspect ratio of particles increases when the bed height is low.

1.4.4 Summary

Numerous domestic and foreign scholars have conducted extensive numerical simulations and experimental studies on gas-solid two-phase flows in bubbling fluidized beds, predicting flow characteristics and motion laws of gas-solid two-phase flow. This provides a theoretical reference for the design, optimization, and operation of fluidized bed reactors. Many factors can affect fluidization characteristics, including the particle size and shape. However, most studies were carried out using near-spherical particles due to their geometric simplicity. In industrial processes, however, most

particles are nonspherical (say, spheroids, rods, and polygons). The particle shape, being one of the most important properties of particles, significantly impacts fluidization behavior, including flow, permeability, chemical reactions, and segregation. The assumption of spherical particles cannot truly reflect the flow behavior of particles in fluidized systems. Therefore, it is of great significance to study the gas-solid two-phase flow characteristics of nonspherical particles in a bubbling fluidized bed.

At the meso-scale and micro-scale, the existing research on fluid dynamics of nonspherical particles is insufficient, despite numerous studies on spherical particles. Furthermore, there is still a lack of experimental research on the fluidization behavior of nonspherical particles. At the macro-scale, the research has focused on particles with clear shapes, and the impact of aspect ratio on macro-scale law remains incomplete. At the micro-scale, the research on the micro-scale characteristics of rod-like particles is still incomplete. Questions exist at such as how the velocity of the particles (translational velocity and rotational velocity), and the orientation of the particles change with the particle properties and operating parameters? At the meso-scale, the research on the motion mechanism of bubble and particle configurations is still incomplete. For example, how do operating parameters and particle properties affect the shape and motion of bubble and particle configurations? The relationship between bubble dynamics and nonspherical particle orientation is still unclear, and how does the

particle configuration affect the particle dynamics of nonspherical particles? Further research and exploration are needed on these aspects.

1.5 Outline of thesis

The current numerical simulation and experimental research mainly focus on the gas-solid two-phase flow of spherical particles, and there are few studies on the gas-solid two-phase system of nonspherical particles. Therefore, this study focuses on the gas-solid two-phase flow of nonspherical particles, and uses the particle tracking velocimetry (PTV) method to comprehensively study the fluidization behavior and meso-scale structure of a fluidized bed with nonspherical particles, as well as the underlying mechanism. PTV is a non-invasive, transient, full-field velocity measurement technique that tracks the movement of all particles in the flow field. This method is highly accurate and provides visual intuitiveness, making it particularly useful for studying complex and dynamic flows. It has been applied in various fields such as turbulent flows, multiphase flows, and biological flows. In order to better understand and master the flow mechanism of rod-like particles, and, especially in light of the importance of particle configuration in determining nonspherical fluidization behavior above, it is necessary to explore the dependence of the particle configuration on the particle shape and two-phase flow conditions.

Therefore, this thesis carries out the research on the flow characteristics of rod-like particles in a bubbling fluidized bed. The effects of particle properties and operating parameters on the fluidization behavior and mesoscale structure of nonspherical particles are investigated experimentally. As shown in Fig. 1.9, the thesis is structured as follows: (1) The research on the fluidization behavior of rod-like particles was first carried out, focusing on the macro-scale laws such as the pressure drop, minimum fluidization velocity, and bed height, as well as the micro-scale motion laws such as particle orientation, particle velocity, and particle kinetic energy. (2) Particle configuration dynamics of rod-like particles was qualitatively analyzed by using the coordination number, radial distribution function, and nematic equivalence structure parameters, and the flow properties of super-particles were studied. (3) Exploration of bubble dynamics of nonspherical particles, including meso-scale laws such as volume, shape, and velocity of bubbles.

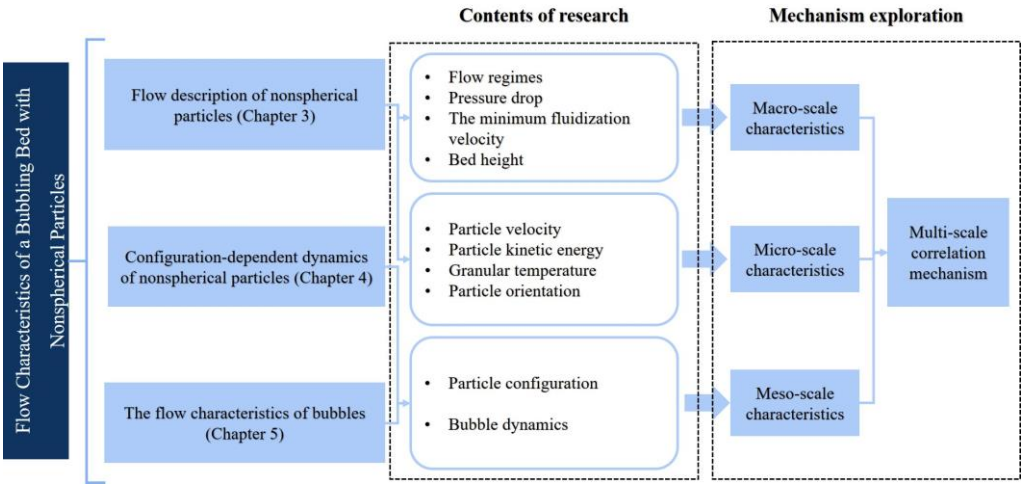

Figure 1.9 The structure of the thesis.

2 Experimental Setup & Technical Approach

2.1 Introduction

Experimental measurement is one of the important research methods in the study of dense gas-solid two-phase flow. PTV technology finds extensive applications in the field of fluidization as an optical measurement technology. PTV mainly utilizes a camera to capture the movement of particles. This technology can obtain dynamic information such as the position, velocity, and orientation of a single particle without interfering with the flow field.

In this chapter, a fluidized bed experimental measurement platform is established based on PTV measurement technology to conduct experimental research on the fluidization behavior of nonspherical particles. The experimental system is introduced, including the fluidized bed equipment, image processing, experimental data collection and processing methods, and the definition of each variable.

2.2 Experiments

Since the PTV measurement technology is easily blocked by dense solid particles, and cannot penetrate the bed, it is generally only suitable for measuring two-dimensional fluidized beds. In this experiment, a pseudo-2D fluidized bed was selected

for experimental research. Figure 2.1. shows that the experimental device is primarily constructed of transparent polymethyl methacrylate, 150 mm×25 mm×1500 mm (width × thickness × height). The experimental device includes four parts: inlet section, gas chamber, fluidized bed body and an outlet section. The ambient air, measured by a digital mass flow controller, enters the bed through the distributor made of a sintered plate and exits through the air outlet. The sintered plate is made of stainless steel with a thickness of 3 mm. Three types of alumina particles with equivalent volume but different aspect ratios χ, are selected. One of those are spherical particles(χ=1, marked as AR-1)), and the other two with χ=2 (AR-2) and 4 (AR-4) are cylindrical. It is worth noting that in our study, the smallest ratio of the bed thickness to the length of particles is 3, corresponding to the case where the aspect ratio increases to 4. According to the results of Mahajan et al.[24], such a ratio is sufficient to ensure that the particle behavior is shape induced. In our study, particles are packed with an initial height of 150mm. The superficial gas velocities of the observed cases are set to be 1.0, 1.4, 1.8 and 2.2 times the minimum fluidization velocity, U_{mf}, respectively. The parameters of experimental setup are listed in Table 2.1.

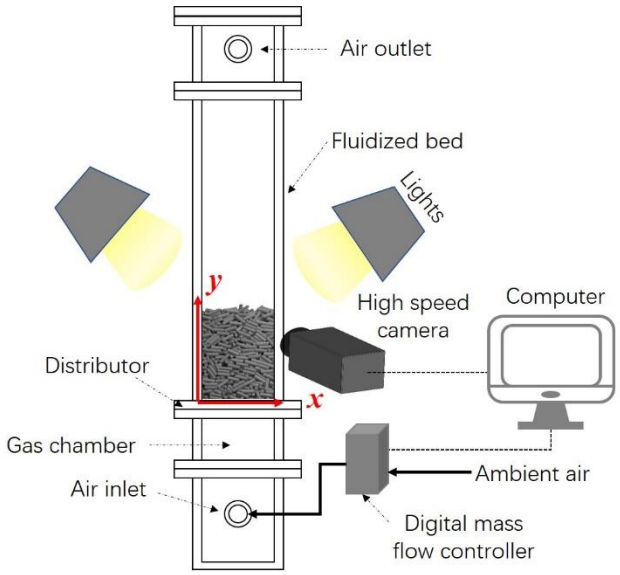

Figure 2.1 Experimental setup of the pseudo-2D fluidized bed.

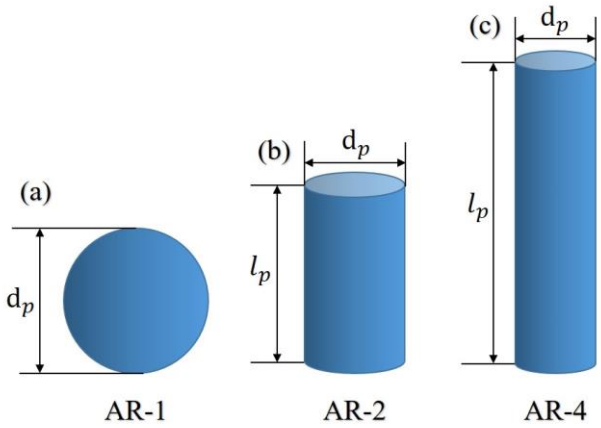

Figure 2.2 Illustrations of particles with different aspect ratios (χ): (a) χ = 1; (b) χ = 2; (c) χ = 4.

Table 2.1 Experimental settings.

Parameters	Value
Fluidized bed settings	
Width×height×thickness (mm×mm×mm)	150×1500×25
Alumina particle (kg/m^3)	3340~3567
Particle diameter (d_p)×length (l_p) (mm×mm)	3.6; 2.5×5; 2×8
Aspect ratio (χ)	1; 2; 4

Equal volume equivalent diameter (d_v) (mm)	3.6
Particle sphericity (∅)	1; 0.8294; 0.72
Packed bed height (mm)	150
Superficial gas velocity scaled with U_{mf}	1.0, 1.4, 1.8, 2.2
The pore size of the sintered plate (μm)	50
The thickness of sintered plate (mm)	3
Camera settings	
Camera resolution(pixels)	1920×2560
Frame rate(fps)	1000
Shooting area (mm×mm)	150×200

The experimental measurement device consists of two main components: pressure drop measurement and visual measurement. The pressure drop measurement system is composed of a differential pressure transmitter (Beijing North River Instruments Co., Ltd., DP102MD) and a four-channel recorder (Beijing Sike Instruments Co., Ltd., NR2400) with a sampling frequency of 1 Hz. The pressure measurement point is located at the elevation of 35 mm, and it measures the pressure difference between this point and the external atmospheric pressure. The measurement result does not represent the pressure drop of the entire bed, but the pressure drop generated by the particles above the pressure measurement point. The effective pressure drop of the bed above the pressure measurement point is used as the normalized reference variable in the measurement.

$$\Delta P_0 = \varepsilon_{s0}\rho_s g h \tag{2.1}$$

where ε_{s0} is the particle concentration at the initial accumulation, ρ_s is the particle density, g is the gravity acceleration, h is the height from the bed surface.

The minimum fluidization velocity is determined by measuring the bed pressure drop at various gas velocities. During the preparation stage of the experiment, particles were poured into the bed according to the same filling procedure. The particles fell from a fixed height, filling into the bed to the surface. Afterwards the particles were allowed to rest for a period of 10-15 minutes to reduce the effect of electrostatic effects on the particles. The same static bed height was maintained in each experiment. Starting from the fixed bed conditions, the bed pressure drop of each gas velocity is determined, and the gas flow rate is increased from a fixed bed to full fluidization, then decreasing it back to the fixed bed state. The step-change of the gas flow rate is 25 L/min. The minimum fluidization velocity is defined by convention as the intersection of the fixed bed line with the full fluidization line during decreasing fluidization velocity. For each superficial gas velocity, the measurement time is 3 min, and then the average pressure drop at each superficial gas velocity is obtained.

The visualization system includes a high-speed camera (NAC, HX-5E) and a light source. To obtain clear images, A black background is attached to the back wall of the fluidized bed to improve the contrast in addition to using two LED lights to illuminate

the bed surface at a certain angle, reducing the reflection from the front wall. The motion of particles are recorded by using a high-speed camera with a frame rate of 1000 fps and a resolution of 2560 × 1920 pixels. The total image area is 150 mm × 200 mm, and its width is equal to the width of the bed, allowing for a simultaneous recording of details from the wall to the center. The origin point of the recording is set at the lower left corner of the bed, with the x-coordinate representing the horizontal position and the y-coordinate representing the vertical position, as shown in Figure 2.1.

The fluidization experiment is performed first to reach a steady state, then a recording of 6s is taken for statistical analysis. In addition, we have repeated the experiment and recorded the data for more than 10 seconds with a larger memory of 64G of another high-speed camera, and got similar results. As an evidence, Figure 2.3 and Figure 2.4 show the comparison of the velocity fields of these two experiments and mean velocity results, respectively, with different time intervals. We can see that the results are not sensitive to the variation of average span Δt larger than 4s. The videos of moving particles are converted into digital images, and after image processing and particle tracking, we obtain the particle positions and velocities.

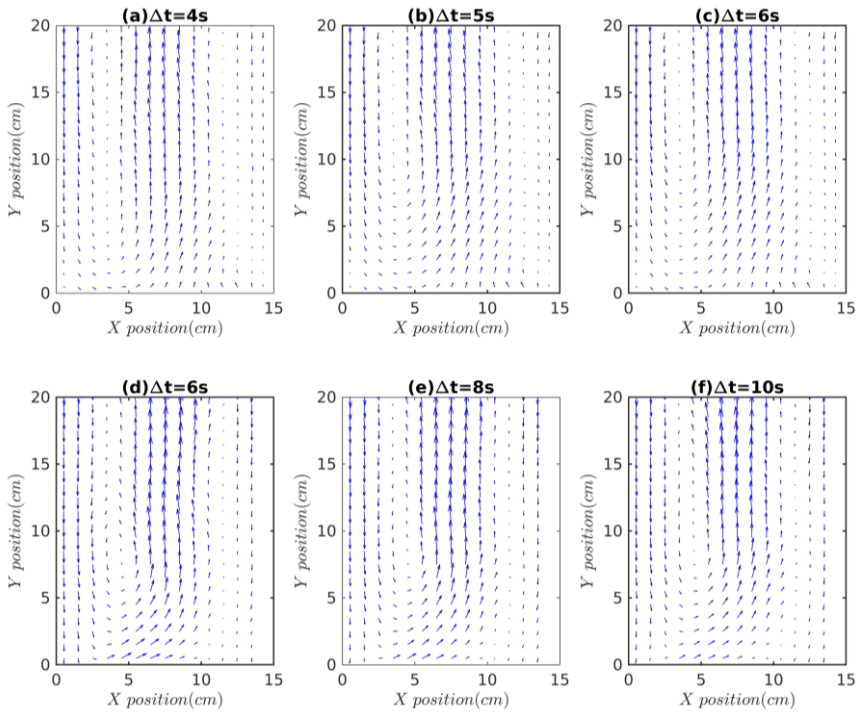

Figure 2.3 The velocity fields for AR-4 particles in the X-Y plane under different average spans (superficial gas velocity is $2.2U_{mf}$) ((a, b, c) are recorded with a memory of 32G; (d, e, f) are recorded with a memory of 64G.

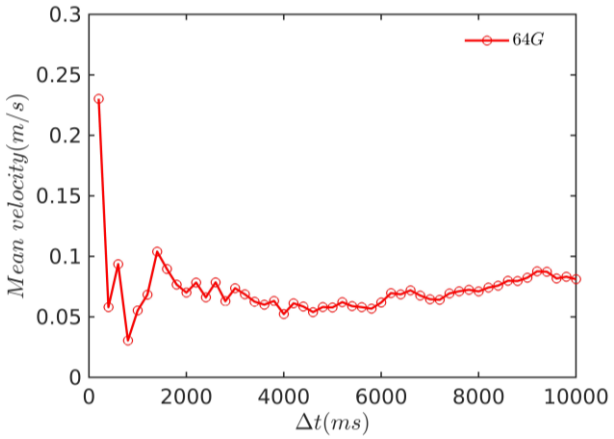

Figure 2.4 The variation of the mean velocity of AR-4 particles in the area between the heights of 50 mm and 100 mm (superficial gas velocity is $2.2U_{mf}$).

2.3 Image processing

After obtaining the original image, it is necessary to use image processing technology and particle tracking technology to obtain the position, orientation, and area of particles. This section will introduce the process of image processing in detail.

2.3.1 Particle identification

Particle identification refers to the process of obtaining parameters such as particle position, area, and orientation from an original image. In order to achieve this goal, a series of image processing techniques are needed. In this section, we take the image of a set of AR-4 particles as an example to introduce the detailed steps of the algorithm.

Figure 2.5 Example of digital image analysis (DIA) procedure: (a) the image is cropped and pretreated; (b) Binarized image; (c) Denoised image; (d) The center of mass of each particle is detected, and all parts too small (<600 $pixel^2$) or too large (>1200 $pixel^2$) are removed.

The image analysis in our study is based on MATLAB® and ImageJ®. Four typical step results of image processing are shown in Figure 2.5:

(a) the captured color picture is cropped, and preprocessed. It is necessary to remove all parts of the image that interfere with image identification, such as random

noise and the side and bottom of the container. Commonly used algorithms in ImageJ can be used to remove random noise. The boundary of the container needs to be cropped according to the geometric size of the container. At this stage, only the pixels belonging to each particle should be visible in the image;

(b) the automatic local threshold method is used to binarize the image; Binarization involves converting the original grayscale image into a black and white binary image, where the pixel grayscale belonging to the particle is set to 1, and the pixel grayscale belonging to the background is set to 0. To accomplish this, the automatic local threshold method is utilized. It is challenging to identify one or more suitable thresholds from an image in image processing. Generally, according to a certain empirical threshold, there is no obvious distinction between the original image and the binary image, and it is slightly corrected in the subsequent image processing;

(c) the denoising algorithm is employed to separate the particles. For complex images, the background and particles may not be completely distinguished by binarization, and some denoising algorithms are needed to optimize mathematical morphology.

(d) the particles are calculated and measured, and the particles too large (>1200 $pixel^2$) or too small (<600 $pixel^2$) are removed, then the position and orientation are obtained and marked. The second-order central moment is used to calculate the

orientation angle range within [0, 180). For our experimental system, the orientation angle is defined as the angle of the principal axis of the rod to the horizontal direction, i.e., 90° means the particle is vertical or streamwise, and 0° or 180° mean the particle is horizontal or spanwise, as shown in Figure 2.6.

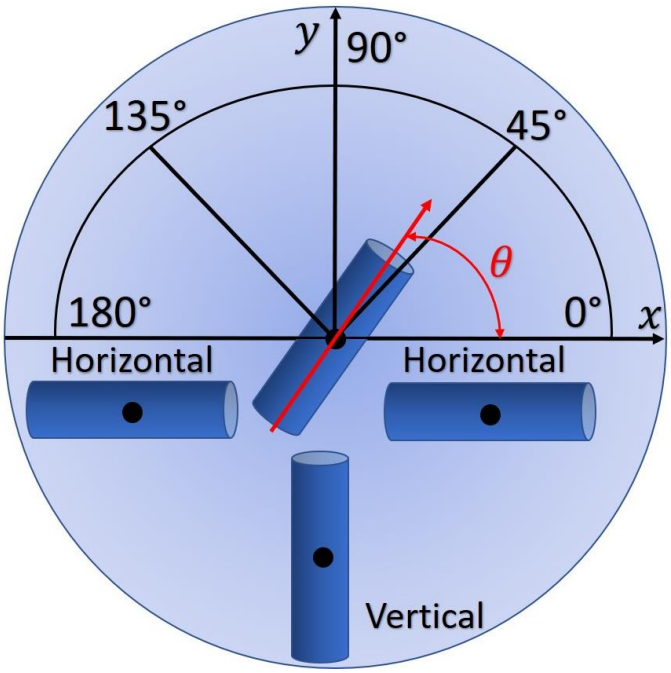

Figure 2.6 Definition of particle orientation angle.

2.3.2 Particle tracking

After obtaining the position information of particle within the shooting area, the particle tracking algorithm matches the corresponding particles on two successive images (see Figure 2.7). In detail, the target position in the previous frame is taken as the center, and then we search for the nearest neighbour in half of the particle width in

the new frame as the matching object of the target. Here, we show an example of particle trajectories obtained by the tracking algorithm (see Figure 2.8).

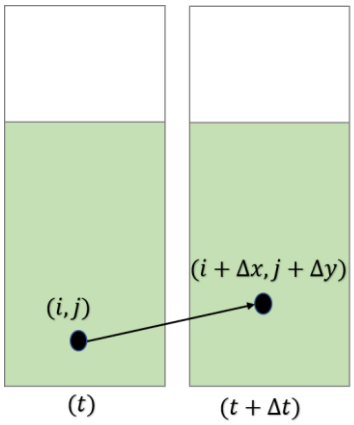

Figure 2.7 The schematic of the particle tracking algorithm.

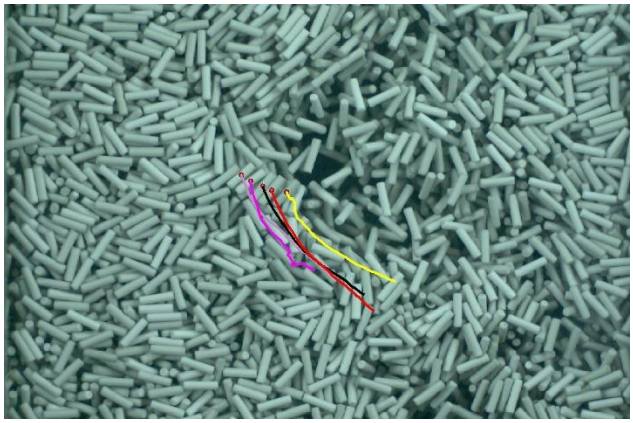

Figure 2.8 Example of particle trajectories within 105 ms.

2.4 Data processing

2.4.1 Particle velocity

After particle tracking, the displacement information of a single particle at adjacent

time can be obtained (see 2.3.2), then the velocity of a single particle can be calculated.

$$v = \frac{S_{i,t+\Delta t} - S_{i,t}}{\Delta t} \tag{2.2}$$

where i is the number of particles, t is time, Δt is the time interval between two frames. Here, v is a two-dimensional vector, representing only the horizontal and vertical directions, while disregarding motion in the thickness direction. An example is shown in Figure 2.9.

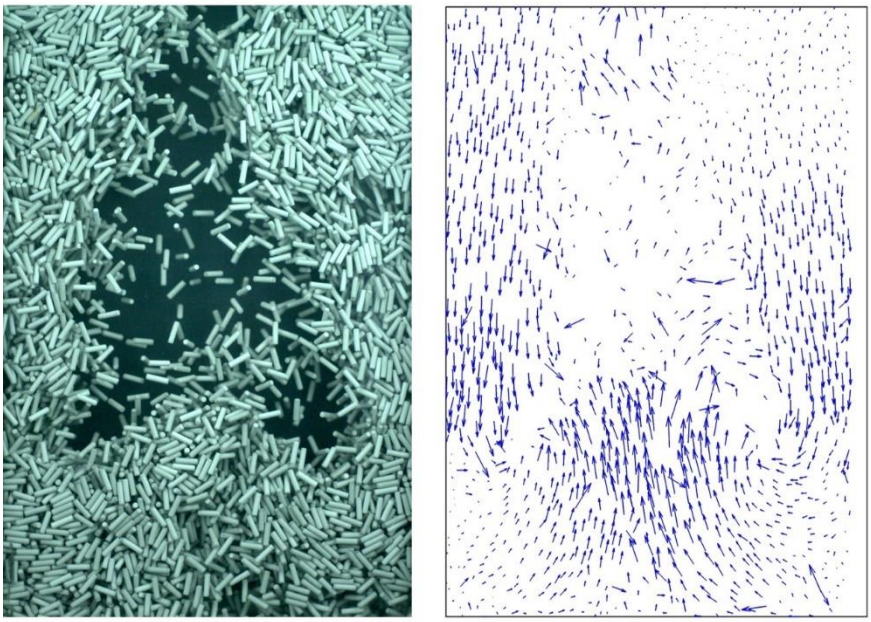

Figure 2.9 Example of particle velocity processing (a) the original image of AR-4 particles; (b) the vector field of particle velocity.

2.4.2 Order parameters

In the analysis of the local structure of rod-like particles, the difference between

nonspherical particles and spherical particles is that nonspherical particles have orientation. Consequently, when investigating the ordered structure of rod-like particles, we utilize the nematic-order correlation function and the tetratic-order correlation function to examine their orientation-based ordering[230-232]. Additionally, order parameters can be classified as global or local, depending on their definition. The local order parameter is more sensitive to local special structures and can be used to detect some particles with higher order in the whole system. In contrast, global order parameters are utilized to gauge overall system properties. The definitions of these order parameters are introduced below.

（1）The nematic-order correlation function

For rod-like particles with obvious axial effect, the nematic-order correlation function serves to indicate the presence of orientation consistency within their internal structure[160,233].

The global nematic-order correlation function, which measures the degree of orientation order in a single direction, is employed in our study. Specifically, we adopt the airflow direction as our reference direction, and the function is formulated as follows[234]:

$$S_2 = \langle (2cos^2\varphi - 1) \rangle \tag{2.3}$$

Here, φ represents the angle between the long axis of the particle and the direction of the airflow, and the angle brackets denote an average over all such pairs of particles within about 6000 frames of images. The value of S_2 ranges from 1 to -1, where $S_2 = 1$ corresponds to the orientation of the particles is parallel to the direction of airflow, $S_2 = 0$ indicates that the particle orientation is in an isotropic state, and $S_2 = -1$ indicates that the orientation of the particles is perpendicular to the direction of airflow.

The local nematic-order correlation function $G_2(r)$ of particle i is defined as，

$$G_2(r) = \langle (cos2(\theta_i - \theta_j) \rangle \tag{2.4}$$

where θ_i and θ_j are the angles of particles i and j, respectively, i and j sweep over all pairs of particles separated by a distance r[200]. It is equal to 1 if the two particles are parallel and -1 if they are perpendicular to each other.

(2) The tetraic-order correlation function

The tetraic-order correlation function G_4 can be used to describe the parallel or perpendicular arrangement of particles. The calculation formula is as follows[230,235]:

$$G_4 = \langle \cos\left[4(\theta_i - \theta_j)\right] \rangle \tag{2.5}$$

where θ_i and θ_j are the angles of particles i and j, respectively. The cubic order

parameter, G_4, provides valuable quantitative insights into the local structure of rod-like particle fluidization. Specifically, a value of $G_4 = 1$ signifies that the rod particles are in a perfectly ordered structure (i.e., parallel or orthogonal to each other), while a value of $G_4 = 0$ indicates that the particles are in a completely disordered structure.

3 Flow Description of Nonspherical Particles

3.1 Introduction

The study of gas-solid flow characteristics and interaction mechanisms of nonspherical particles in fluidized beds remains limited, leaving many basic dynamic problems, such as flow characteristics and the impact of particle shape on fluidization, unresolved. The lack of understanding of the dynamic characteristics of nonspherical particles, particularly in the case of biomass particles, has emerged as a significant hindrance to their development and practical implementation[2]. Investigating the fluidization behaviours of nonspherical particles in fluidized beds is therefore necessary. As nonspherical particle motion exhibits strong anisotropy, understanding the mechanism of its internal fluidization behavior and analyzing its anisotropic behavior can significantly improve the operation and design of bubbling fluidized beds.

In this chapter, we examine the dynamic characteristics of rod-like particles with typical nonspherical shape characteristics in a bubbling fluidized bed, including pressure drop, bed height, particle velocity, granular kinetic energy, particle temperature, and particle orientation. We investigate the impact of particle shape and superficial gas velocity on the flow behavior of nonspherical particles to reveal the motion mechanism of rod-like particles in the fluidized bed.

3.2 Fluidization regimes

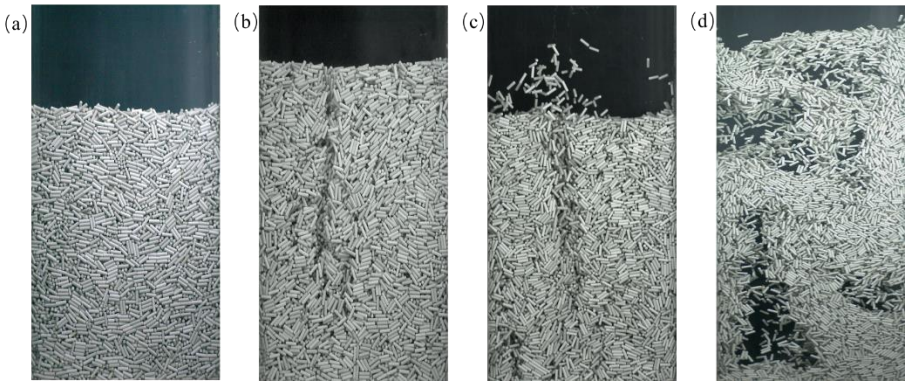

Figure 3.1 Examples of the different fluidization regimes for AR-4 particles(a: Fixed bed; b: Passive channelling; c: Active channelling; d: Bubbling fluidization.).

Characterizing the fluidization regimes offers a detailed depiction of the fluid flow state within the bed. This serves as a critical foundation and an effective tool for analyzing the fluidized bed's performance. Across various gas velocities, different fluidization regimes as described below can be observed, with illustrative examples shown in Figure 3.1. Comparable behavior for elongated cuboids of similar dimensions to the larger particles was also observed by Kruggel-Emden[95].

Figure 3.1(a) depicts a fixed bed, where at low gas velocities, the particles remain stationary and the fluid flows upward through the gaps between the particles. In this state, the drag force of the fluid on the particles is insufficient to overcome gravity[97]. As the gas velocity increases, the original structure of the bed is disrupted, and the fluidized bed enters a passive channeling (Figure 3.1(b)). This state is characterized by

the formation of one or more stable channels within the bed, where the particles remain stationary. Further increase in gas velocity leads to the fluidized bed entering an active channeling (Figure 3.1(c)). At this stage, particles are drawn into the channel from the bottom, forming a fountain. The particles on either side move downward to create an internal circulation mode, while the velocities of particles in other areas are comparatively lower. In contrast to the passive channeling, the channel does not only widen but also collapse rapidly while continually creating new path. These two regimes, active and passive channelings, are observed only in particles with large aspect ratios, possibly due to interlocking between nonspherical particles.

Figure 3.1(d) illustrates a bubbling regime, which is the most common flow pattern observed in single-species particle fluidization and multi-component particle fluidization[114,187,236]. The dominant feature of this regime is the movement of particles by visible bubbles formed from a distributor plate. As these bubbles pass through the bed, the particles are carried along by the wake of the bubbles, causing them to rise. Concurrently, in order to fill the cavity generated after the bubbles passe, the surrounding mixture migrates downward, resulting in a downward flow of particles around the bubble area. This movement of bubbles upward and particles downward generates a particle circulation mode.

3.3 Pressure drop and minimum fluidization velocity

The pressure drop of bubbling fluidized bed is easy to obtain information in industrial and laboratory scale fluidized beds. It can provide important insights into the dynamic characteristics and time-averaged behavior of fluidized beds. Its temporal evolution serves as an indicator of the fluidization state of the bed, making it one of the most commonly used methods for investigating flow characteristics in bubbling fluidized beds.

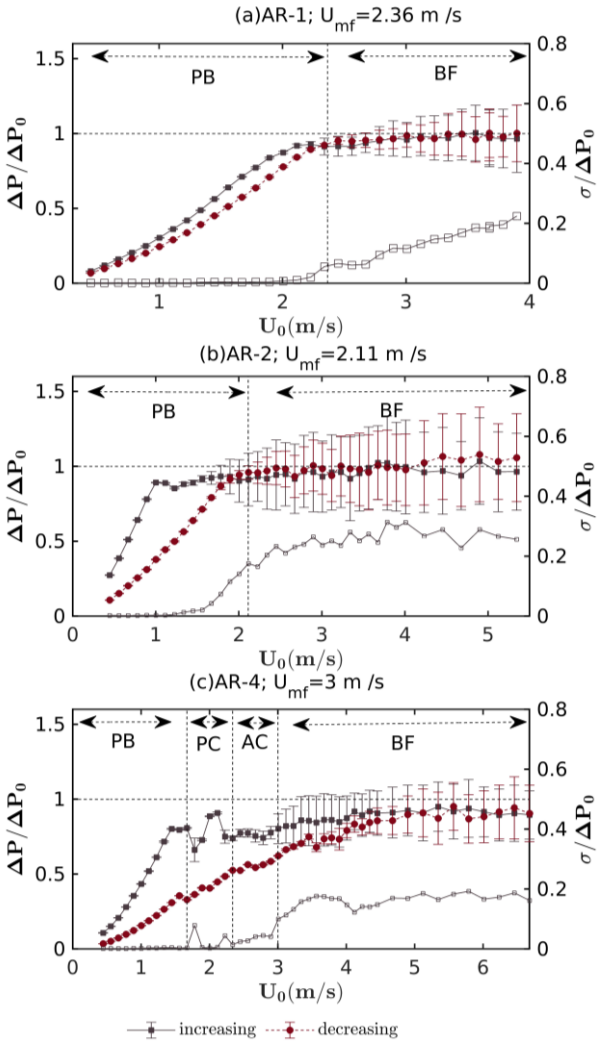

Figure 3.2 Measured pressure drop for AR-1(a), AR-2(b), and AR-4(c) particles. The

filled black square and filled red circle denote the curves of increasing pressure drop and decreasing pressure drop, respectively, both with error bars; the empty squares to the right axes ($\sigma/\Delta P_0$) denote the standard deviation of the increasing pressure drop curves; the horizontal dashlines denote the idealized static pressure drop, whereas the vertical dashlines demarcate the transitions between different fluidization regimes, i.e., packed bed (PB), passive channeling (PC), active channeling (AC), and bubbling fluidization (BF).

Figure 3.2 displays the pressure drop profiles of three types of particles as a function of gas velocity. The pressure drop here is normalized with the idealized pressure drop, ΔP_0, which is determined by the total weight of packing particles[71]. Error bars indicate the standard deviation of the measurement, defined by Eq.3.1. Figure 3.2 indicates a significant effect of particle shape on the pressure drop. This value is around unity for AR-1 particles and AR-2 particles, indicating a full fluidization state has been reached. For AR-4 particles, however, the normalized pressure drop is obviously smaller than unity over the whole range of gas velocity, indicating the occurrence of partial fluidization and even channeling[237], which has been reported to include passive and active channeling[24,95]. As in the literature[95], the channeling(PC and AC in Figure 3.2) is identified by lower than normal pressure drop and stronger fluctuations of pressure drop curve. By integrating visual field observations and standard deviation analysis of the pressure curve, it is evident that during the initial passive channeling phase, pressure fluctuation reaches a local peak before subsequently decreasing. As the superficial gas velocity gradually increases, the pressure fluctuation

gradually increases, and the fluidization regime enters the active channeling. The minimum bubbling ensues after the channeling. The discrepancy between the decreasing and increasing pressure drop curves deteriorates significantly with the increase of the aspect ratio of particles, which may partly be attributed to the quasi-2D bed configuration, as has been reported in the literature[24].

The pressure drop curve can be utilized to determine the minimum fluidization velocity, a fundamental parameter that characterizes particle flow within the fluidized bed. This parameter is influenced by both the geometric parameters of the fluidized bed and the material properties of the particles[39,114,238].U_{mf} and U_{mb} strongly depend on the aspect ratio, χ, from Figure 3.2. As χ increases from 1 to 2, U_{mf} decreases with the increase of χ, and when χ increases from 2 to 4, U_{mf} increases with χ. Likewise, similar dependences are observed in previous studies[23,96,105].

The mean projected face area of particle and voidage fraction in fixed bed for AR-1, AR-2 and AR-3 particles are listed in Table 3.1. It should be noted that since the direction of fluid flow is vertical, so the mean projected face area is the projection area of particles in the x-direction. In the packed bed, the bed porosity and the average projection area of AR-4 particles are larger than those of AR-2 particles as shown in Table 3.1. In general, the drag force is inversely proportional to the porosity and directly proportional to the projected area of the particles. Moreover, for rod-like particles, the

interlocking between particles will lead to the increase of resistance, which is not conducive to the fluidization of particles. As the aspect ratio of particles increases, interlocking becomes more pronounced. This indicates that for rod-like particles, an increase in voidage fraction and interlocking has a more significant impact on bed fluidization compared to an increase in particle projection area. This results in AR-4 particles having a higher minimum fluidization velocity (U_{mf}) than AR-2 particles.

$$\sigma = \sqrt{\frac{1}{N-1}\sum_{i=1}^{N}|A_i - \bar{A}|^2} \quad (3.1)$$ Where σ is the standard deviation and A is a serious of N measurements, of which $\bar{A}$ is the mean value.

Table 3.1 The mean projected face area of individual particle ($A_{\perp}$, (mm^2)) and voidage fraction (ε) in packed bed for AR-1, AR-2 and AR-4 particles.

	AR-1	AR-2	AR-4
$A_{\perp}$	10.1788	13.0679	16.0419
ε	0.2475	0.1977	0.2665

3.4 Bed height

For the design and operation of fluidized bed reactors, Bed expansion ratio (H/H_{mf}) is one of the important parameters[239,240]. Researchers generally believe that the bed expansion during the operation of the bubbling bed is caused by bubbles movement and the expansion of the dense phase, and its essence is a macroscopic

reflection of the movement of particles and bubbles. During fluidization, particles rise due to the driving force of the air flow and fall under the influence of gravity. The position of particles changes over time due to various forces acting on them. The study of bed height is an important aspect in the design of fluidized bed reactors. Therefore, H is used to characterize bed height at different superficial gas velocities[241].

$$H = \frac{2\sum_{i=1}^{N} y_i}{N} \tag{3.2}$$

where y_i represents the vertical coordinate of the centre of mass of particle i and N denotes the total number of particles.

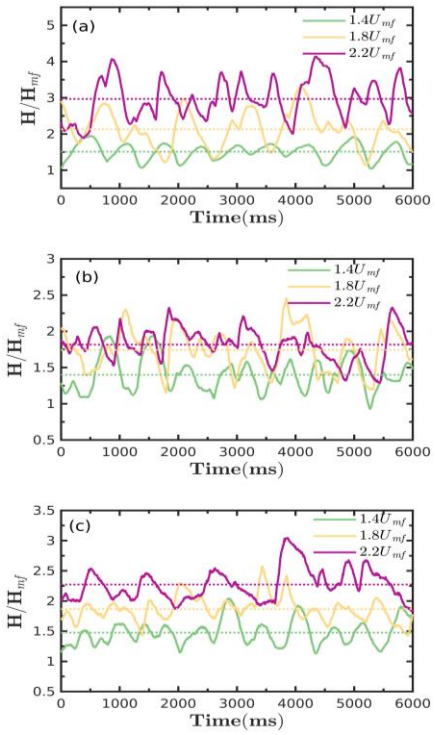

Figure 3.3 Time evolution of the bed expansion ratio at different gas velocities for (a) AR-1, (b)AR-2 and (c) AR-4 particles. The dotted line represents the average bed

expansion ratio.

Figure 3.3 shows the time-dependent the bed expansion ratio curves, where H_{mf} is the average bed height at the minimum fluidization velocity. The bed expansion rate is affected by the gas velocity and particle shape. Particle motion within the bed is significantly influenced by the gas velocity. Increasing the gas velocity results in a greater force being exerted by the gas phase on the solid phase, leading to an increase in bed expansion rate, stronger interaction between the particle phases, more efficient mixing between the gas and particles, and periodic changes in bed expansion rate. As χ increases from 1 to 2, H/H_{mf} decreases with an increase in χ. However, when χ increases from 2 to 4, H/H_{mf} increases with an increase in χ. The impact of aspect ratio on the bed expansion rate is similar to that on the minimum fluidization velocity (Figure 3.2).

3.5 Particle flow characteristics of bubbling fluidized bed

3.5.1 Particle velocity

Particle velocity is a crucial parameter in the study of bubbling fluidized bed flow. During the bubbling fluidization process, particles move in response to the combined effects of buoyancy, drag force, and gravity. Specifically, particles located at the bottom

of the bed rise gradually upward as bubbles form. Once a bubble reaches the top of the bed, it ruptures, causing the particles to move downward due to the force of gravity being greater than the drag force. This results in the formation of a circulating motion of particles within the bed.

When particles in a flow field are subjected to external forces, they not only experience horizontal or vertical motion, but also exhibit rotational motion around their own axis. This rotation does not only affect the particle motion characteristics but also impact the surrounding continuous-phase flow field. Moreover, particle collisions, heat transfer, and mass transfer are among the processes that are significantly affected by this rotational motion[242]. From the perspective of theoretical mechanics, the reason why nonspherical particles rotate is that the particles are affected by the torque in the flow, which is mainly caused by the uneven force of the particles, including the flow field factors such as the velocity gradient and pressure gradient in the local area, as well as the factors such as collision between particles and irregular shape of particles[243].

Studying the velocity in fluidized beds is important to both theoretical investigations of dense gas-solid flows and the development of more accurate simulations of gas-solid multiphase flows. Moreover, particle velocity directly impacts the efficacy of the gas-solid contact, heat and mass transfer processes that occur during thermochemical processes such as combustion, pyrolysis, or gasification. Therefore, it

is a critical parameter for the design of processes, equipment, and control systems. Its practical significance is evident in various industrial applications.

3.5.1.1 Particle velocity profiles

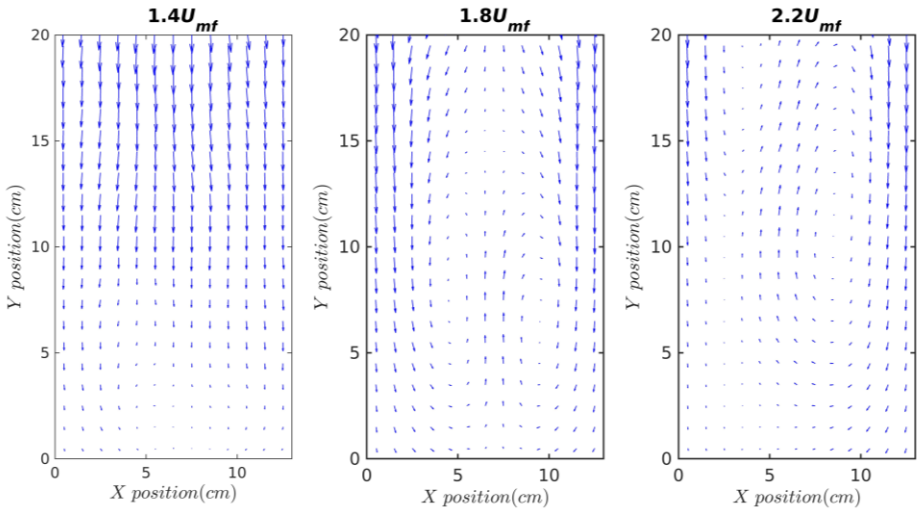

Figure 3.4 Velocity field distribution for AR-1 particles in the X-Y plane for different gas velocities.

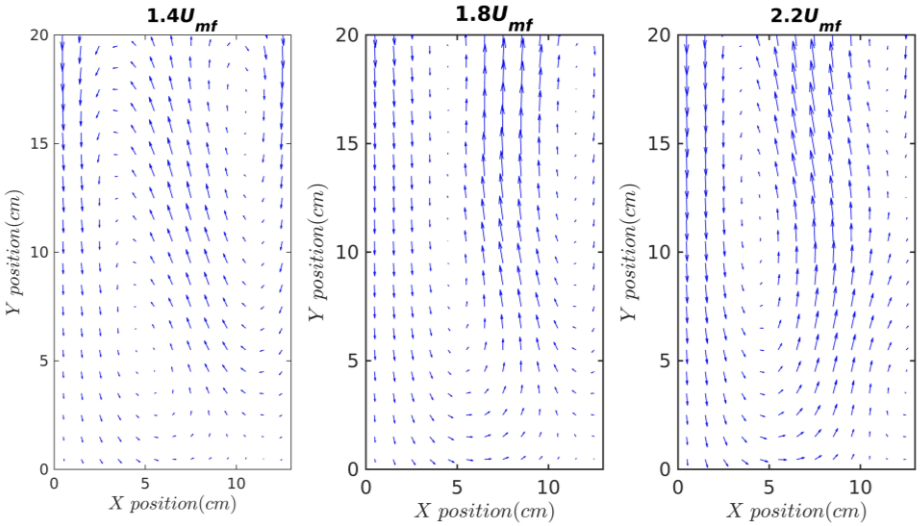

Figure 3.5 Velocity field distribution for AR-2 particles in the X-Y plane for different gas velocities.

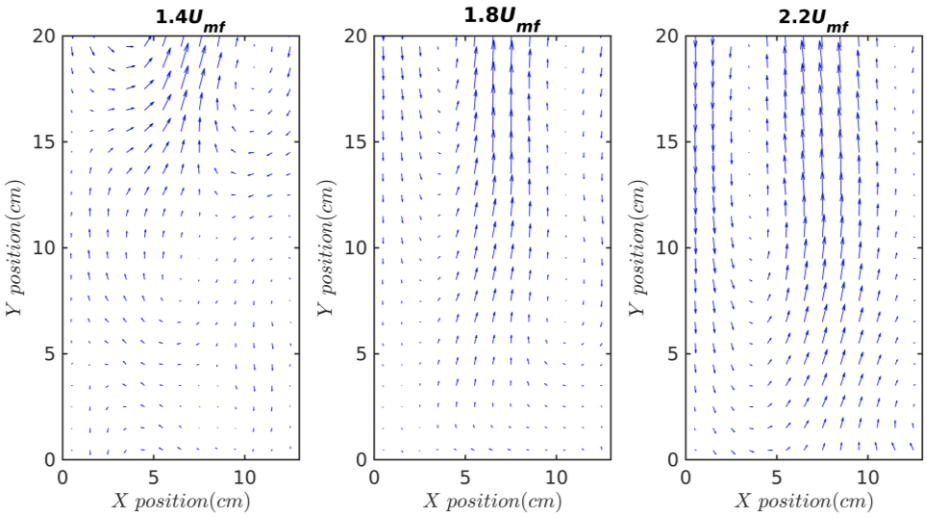

Figure 3.6 Velocity field distribution for AR-4 particles in the X-Y plane for different gas velocities.

Figure 3.4-Figure 3.6 show the velocity field distribution in the X-Y plane for particles of AR-1, AR-2 and AR-4 particles. Although the averaged velocity profiles may appear to be unphysical at first glance, this observation is attributed to the disparity in the timescales between the upward and downward movements of the particles. And the velocity field distribution of particles with different aspect ratios has its own characteristics. However, with the increase of superficial gas velocity, the movement trend of all three types of particles gradually becomes the same, and the particles fall from the middle rising boundary.

For AR-2 particles (Figure 3.5), two circulation cells are observed under different gas velocities. The circulation cells located at the bottom left and the top right at $1.4U_{mf}$ reform to be located in the center of the bed at $1.8U_{mf}$, but the solid

circulation cell observed at the left appears to be larger and dominant. The circulation pattern of $2.2U_{mf}$ is nearly similar as observed for $1.8U_{mf}$. For AR-4 particles (Figure 3.6), there are multiple solid circulation cells at $1.4U_{mf}$. However, with an increase in gas velocity, the circulation pattern gradually becomes similar to that observed for AR-2 particles.

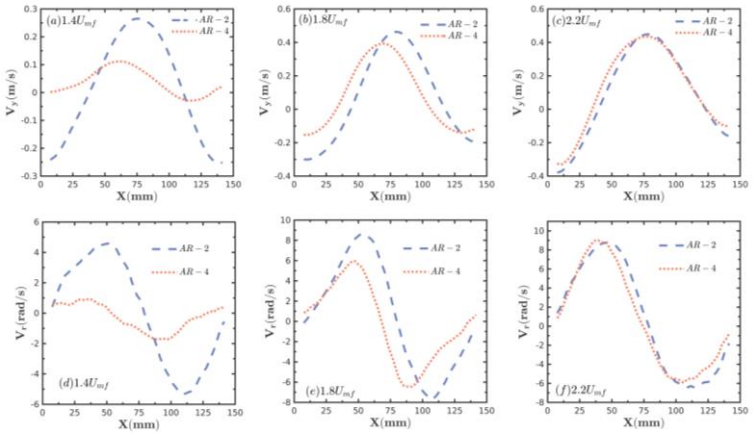

Figure 3.7 Particle vertical velocity V_y and rotation velocity V_r profiles for AR-2 and AR-4 particles.

Figure 3.7 illustrates the profiles of the vertical velocity (V_y) and the rotational velocity (V_r) components for AR-2 and AR-4 particles under different gas velocities. We divide the observation area into 68 bins along the horizontal direction. Each bin has a height of 200 mm and a width of 15 mm. Here, due to measurement limitations, we only consider the rotational velocity of particles around the depth axis passing through its volumetric center and perpendicular to the paper plane. At lower gas velocity, the

velocity distribution of particles with different shapes varies greatly, but at higher gas velocity, the shape has little effect on the velocity profiles of particles. The shapes of AR-2 profiles reflect that particles move upward in the center of the bed and descend near the wall at $1.4U_{mf}$, which is a typical flow pattern of spherical particles in a fluidized bed[244]. However, for AR-4 particles, a large cycle is evident with upward-flowing particles near the left wall and downward-flowing near the right one. That may be attributed to that increasing the aspect ratio makes it difficult for particle configurations to break, and for bubbles to pass through in the bed center. In a qualitative sense, the interlocking in granular materials can be described as a state in which particles or grains lock among themselves and provide additional resistance toward deformation[191]. Consequently, AR-4 particles are not fully fluidized, as shown in Figure 3.7. By comparison, as the gas velocity increases to $2.2U_{mf}$, the velocity profiles between AR-2 and AR-4 particles are close, as shown in Figure 3.7, indicating a similar flow pattern for both particles at full fluidization.

At low gas velocity, V_r of AR-4 particles fluctuates around zero, whereas the V_r profile of AR-2 particle is positive on the left wall and negative on the right one. More concretely, the AR-2 and AR-4 particle rotates anticlockwise on the left side of the bed and clockwise on the right. There is similarity between V_r and V_y profiles of AR-4 particle. Moreover, AR-2 particles have a higher rotational velocity than AR-4 particles.

Nevertheless, at $2.2U_{mf}$ the rotational velocity profiles of the two kinds of particles show similar trends.

3.5.1.2 Particle velocity distribution

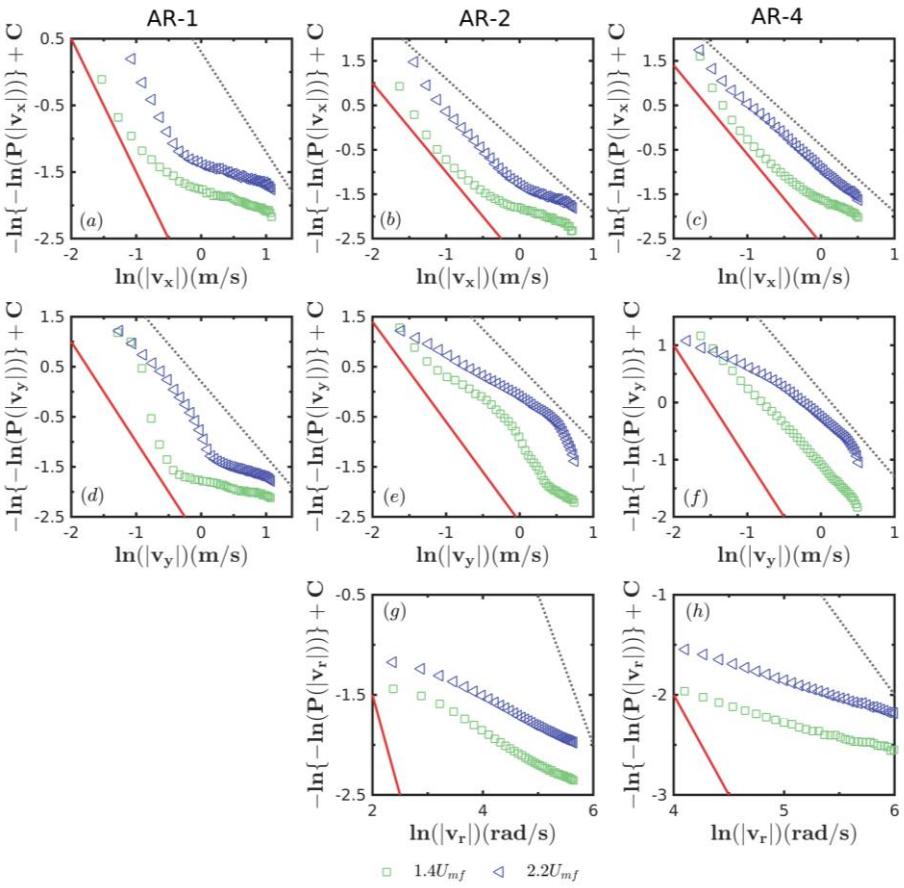

Figure 3.8 The double-logarithmic of velocity distribution for AR-1, AR-2 and AR-4 at different gas velocities. The green and blue symbols represent $1.4U_{mf}$ and $2.2U_{mf}$. The red solid and black dashed lines are lines with slopes of 2 and 1.5, respectively, with respect to $\sim\exp[-\beta(V/\sigma)^2]$ and $\sim\exp[-\beta(V/\sigma)^{1.5}]$; (a, b, c) particle horizontal velocity V_x ; (d, e, f) particle vertical velocity V_y; (g, h) particle rotational velocity V_r.

Figure 3.8 displays the velocity distribution throughout the range of parameters

studied. The velocity distributions are fitted by $P(V) = Cexp[-\beta(V/\sigma)^{\alpha}]$, if we take a log one time, $\ln(P(|V|)) = \ln C - \beta\left(\frac{V}{\sigma}\right)^{\alpha}$. Then we take the log of the above expression again, we have $-\ln(-\ln|P(V)|) + Constant = -\alpha\ln\left(\frac{V}{\sigma}\right)$, then we could observe the slope of the line to judge the distribution type directly. So the red solid line in the figure represents the Gaussian distribution with a slope, $k = -2, \sim exp[-\beta(V/\sigma)^2]$ and the black dashed line represents an exponential distribution with a slope, $k = -1.5, \sim exp[-\beta(V/\sigma)^{1.5}]$. All the velocity distributions are non-Gaussian and yield stretched tails at high speed. The exponential distribution means that the velocity distribution function differs drastically from the Maxwellian distribution for fast particles whose velocities significantly exceed the thermal velocity ($v_1 \gg \sqrt{T}$), which is one of the major non-equilibrium characteristics of dissipative granular systems[245-248]. Generally, the more dissipative, the heavier tail of the velocity distribution. A Maxwellian distribution cannot describe the nonspherical particle behavior in a gas-solid bed. Accordingly, the velocity distributions are fitted by using Gaussian and exponential distributions, i.e., $f \sim exp[-\beta(V/\sigma)^{1.5}]$, and $f \sim exp[-\beta(V/\sigma)^2]$, respectively. To examine the differences between velocity distributions, we plot $-\ln\{-(P(|V|))\}$ instead of $P(V)$. As the aspect ratio increases, the probability of high-populated tails is increased more frequently compared with the Gaussian distribution, and the asymptotics can be observed. It seems $P(V_r)$ deviate much from not only the

equilibrium distribution but also the exponential distribution $f\sim\exp[-\beta(V/\sigma)^{1.5}]$, suggesting it is harder to predict the rotational velocity using the continuum theory. Indeed, as the rotational particle behavior is very important to understand the fluidization of rod-like particles. More efforts are deserved to tackle its complexity as well as its correlation with the linear velocities.

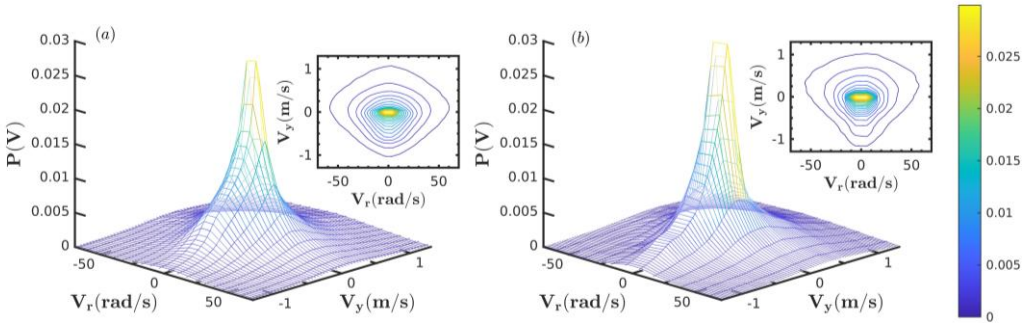

Figure 3.9 A joint probability density function for (a) AR-2 and (b) AR-4 particles under $2.2U_{mf}$.

To relate the rotational and translational velocity, Figure 3.9 presents the joint probability density function of the rotational and vertical velocities for AR-2 and AR-4 particles at $2.2U_{mf}$. It shows that the most probable area is $(-0.1\mathrm{m/s} < \mathrm{V_y} < 0.1\mathrm{m/s})$ and $(-15\ \mathrm{rad/s} < \mathrm{V_r} < 15\ \mathrm{rad/s})$ for both AR-2 and AR-4 particles. $\mathrm{V_r}$ is symmetric, while $\mathrm{V_y}$ asymmetric. Especially for AR-4, the rotation rate $\mathrm{V_r}$with $\mathrm{V_y} > 0$ is larger than $\mathrm{V_r}$ with $\mathrm{V_y} < 0$. That is, the upward moving particles have a higher rotational velocity than those downward. This asymmetry increases with the aspect ratio. The possible reason is that the particles with a larger aspect ratio need more space to rotate,

which may be easier to obtain larger rotational velocity during the rise due to larger upward airflow and agitation, as compared to the lower gas flow near the wall for descending particles.

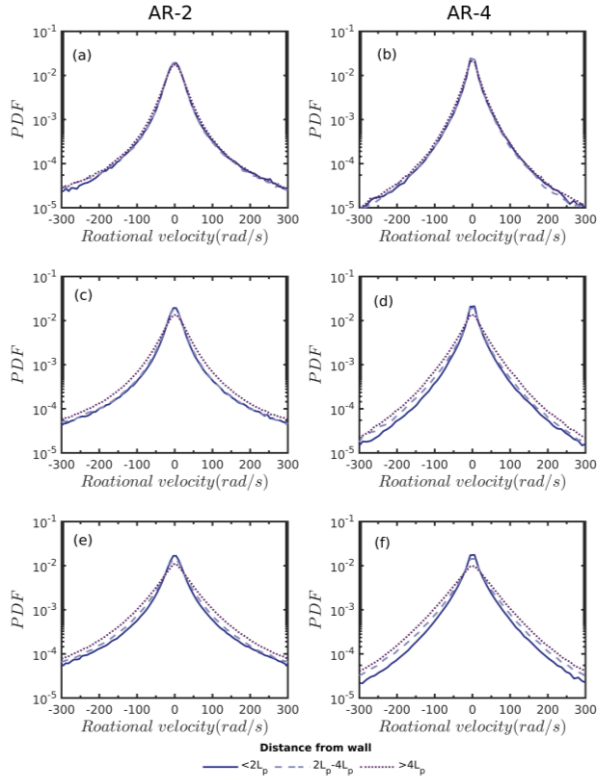

Figure 3.10 Particle rotational velocity for different locations for AR-2 particles and AR-4 particles under different gas velocity. (a,b) $1.4U_{mf}$; (c,d)$1.8U_{mf}$; (e,f)$2.2U_{mf}$.

Due to the inhibitory effect of the boundary on the rotation of rod-like particles, we conducted a study on its impact on the rotation velocity. To achieve this, we divide the fluidized bed into three sections according to the distance from the wall, i.e., $<2l_p$, $2\sim4l_p$, and $>4l_p$, to study the effect of the sidewall on rotation velocity. Figure 3.10 shows the probability density distribution of rotation velocity at different positions.

With the increase of gas velocity, the influence of boundary on rotation velocity is gradually obvious. At lower gas velocities, particles within the bed or at the boundary experienced mild fluidization, resulting in fewer particle collisions and thus less frequent orientation changes. Consequently, particle rotation velocity was small and the boundary had minimal impact on rotation velocity. However, as superficial gas velocity gradually increased, orientation changes became more frequent, leading to larger changes in rotation velocity and a greater influence of the boundary on rotation velocity.

3.5.1.3 RMS distribution

Gas-solid two-phase flow typically exhibits anisotropic distribution, and the root mean square (RMS) distribution is commonly used to characterize the random and fluctuating behavior of particle velocity. By calculating the RMS ratio of particle velocity in different directions, it is possible to investigate the isotropy of flow in gas-solid two-phase flow systems. Specifically, the ratio of RMS of the instantaneous vertical velocity to RMS of the instantaneous horizontal velocity serves as a metric for quantifying the isotropy of the system, with a value closer to 1 indicating a more isotropic behavior of the system[183,249].

$$\frac{v_{\mathrm{y,RMS}}}{v_{\mathrm{x,RMS}}} = \frac{\sqrt{\frac{1}{N-1}\sum_n^N (v_{\mathrm{y}}(n) - \overline{v_{\mathrm{y}}})}}{\sqrt{\frac{1}{N-1}\sum_n^N (v_{\mathrm{x}}(n) - \overline{v_{\mathrm{x}}})}} \tag{3.3}$$

where v represents the instantaneous velocity, $\bar{v}$ represents the average velocity, and

N represents the number of particles.

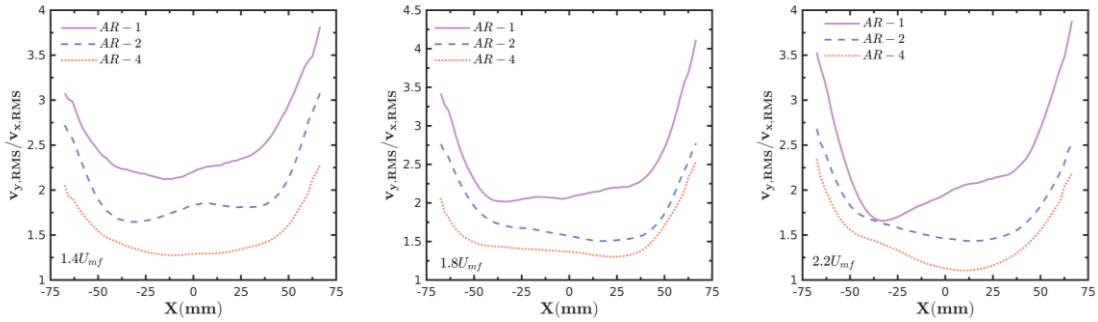

Figure 3.11 Isotropy distribution based on RMS of particle velocities.

Figure 3.11 shows the ratio of the RMS of the vertical velocity of the three types of particles to the RMS of the horizontal velocity. If the ratio is closer to 1, the system behavior is more isotropic. For all the cases, the ratio of the RMS is closer to 1 in the central region of the bed, indicating that the isotropic effect of gas-solid flow in this region is stronger. At other locations, the ratio of the RMS deviates from 1, indicating that the isotropic effect of gas-solid flow in this region is weak. Notably, the ratio of the RMS is the largest near the side wall, indicating that the anisotropic characteristics of the particle velocity are the most obvious. Moreover, for the same gas velocity, the aspect ratio had a certain influence on the ratio, which was more significant.

3.5.2 Translation and rotational kinetic energy

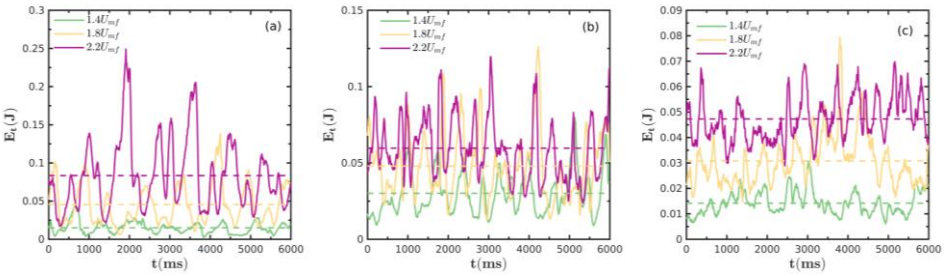

Figure 3.12 Translational kinetic energy at different gas velocity for (a) AR-1, (b) AR-2 and (c) AR-4 particles. The dotted line represents the average kinetic energy of the particles.

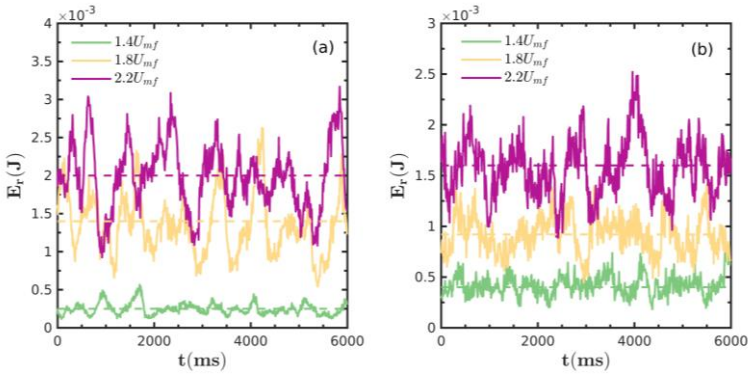

Figure 3.13 Rotational kinetic energy at different gas velocity for (a) AR-2 and (b) AR-4 particles. The dotted line represents the average kinetic energy of the particles.

Figure 3.12-Figure 3.13 shows the time series of the rotational and translational kinetic energy of AR-1, AR-2, and AR-4 particles under different gas velocities. The rotational and translational kinetic energies are given by

$$E_r = \frac{1}{2} I_p V_r^{\ 2} \tag{3.4}$$

$$E_t = \frac{1}{2} m_p (V_x^{\ 2} + V_y^{\ 2}) \tag{3.5}$$

where I_p represents the particle moment of inertia, V_r denotes the rotational velocity, and m_p stands for the particle mass. The translational energy is almost 2-orders magnitude larger than that of the rotational energy. In all cases, the kinetic energy of the particles increases with the gas velocity. From the average kinetic energy, we can see the big effect of gas velocity on the rotational and translational behavior of particles. This phenomenon can be attributed to the closer contact mode and interlocking effect of rod-like particles, which in turn leads to the formation of a more stable structure. Consequently, as the aspect ratio increases, a greater amount of kinetic energy is required to facilitate the flow[105,226].

Regarding the rotational kinetic energy of rod-like particles, it is worth noting that they tend to rotate when in contact with the fluid and surrounding particles. At low gas velocities, the kinetic energy of the gas is insufficient to trigger particle rotation, resulting in a relatively small rotational kinetic energy. However, as the superficial gas velocity gradually increases, the bed interior becomes relatively looser and the gas's kinetic energy increases. This increase in kinetic energy promotes particle rotation, leading to a larger rotational kinetic energy.

3.5.3 Granular temperature

Granular temperature is a fundamental concept in particle systems and plays a crucial role in characterizing the degree of particle activity in fluidized beds. It reflects the strength of particle pulsating motion, and the fluidization characteristics of particles strongly depend on the motion state of particles[250,251]. Since particles have both translational and rotational velocities, their fluctuation includes both translational and rotational velocity fluctuation. In terms of granular temperature, it can be divided into translational and rotational components, which reflect the turbulent characteristics in the translational motion of particles and the fluctuation characteristics of their rotational velocity, respectively[252]. Therefore, it is feasible to infer the motion behavior of particles in fluidized beds based on the distribution of granular temperature.

The granular temperatures are defined by[71,253,254]

$$\mathrm{T_t(t)} = \frac{1}{\mathrm{N}}\sum_{\mathrm{i=1}}^{\mathrm{N}}[(V_x^i(\mathrm{t}) - \bar{V}_x(\mathrm{t}))^2 + (V_y^i(\mathrm{t}) - \bar{V}_y(\mathrm{t}))^2]/2 \qquad (3.6)$$

$$\mathrm{T_r(t)} = \frac{1}{\mathrm{N}}\sum_{\mathrm{i=1}}^{\mathrm{N}}[(V_r^i(\mathrm{t}) - \bar{V}_r^i(\mathrm{t}))^2]^2 \qquad (3.7)$$

where $V_x^i(\mathrm{t})$ are instantaneous velocity x-component of particle i and $\overline{\mathrm{V}}_{\mathrm{x}}^{\mathrm{i}}(\mathrm{t})$ instantaneous mean particle velocity, e.g., $\overline{\mathrm{V}}_{\mathrm{x}}(\mathrm{t}) = \frac{1}{\mathrm{n}}\sum_{\mathrm{i=1}}^{\mathrm{n}} V_x^i(\mathrm{t})$, N is the particle number in one frame, and so are the other components.

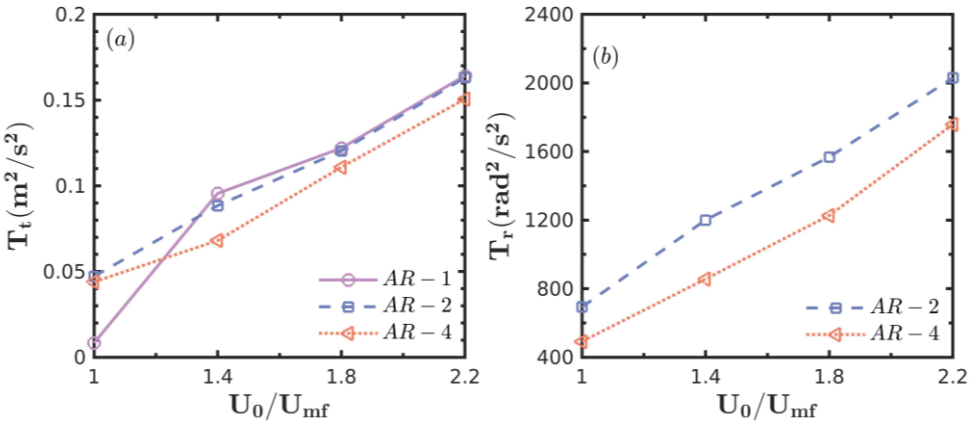

Figure 3.14 Granular temperature of different components for AR-1, AR-2 and AR-4 particles with different gas velocities: (Left) the translational temperature, T_t (Right) the rotational temperature, T_r.

Figure 3.14 depicts the granular temperature for three types of particles. Generally, the granular temperature increases monotonically with the gas velocity, whereas the rotational temperature is affected more by the aspect ratio than the translational temperature is. That also suggests a stronger nonequilibrium behavior with respect to the rotational component. It is found that the rotational temperature of AR-2 is higher than that of AR-4, which implies a larger aspect ratio of particles make it harder to get the rotation energy.

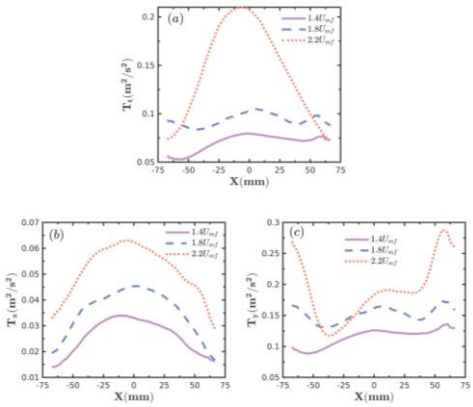

Figure 3.15 Distribution of particle translational granular temperature distribution for AR-1 particles. (a) $x-y$ direction; (b)x-direction;(c) y-direction.

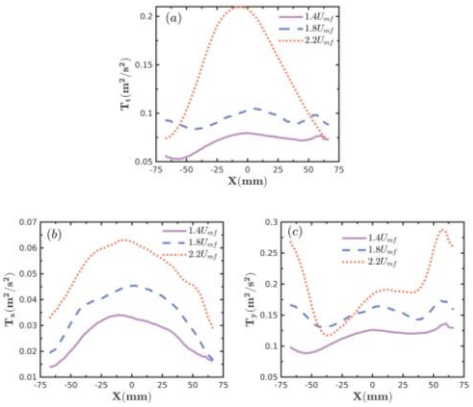

Figure 3.16 Distribution of particle translational granular temperature distribution for AR-2 particles. (a) $x-y$ direction; (b)x-direction;(c) y-direction.

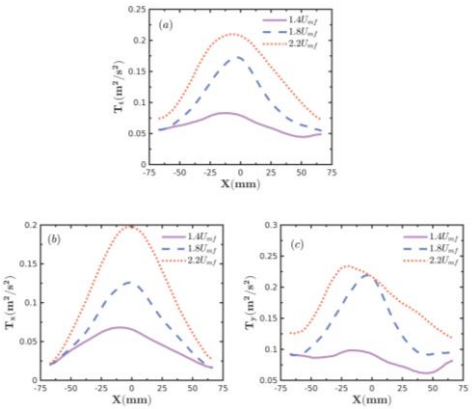

Figure 3.17 Distribution of particle translational granular temperature distribution for

AR-4 particles. (a) $x-y$ direction; (b)x-direction;(c) y-direction.

Figure 3.15-Figure 3.17 present the results of quantitative analysis on the distribution of particle translational granular temperature in the bubbling bed. The figures reveal that as the gas velocity increases, so does the particle translational granular temperature. Regarding the $x-y$ direction, granular temperature is larger near the center of the bed for all three different aspect ratios, while it is smaller on both sides of the bed, but slightly larger near the wall of the bed. This observation suggests that the particle velocity fluctuation is more intense at the center of the bed, followed by the side walls on both sides. Concerning the x-direction, the particle temperatures of the three different aspect ratios are symmetrically distributed. As for the rod-like particles, the trend of granular temperature distribution in the x direction is similar to that in the y direction, with slight differences. Moreover, the granular temperature in the y direction is slightly higher than that in the x direction.The distribution of granular temperature in both directions is convex. In the case of spherical particles, the granular temperature is larger on both sides of the bed in the y direction. In summary, the shape and superficial gas velocity are key factors that impact the velocity fluctuation of the particles, and changes in the gas velocity and shape lead to a corresponding variation in the fluidization state of the bed.

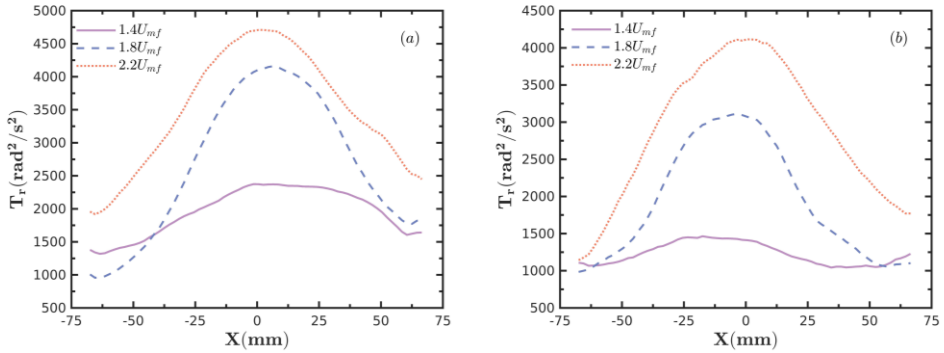

Figure 3.18 Distribution of particle rotational granular temperature distribution for (a)AR-2 particles and (b) AR-4 particles.

Figure 3.18 shows the particle rotational granular temperature distribution of particles. The temperature of the rotating particles is larger near the center of the bed and smaller on both sides of the bed. The distribution trend is similar to particle translational granular temperature. The fluctuation of particle velocity affects the exchange of momentum and energy in the bed. Therefore, the fluctuation intensity of particle velocity in the region with small particle temperature can be appropriately strengthened to achieve more uniform momentum transfer and energy transfer in the bed. At the same gas velocity, the rotational particle temperature of AR-2 is higher than that of AR-4, but the distribution trend of the two particles is basically the same. With the increase of superficial gas velocity, the rotational particle temperature of the particles also increases. The distribution trend is similar under different superficial gas velocity conditions, that is, it is larger in the central region of the bed and smaller near the boundaries.

3.5.4 Particle orientation

The most significant difference between spherical particles and nonspherical particles is the orientation[96] and rotation of particles. For isotropic spherical particles, the force when facing fluid and other particles is not affected by particle orientation. Conversely, when rod-like particles with different orientations are in contact with the same incoming fluid and other particles, the force and torque of rod-like particles will change, resulting in differences in the behavior of individual particles. Additionally, alterations in the orientation distribution of rod-like particles within a bed can lead to changes in the flow structure and pattern of the entire bed, thereby affecting mass and heat transfer between particles or between particles and the fluid. The orientation distribution is a key feature to study the fluidization of nonspherical particles. Therefore, studying the orientation distribution in a fluidized bed is a crucial step in comprehending fluidization of nonspherical particles. The orientation of rod-like particles is examined in this section.

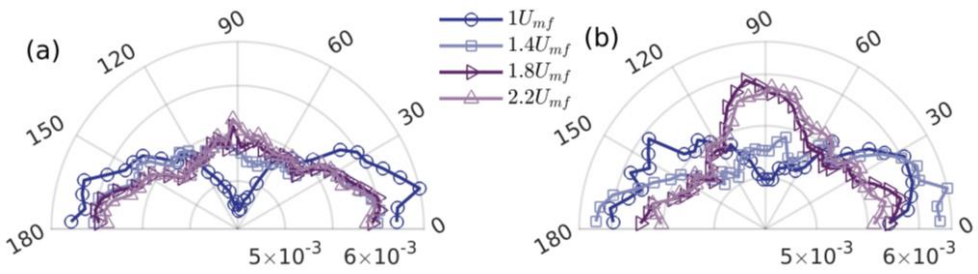

Figure 3.19 Probability distribution function of particle orientation under different gas

velocities. (a) AR-2 particles; (b) AR-4 particles.

Figure 3.19 presents the probability distribution function of particle orientation under different gas velocities. At gas velocities of $1U_{mf}$ and $1.4U_{mf}$, AR-2 particles are dominated by the horizontal direction. At low superficial gas velocities, the orientation of the particles remains the state of the fixed bed due to the milder fluidization conditions and reduced collisions between particles. As the superficial gas velocity increases, the rod-like particles tend to align their long axis parallel to the direction of fluid flow, but horizontal orientation is still dominant in the bed. The phenomenon is different for AR-4 particles, where horizontal orientation is dominant in the bed at U_{mf} and $1.4U_{mf}$, but at higher gas velocities, vertical particles dominate. Generally speaking, under the action of gravity, rod-like particles should tend to be in a relatively stable horizontal state[176]. At lower gas velocities, the orientation distributions of AR-2 and AR-4 are similar in the sense that particles exhibit strongly horizontal alignment in the bed. When the gas velocity is $2.2U_{mf}$, the drag force, not the gravity, becomes dominant. The stable state thus tends to be vertical alignment to avoid higher resistance or drag force[21,228]. Nevertheless, when the gas velocity reaches a certain value, the orientation does not change anymore, which is consistent with previous observations[78,105].

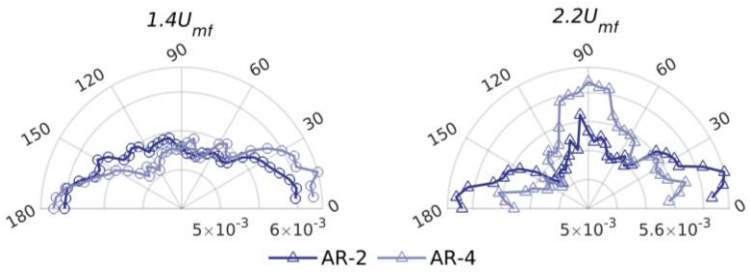

Figure 3.20 Probability distribution function of particle orientation under different particle shape (a)$1.4U_{mf}$; (b) $2.2U_{mf}$.

To gain a deeper understanding of the orientation of particles within a fluidized bed, the influence of particle shape was studied. Figure 3.20 shows effect of particle shape on orientation distribution. At a low gas velocity of $1.4U_{mf}$, the orientation distribution of the two particles is similar, and the particles tend to be arranged horizontally in the bed. This is because most of the particles are in a static or gentle fluidization state, and the rod particles cannot obtain enough energy and space to change their orientation significantly. As a result, the orientation distribution of the two particles is not much different and tends to be horizontal. However, at a higher superficial gas velocity of $2.2U_{mf}$, an increase in vertically oriented particles is observed, and the difference in orientation distribution between the two particles becomes larger. For AR-2 particles, most particles tend to be horizontally oriented, but they also exhibit a significant tendency towards vertical orientation. In contrast, for AR-4 particles, the particles are more inclined to vertical orientation.

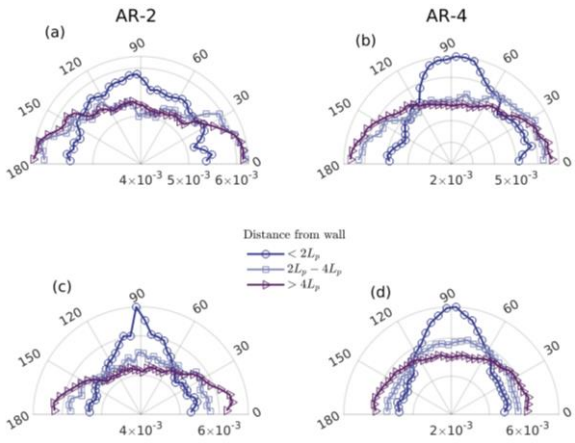

Figure 3.21 Probability distribution function of particle orientation for different locations for AR-2 particles and AR-4 particles. (a, b) $1.4U_{mf}$; (c, d) $2.2U_{mf}$.

Considering that the wall dramatically influences the orientation of nonspherical particles[79,174], we divide the fluidized bed into three sections according to the distance from the wall, i.e., <2l_p, 2~4l_p, and >4l_p, to study the effect of the sidewall on particle orientation. Figure 3.21 shows the particle orientation distributions in different sections under two gas velocities. A clear difference is observed owing to the influence of the wall under both gas velocities. The particle orientation near the sidewall tends to be parallel to the vertical direction. At higher gas velocity, boundary effects are more pronounced.

Due to the collisions between particles and between particles and boundaries in the fluidized bed, the orientation of particles becomes more randomized. To quantify the degree of order in the particle orientation, The global nematic-order correlation function S_2 is used to describe the overall degree of orientation order.

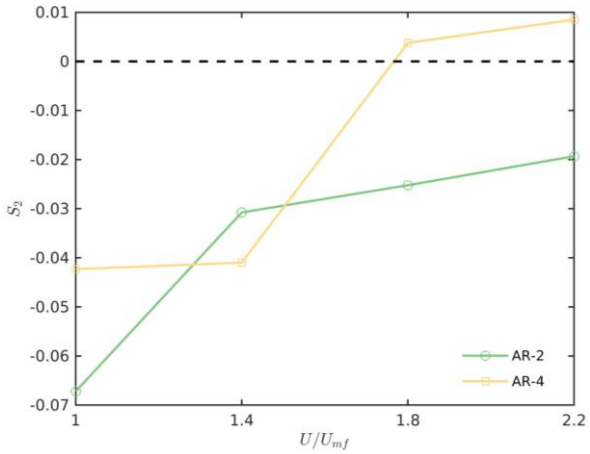

Figure 3.22 The global nematic-order correlation function for AR-2 particles and AR-4 particles with different gas velocity.

Figure 3.22 illustrates the impact of gas velocity on the overall degree of orientation order for AR-2 and AR-4 particles. In all cases, S_2 remains close to 0, indicating that the overall orientation of particles in dense gas-solid two-phase flow systems with nonspherical particles tends to be disordered. At lower gas velocities, S_2 is negative, indicating that the orientation of the particles tend to be perpendicular to the direction of airflow. As the gas velocity increases, S_2 gradually increases, signifying a gradual decrease in horizontally oriented particles. For AR-2 particles, S_2 always remains negative, indicating that although the proportion of horizontally oriented particles gradually decreases, they still remain dominant. Conversely, for AR-4 particles, when the gas velocity exceeds $1.8U_{mf}$, the S_2 of the particles gradually becomes positive, suggesting that vertically oriented particles are dominant, and this trend continues to increase with the gas velocity. For particles with a higher aspect ratio,

they tend to align parallel to the airflow at higher gas velocities.

It can be seen from Figure 3.21 that the boundaries have an effect on the orientation of particles. Therefore, we need to explore the influence of boundary effects on the global nematic-order correlation function.

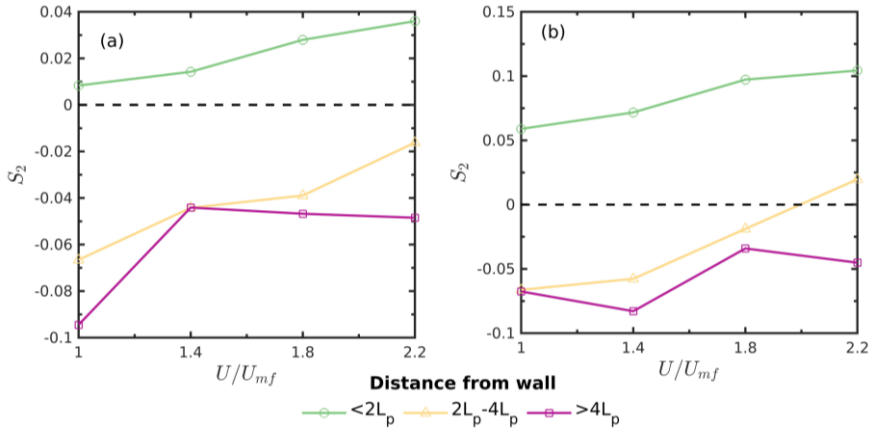

Figure 3.23 The global nematic-order correlation function for different locations for (a)AR-2 particles and (b)AR-4 particles.

We divide the fluidized bed into three sections according to the distance from the wall, i.e., <2l_p, 2~4l_p, and >4l_p, to study the effect of the sidewall on the global nematic-order correlation function. From the diagram, it is evident that S_2 is larger in the boundary region compared to the central region. As the particle position gradually moves away from the boundary, S_2 gradually decreases. This indicates that the particles in the boundary area tend to be more orderly.

3.6 Summary

This chapter presents a comprehensive investigation of the fluidization behavior of rod-like particles using experimental methods. The primary research findings and conclusions are summarized as follows:

(1) Compared to particles with smaller aspect ratios such as AR-1 and AR-2, AR-4 tend to form channel flow, while the other two particles smoothly transit to the bubbling regime. The channeling flow can be divided into two types: passive channeling and active channeling. Additionally, the minimum fluidization velocity initially decreases and then increases with increasing aspect ratio. The impact of particle aspect ratio on the bed expansion rate is similar to that on the minimum fluidization velocity.

(2) At lower gas velocities, the fluidization behavior in the fluidized bed becomes more apparent with decreasing aspect ratio of particles, leading to the formation of regular internal circulation where particles tend to move upward from the middle of the bed and downward near the boundary. The rotational velocity (V_r) of AR-4 particles fluctuates around zero, while the AR-2 particles exhibit centrosymmetric behavior. At high gas velocities, the particle shape has minimal effect on particle velocity distribution. As superficial gas velocity increases, particle fluctuation becomes more active, and the rotational temperature is more influenced by the aspect ratio than the

translational temperature. Moreover, as the aspect ratio increases, the flow requires higher kinetic energy.

The orientation distribution of rod-like particles is influenced by various factors including the aspect ratio, fluidization gas velocity, and particle location. At the gas velocity of 0, the long axis of the particles tends to be horizontal, but this tendency weakens after fluidization. As the fluidization state is established, the number of particles aligned parallel to the fluid direction increases. At high gas velocities, for AR-2 particles, although the number of particles aligned parallel to the fluid direction increases, most particles remain horizontally oriented. However, for AR-4 particles, most particles tend to be aligned vertically. Notably, a clear wall effect is observed during fluidization, where the long axis of rod-like particles located near the wall is more likely to be oriented in the vertical direction compared to those located in the middle region of the bed.

4 Configuration-Dependent Dynamics of Nonspherical Particles

4.1 Introduction

Particles exist in the form of dispersed particles or particle clusters[255-257]in gas-solid fluidized beds. When nonspherical particles come into contact, they may additionally form an interlocking structure that limits their relative motion besides local cluster structure[258,259]. The interaction between the gas phase, discrete particle phase, and particle cluster phase results in a more complex gas-solid two-phase flow[260,261] that may further change the dynamics, mass transfer, and heat transfer characteristics in fluidized beds.

In this chapter, the rod-like particles with different aspect ratios are studied experimentally. The configuration of particles is quantified in terms of the radial distribution function, coordination number and order parameters. The typical particle structures and their dynamics can be addressed precisely by identifying the so-called “super-particles”.

4.2 The configuration of particles

4.2.1 Coordination number

An important reason for the wide application of fluidized beds in industry is the

rapid heat transfer between particles and fluid as well as between particles[96]. The contact between particles or between particles and side walls plays a very important role in flow dynamics, and can reflect the anisotropy of different granular materials to a certain extent. The coordination number (CN) is widely used to characterize the internal structure of particles[24,104,262-264], which is closely related to the heat transfer and chemical reactions between particles. In this work, the coordination number is defined as the number of neighbors particles in a $2l_p \times 2l_p$ region around one reference particle as in the literature[24,97].

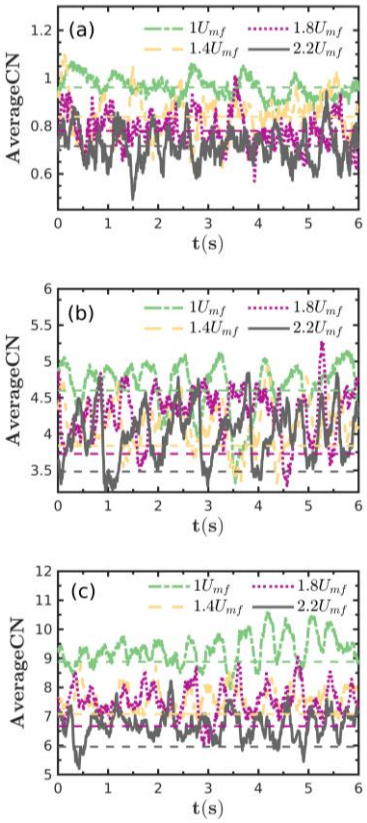

Figure 4.1 Variation of bed averaged CN with time with different superficial gas

velocity for(a) AR-1, (b)AR-2 and (c)AR-4. The dotted line represents the average CN of the particles.

Figure 4.1 displays the time series of the average coordination number, i.e., the average CN for AR-2 particles and AR-4 particles. It can be seen that the coordination number fluctuates around a particular value, depending on the intermittent appearance of voids or bubbles[96]. This specific value depends on the particle shape and gas velocity. As the aspect ratio of the particles gradually increases, the average coordination number gradually increases. This shows that for rod-like particles, when the experimental conditions are the same, the larger the aspect ratio, the greater the probability of particle contact. Onsager calculated the ratio of excluded volume to particle volume between two rod-like particles ($V_{ex}/V_p = 2\pi + 3 + 2(l_p/d_p) + (\pi/2)(d_p/l_p)$)[97,265,266]. For AR-2 particles, V_{ex}/V_p is 14.0686; for AR-4 particles, V_{ex}/V_p is 17.6759. That is to say, a higher aspect ratio results in a larger excluded volume, which would, in turn, lead to a greater likelihood of contact with other particles. The results demonstrate that the particle shape plays an important influence in the heat transfer behavior between particles. Furthermore, the average coordination number of particles decreases with an increase in gas velocity. This is because as the superficial gas velocity increases, the average bed height becomes larger, which reduces the contact between particles.

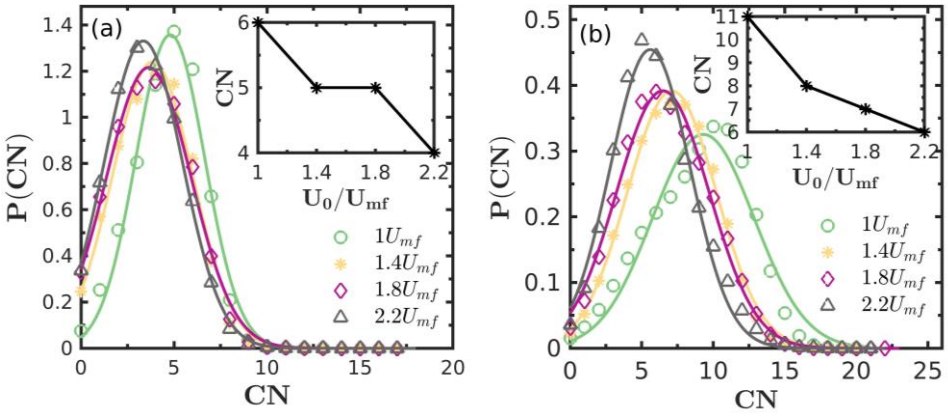

Figure 4.2 Probability density distribution of CN under different superficial gas velocities for (a) AR-2 and (b) AR-4 particles.

Figure 4.2 further displays CN probability density distribution under different superficial gas velocities. It is worth nothing that the probability density distribution of coordination number can be well fitted by Gaussian distribution.

As shown in the figure, the probability density distribution of rod-like particles is approximately a Gaussian distribution. As the gas velocity increases, the energy input into the system causes most of the particles in the system to move violently, resulting in an increase in the average bed height and a gradual decrease in its most likely value. The wider the probability density distribution function of the coordination number, the longer the aspect ratio, and the fewer particles with a coordination number of 0.

For AR-4 particles, most particles have 3-10 neighbors, while most AR-2 particles have 2-5 neighbors. Therefore, under the same conditions, the particles with a longer

aspect ratio are less likely to fluidize, which reflects that the steric interaction makes the particles with a longer aspect ratio easier to contact each other during the fluidization process.

4.2.2 Radial distribution function

Above CN only reflects statistics of the particles within a fixed distance, to better understand the inter-particle spatial correlation, we investigate the radial distribution function (RDF)[104,192,267-269], which is commonly used to represent the structure in fluid-particle systems and can help analyze the typical particle arrangement caused by the shape and orientation of the particles[269]. RDF, $g(r)$, is the probability of finding one particle center at a distance (usually, radius) for a given particle, i.e.,

$$\mathrm{g(r)} = \langle \frac{N(r+\Delta r)}{2\pi r \Delta r \rho_0} \rangle \tag{4.1}$$

where $\mathrm{N}(r+\Delta r)$ is the number of particles at a distance between r and $r+\Delta r$ from the center of a given particle. ρ_0 is the average number of rod-particles per unit area. The angle brackets denote an average over all such pairs of about 6000 frames of images.

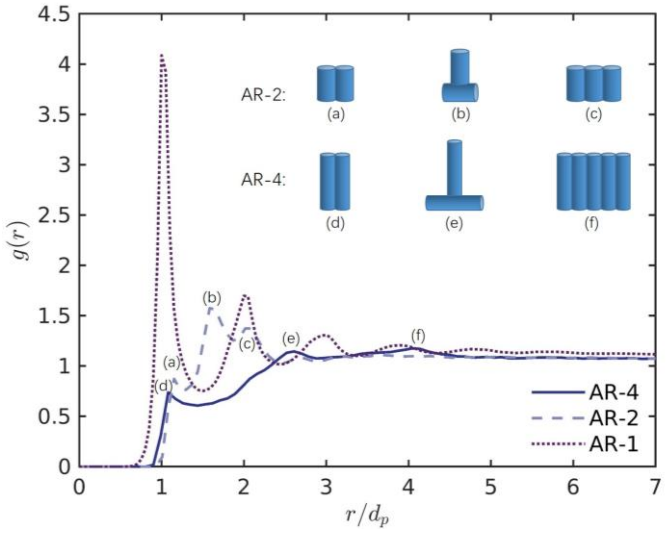

Figure 4.3 Radial distribution functions g(r) for different particle shapes at $1.8U_{mf}$. The inset shows typical particle configuration of AR-2 and AR-4 particles.

Figure 4.3 shows the radial distribution function g(r) of rod-like particles with different aspect ratios at a gas velocity of $1.8U_{mf}$. The distance is normalized by d_p. The inset shows typical particle configurations with respect to the peaks on the RDF curves. For AR-1, spherical particles, g(r) exhibits typical short-range order characteristics, with a sharp peak at $r/d_p = 1$ and three lower peaks successively at $r/d_p = 2, 3, 4$. With the increase of the aspect ratio, the shape of the particles gradually deviates from the sphere, and the first peak value becomes lower than that of the sphere. That is easy to understand as, for spherical particles, six particles are allowed to exist around a given particle, whereas for rod-like particles, only two sides are allowed at the closest contact position for a given particle.

The reduction in these peak values implies that rod-like particles have a poorer short-range ordered structure than spherical particles. The first peak locations for particles of different aspect ratios are the same, suggesting that particles tend to parallel along their long faces. In all these particle configurations with respect to those peaks, the rod-like particles are parallel along their long edges or perpendicular to each other. They are relatively stable mechanical structures as the particles contact with each other by an edge, not a point. Interestingly, there is no configuration of three particles set side by side for AR-4 particles as is for AR-2, implying such a three-particle side-by-side configuration is not stable for AR-4. In fact, at the low gas velocity of $1.0U_{mf}$, the AR-4 three-particle side-by-side configuration exists, as identified by the additional shoulder at $r/d_p = 2$ in Figure 4.4(b). However, as the gas velocity increases, this configuration vanishes, indicating the instability effects of the gas velocity.

To identify the dependence of g(r) on U_{mf}, Figure 4.4 shows the radial distribution functions of rod-like particles for AR-2 and AR-4 at different gas velocities. It is clear that most locations of peaks remain essentially unchanged, while the peak values decline, indicating that the increase of gas velocity breaks the configuration formed between particles and the short-order reduction.

Generally, the RDF decays and its peaks gradually disappear with increasing aspect ratio and gas velocity, finally collapsing to a line, i.e., the nonstructural value.

That is easy to understand as the larger the aspect ratio, the larger the exclusion volume and the collision frequency, the harder it is for the particles to form an ordered configuration. Moreover, it is well known that gas-solid fluidization is inherently heterogeneous, making it difficult to maintain a specifically uniform flow field condition on a large scale, thus this decaying RDF phenomenon becomes more pronounced with increasing aspect ratio and gas velocity. In other words, particles become more uniform (i.e., no preference on specific configuration) with increasing aspect ratio and gas velocity[198,201]. It is also interesting to note that particles tend to align within a distance of one particle length[24]. That is to say, the three-particle side-by-side configuration is more stable for AR-2 and five-particle side-by-side configuration is more stable for AR-4.

The above[270] configurations can be classified into two types: parallel (configurations a, c, d, f in Figure 4.3, referred to as α) and perpendicular ones (configurations b, e in Figure 4.3, referred to as β). When rods are parallel, the excluded volume is minimal ($2\pi l_p d_p^2$), while being perpendicular is maximal ($2l_p^2 d_p$). As the entropy per rod equals $k_B$ln(V/N), where k_B is Boltzmann's constant (for N rods in volume V)[270], α arrangement has higher translational entropy and lower orientational entropy, but β is opposite, having higher orientational entropy and lower translational entropy. For any process, we can expect that one type of entropy decreases, then the

other increases such that the total entropy becomes larger. The second law of thermodynamics seems still works. In other words, the isotropic-nematic transition is accompanied by an entropy increase. Hence, in a fluidized bed, a higher probability of above two configurations is reasonable.

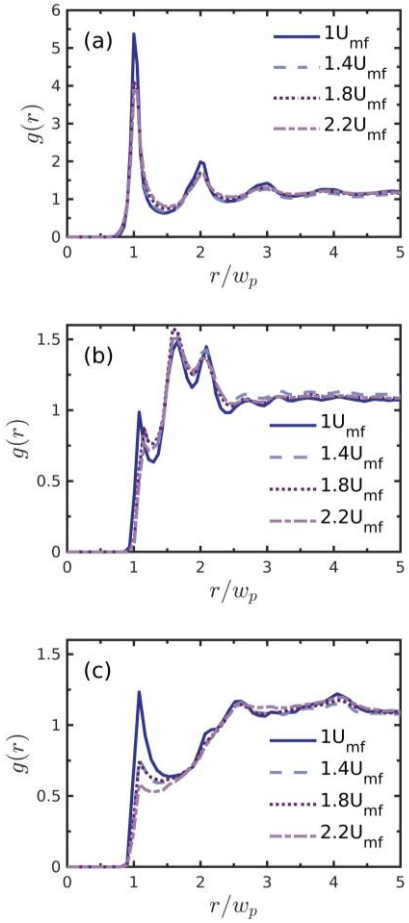

Figure 4.4 Radial distribution functions for (a)AR-1, (b)AR-2 and (c)AR-4 particles with different superficial gas velocity.

4.2.3 Order parameter

In order to study the local ordered structure of particles in the bed, in addition to

the radial distribution analysis based on the particle center distribution, the distribution of particle orientation should also be considered. Here, To accomplish this, we employ nematic-order correlation function and tetratic-order correlation function to study the local ordered structure of rod-like particles in the bed[166,211-213].

4.2.3.1 The local nematic-order correlation function

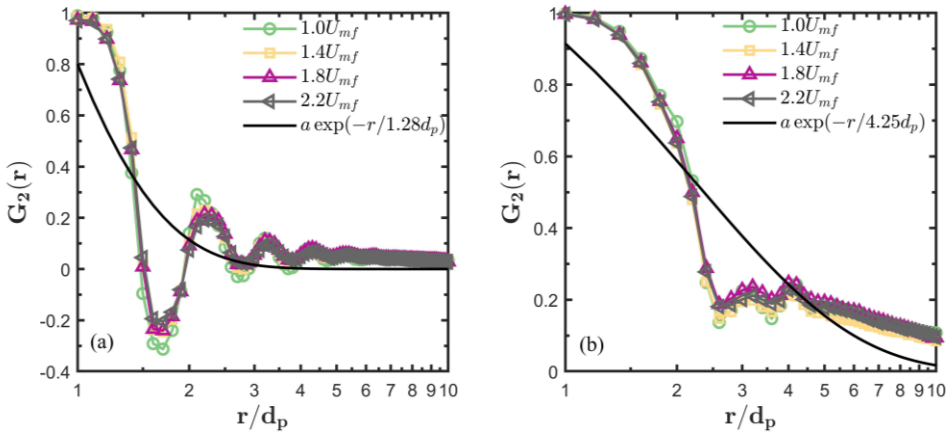

Figure 4.5 The local nematic-order correlation function for (a)AR-2 particles and (b)AR-4 particles with different superficial gas velocity.

Figure 4.5 displays the effect of gas velocity on the nematic correlation function. It shows that the curve rapidly decays to zero, indicating that the orientation correlation is short-range, which may be attributed to the strong particle-fluid interaction and collision between particles. And the gas velocity has little effect on the orientation correlation of the particles. For all gas velocities, the orientation correlation reaches a maximum value at contact around $r/d_p = 1$. Combined with the radial distribution

function, the particles can be aligned along their long sides to maximize the orientation correlation. For AR-2 particles, there are some peaks near $r/d_p = 1$, or 2 which corresponds to the structure of Figure 4.3(a) and (c). And the minimum is obtained near $r/d_p = 1.6$, which corresponds to the structure of Figure 4.3(b). For AR-4 particles, the minimum is obtained near $r/d_p = 2.6$, which corresponds to the structure of Figure 4.3(e). There is also a smaller peak near $r/d_p = 4$ corresponding to Figure 4.3 (f).

In order to further study the effect of aspect ratio on the nematic correlation function, we show the exponential fitting to the local nematic-order correlation function at $2.2U_{mf}$ in Figure 4.5, $G_2(r) \propto ae^{-r/\xi_2}$, where ξ_2 is the order correlation length. With the increase in aspect ratio, the order correlation length gradually increases, where ξ_2 are equal to 1.28 and 4.25, respectively. Forming clusters arranged with long sides is easier for particles with a larger aspect ratio.

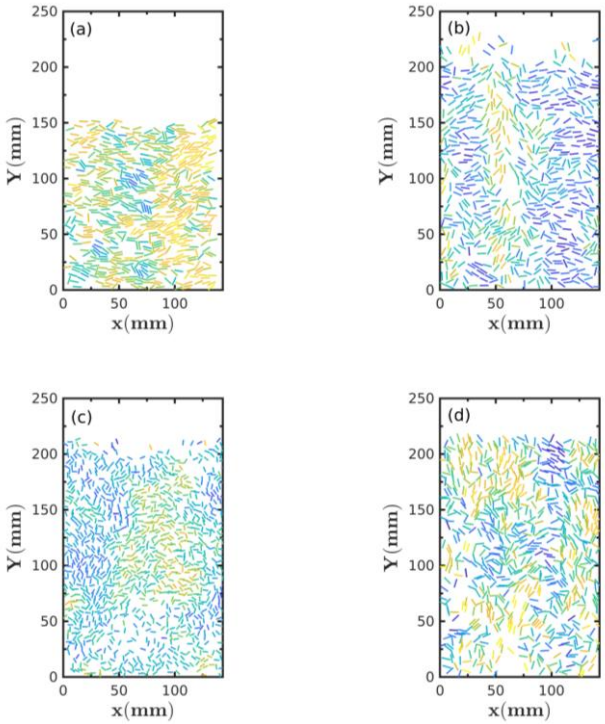

Figure 4.6 Colour maps of the local nematic-order correlation function under various gas velocities (a) Fixed bed; (b)Active channel flow; (c) bubbling bed with AR-2 and (d) bubbling bed with AR-4 particles under $1.4U_{mf}$.

Figure 4.6 shows snapshots of the colour maps of the local nematic-order correlation function of states of (a) fixed bed, (b) active channeling, (c) bubbling bed, and (d) bubbling bed under $1.4U_{mf}$. AR-2 particles are used in subgraph (c) whereas AR-4 in the others. The particle configurations are rather different in these four cases. In the fixed bed, particles tend to be oriented horizontally and $G_2(r)$ of the particles is lower in the central region of the bed. As the gas velocity increases, channeling appears in the center of the bed, where $G_2(r)$ of the particles is large and the particles tend to be vertically oriented. It implies that the interlocking is locally broken as the gas velocity increases, and the fluid follows the channel where flow resistance is low[95].

The gas will promote the vertical orientation of the particles, thereby making $G_2(r)$ of the particles larger. Figure 4.6(c) and (d) depicts the colour map of the nematic correlation field of the bubbling bed of AR-2 and AR-4 particles. It can be seen that there are small clusters for larger values of the nematic correlation, the particles of which are parallel to each other. There are many particles parallel to each other above the bubbles. Compared with AR-2 particles, AR-4 particles have more particles that are parallel to each other, indicating that the larger the aspect ratio, the more serious the interlocking between particles.

4.2.3.2 Tetratic-order correlation function

By analyzing the radial distribution function and the nematic-order parameter G_2, we observe that rod-like particles tend to form perpendicular structures. To provide a more detailed characterization of particle arrangements, this experiment introduces the tetratic-order correlation function G_4 [208,209,211-213,271-273]. It can characterize the arrangement of particles in parallel or perpendicular to each other.

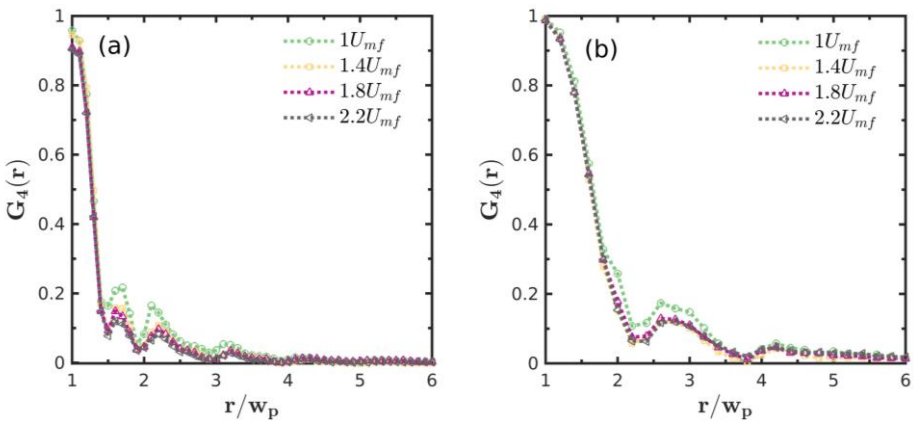

Figure 4.7 The tetratic-order correlation function G_4 for (a) AR-2 particles and (b) AR-4 particles with different superficial gas velocity.

The tetratic-order correlation function of particles with different aspect ratios were obtained by calculation. Figure 4.7 shows the tetratic-order correlation function of AR-2 and AR-4 particles at different superficial gas velocities. In all cases, G_4 clearly shows that the system does not show significant ordering, and the distribution curve shows a series of peaks (parallel or vertical) over a short distance. This behavior is attributed to the local structure of nonspherical particles within the system. The peak value of the curve decreases as the gas velocity increases, indicating an increase in the interaction between particles and between particles and the fluid. This results in the disruption of the local structure within the bed, leading to the formation of a loose structure.

4.3 Dynamics of particle configuration

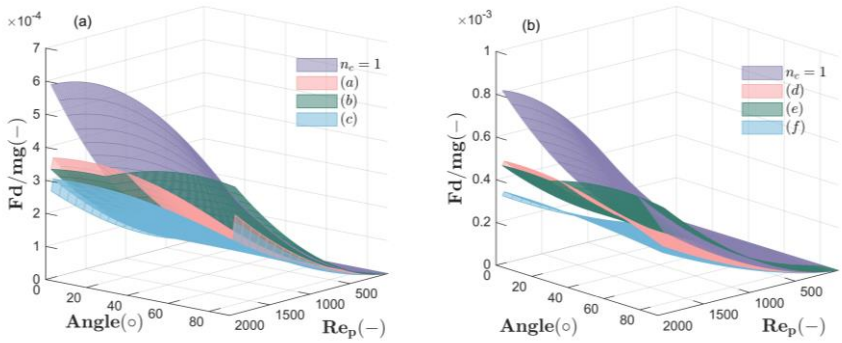

Figure 4.8 Normalized drag of different particle configurations as a function of orientation at different Re for AR-2 particles and AR-4 particles; (a), (b), (c), (d), (e) and (f) represent different particles configuration in Figure 4.3.

To examine the dynamic effects of the particle configuration, we calculate the project area at different angles and then obtain the drag force of the above particle configurations. The drag force F_d is given by[21,228]

$$F_d = \frac{1}{2}\rho_g C_d\left(\frac{\pi}{4}d_v^2\right)(u-\overrightarrow{v_p})|u-v| \tag{4.2}$$

$$C_d = \frac{8}{Re}\frac{1}{\sqrt{\emptyset_{\parallel}}} + \frac{16}{Re}\frac{1}{\sqrt{\emptyset}} + \frac{3}{\sqrt{Re}}\frac{1}{\emptyset^{\frac{3}{4}}} + 0.42 \times 10^{0.4(-\log\emptyset)^{0.2}}\frac{1}{\emptyset_{\perp}} \tag{4.3}$$

Where C_d is the drag efficient, d_v the volume − equivalent diameter, $\vec{u}$ the gas velocity, v the particle velocity, Re the Reynolds number, $\emptyset_{\parallel}$ the lengthwise sphericity, $\emptyset$ the particle sphericity, and $\emptyset_{\perp}$ the crosswise sphericity. The particle mass is assumed to be unity here.

Figure 4.8 compares the scaled drag force of different configurations at various angles and Re number. For the parallel configurations (i.e., a, c, d, f in Figure 4.3), the drag force per unit mass is smaller than that of individual rod-like particles. However, for the perpendicular configurations (i.e., b, e in Figure 4.3), the drag force increases with the angle and could even be larger than that of individual rod-like particles at a large angle side. So it is clear that the configuration significantly affects the drag force, which requires a configuration-dependent drag force for nonspherical particles.

The role of the super-particle is very important in under-resolved simulations (e.g., the two-fluid model[274-277]) of rod-like particles, as the drag force[274] and lift force[24] there in needs the subgrid structural information of collections of particles in each computational cell. For spherical particles, the solids volume fraction and slip velocity are two factors normally adopted to account for the subgrid structure effects. For nonspherical particles, especially for rod-like particles here, we are still far from reaching a consensus regarding the modeling of subgrid particle configurations. The super-particles analysis can be expected to help modelling of fluidization of rod-like particles, though more efforts are definitely needed in future.

4.4 Super-particles

Rod-like particles are easy to lie parallel to each other and form clusters. These

clusters of particles behave collectively as an assembly, which we call super-particles[206,278]. These clusters exhibit relatively high stability and can behave independently in many ways, akin to individual particles. To further quantify the particle configuration, in what follows we perform a statistical analysis of the super-particles. Here, a super-particles is identified when the centroid distance between one particle and its neighbours is less than a given value $(2d_p)$ and their orientation is close to parallel (the intersection angle is less than $5°$), see Figure 4.9.

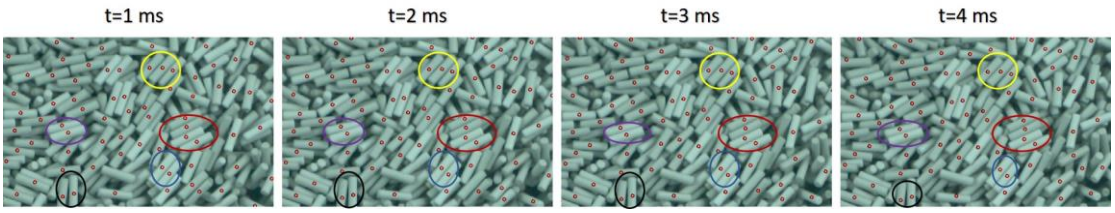

Figure 4.9 Examples of super-particles.

4.4.1 Super-particles size distributions

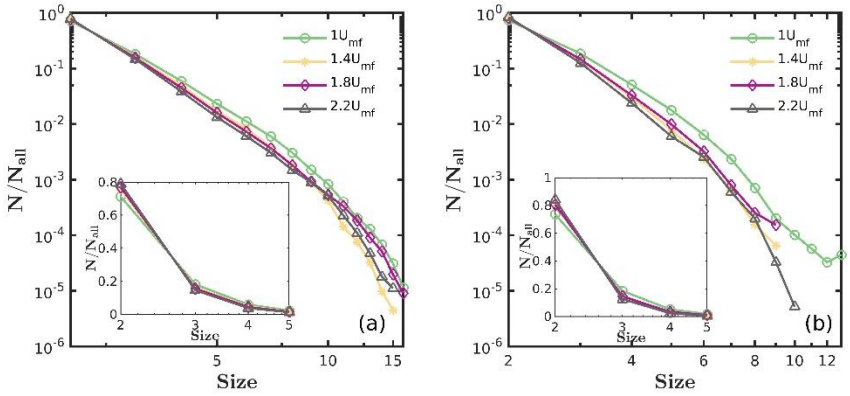

Figure 4.10 Super-particles size distributions for (a)AR-2 and (b)AR-4 particles with

different gas velocities in the double logarithm coordinate. The total number of super-particles normalizes the number of super-particles.

In order to quantitatively study the influence of gas velocity on super-particles, the size distribution of super-particles is analyzed as shown in Figure 4.10, The x-axis represents the size of super-particles, while the y-axis represents the number distribution of super-particles of corresponding size, with the total number of super-particles normalized. It can be seen from the figure that the number of super-particles decreases rapidly with the increase of the size of the super-particles. Super-particles are mainly small-sized clusters, while large-sized super-particles are less. The main reason is that small-sized particles are less disturbed by external fluids and thus stable. Large-sized super-particles are not easy to exist stably for a long time due to external disturbances and frequent collisions of small particles. After continuous crushing and reorganization, a dynamic balance is formed. The superficial gas velocity has little effect on the size of the super-particles. For same particles, as the gas velocity increases, the particles with a super-particles size of 2 gradually increase, while the larger super-particles size decreases. This is due to the increase in collisions between particles and between particles and side walls as gas velocity increases, causing larger super-particles to split into smaller ones.

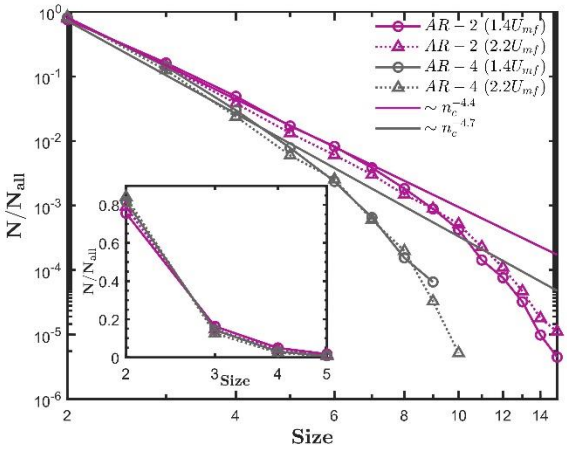

Figure 4.11 Super-particles size distributions for AR-2 and AR-4 particles with different gas velocities in the double logarithm coordinate. The total number of super-particles normalizes the number of super-particles. The black and red solid lines are the power law in a double logarithm coordinate.

Figure 4.11 shows the size distribution of super-particles for AR-2 and AR-4 particles under gas velocities of $1.4U_{mf}$ and $2.2U_{mf}$. The size here refers to the number of rod-like particles in a super-particles. For the sake of comparison, the size distribution is normalized by the total number of super-particles in each case. In all cases, most super-particles are within the size of five particles, and two-particle configuration predominates (as seen in Figure 4.3and Figure 4.5). The size distribution of small super-particles satisfies a power-law relationship, i.e., for AR-2 particles, $n_c(<7)\sim n_c^{-4.4}$ and for AR-4 particles, $n_c(<5)\sim n_c^{-4.7}$, where n_c is the particle number contained in a super-particles. The distribution curve of AR-4 declines faster than that of AR-2, indicating that the longer the aspect ratio, the greater tendency to form smaller super-particles in the bed. Further, the size distribution seems not sensitive

to the variation of gas velocity for each particle type.

4.4.2 The lifetime of super-particles

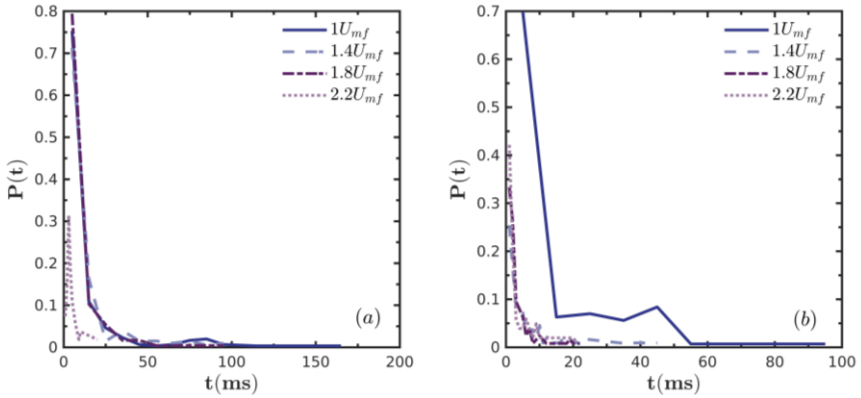

Figure 4.12 The distribution of super-particles lifetime under different gas velocities for (a)AR-2 particles and (b)AR-4 particles.

Another essential characteristic of the particle configuration is the lifetime[279]. Figure 4.12 shows the probability density distribution of the lifetime of these super-particles. The influence of gas velocity on the lifetime distribution of super-particles is apparent from the figure, with a critical point observed for both AR-2 and AR-4 particles. For AR-2 particles, the critical point is between $1.8U_{mf}$-$2.2U_{mf}$. When the gas velocity increases from $1.8U_{mf}$ to $2.2U_{mf}$, the lifetime distribution of super-particles changes significantly. Conversely, for the gas velocity below $1.8U_{mf}$, the change in lifetime distribution is minimal. For AR-4 particles, the critical point is observed between $1U_{mf}$-$1.4U_{mf}$, when the gas velocity increases from $1U_{mf}$ to

$1.4U_{mf}$, the lifetime distribution of super-particles changes obviously. However, for the gas velocity above $1.4U_{mf}$, the change in lifetime distribution is relatively insignificant.

For AR-2 particles, the lifetime is affected by the gas velocity, the higher the gas velocity, the shorter the lifetime. By comparison, AR-4 particles are less affected by the gas velocity. Generally, the lifetime of AR-2 particles is much longer than that of AR-4 particles, suggesting that a smaller aspect ratio increases the mechanical stability of the configuration.

4.4.3 The Super-particles time fraction F_c

The super-particles time fraction refers to the proportion of the total sampling time in which the particles appear in the bed, which reflects the severity of particle agglomeration. The super-particles time fraction of Super-particles F_c[280,281]

$$F_c = \frac{\sum_1^{N_c} t_i}{t_{total}} \tag{4.4}$$

where N_c is the total number of super-particles in the total sampling time t_{total}, t_i is the existence time of super-particles i.

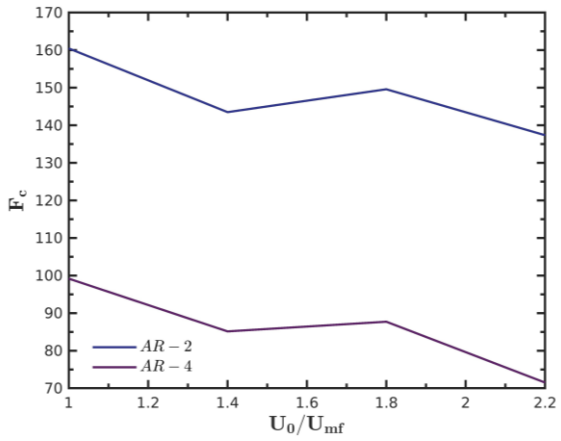

Figure 4.13 Variation of super-particles time fraction F_c under different gas velocities for (a)AR-2 particles and (b)AR-4 particles.

Figure 4.13 display the variation of the super-particles time fraction of AR-2 and AR-4 particles. The effect of superficial gas velocity is the same for AR-2 and AR-4 particles, and the general trend is that F_c of super-particles decreases with an increase in gas velocity. It shows that super-particles are not easy to exist at higher gas velocity. The F_c of AR-2 particles is significantly larger than that of AR-4 particles, indicating that AR-2 super-particles are more prone to existing than AR-4 particles.

4.4.4 The super-particles frequency f_c

The super-particles frequency f_c is the number of super-particles detected per unit

time[280,281],

$$f_c = \frac{k}{t_{total}} \tag{4.5}$$

where k represents the total number of super-particles in the total sampling time t_{total}.

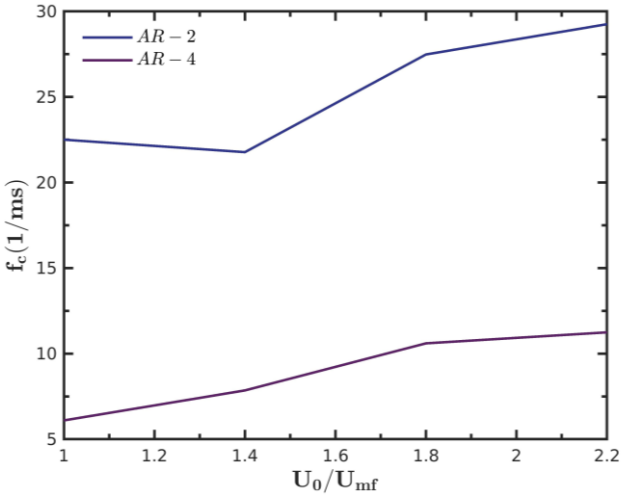

Figure 4.14 The super-particles frequency under different gas velocities for (a)AR-2 particles and (b)AR-4 particles.

Figure 4.14 shows the super-particles frequency of AR-2 and AR-4 particles. For all cases, the frequency of super-particles increases with an increase in gas velocity. Combined with Figure 4.13, at higher gas velocities, super-particles tend to exist in the form of small sizes and have a shorter lifetime. This is due to the strong gas-solid interaction, and the formation and fragmentation of super-particles are more frequent.

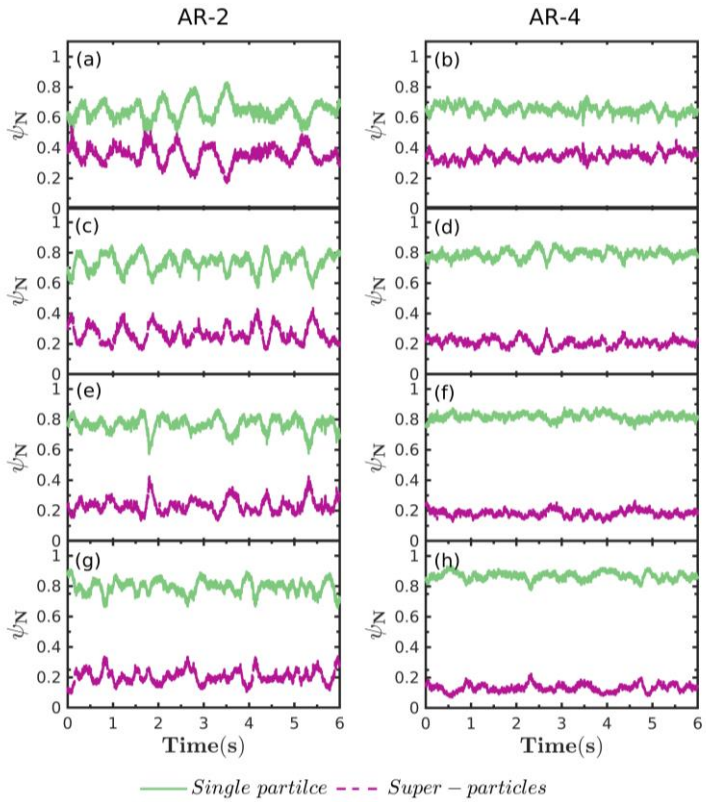

Figure 4.15 The variations of particle number fraction(ψ_N) for AR-2 and AR-4 particles with different gas velocities. (a,b) U_{mf}; (c,d) $1.4U_{mf}$; (e,f) $1.8U_{mf}$; (g,h) $2.2U_{mf}$.

Figure 4.15 shows the proportion of super-particles and single particles at different times for AR-2 and AR-4 particles with different gas velocities. For all cases, the ratio fluctuates around a constant value; As the gas velocity increases, the number of single particles gradually increases, while the number of particles in the super-particles gradually decreases, and the difference between the two gradually increases.

4.4.5 Super-particles velocity

The velocity of super-particles can be defined as follows:

$$v_c(t) = \frac{1}{n_c}\sum_{i=1}^{n_c} v_{ci}\,(t) \tag{4.6}$$

where n_c represents the total number of particles in a super-particles, v_{ci} denotes the velocity of single particle i.

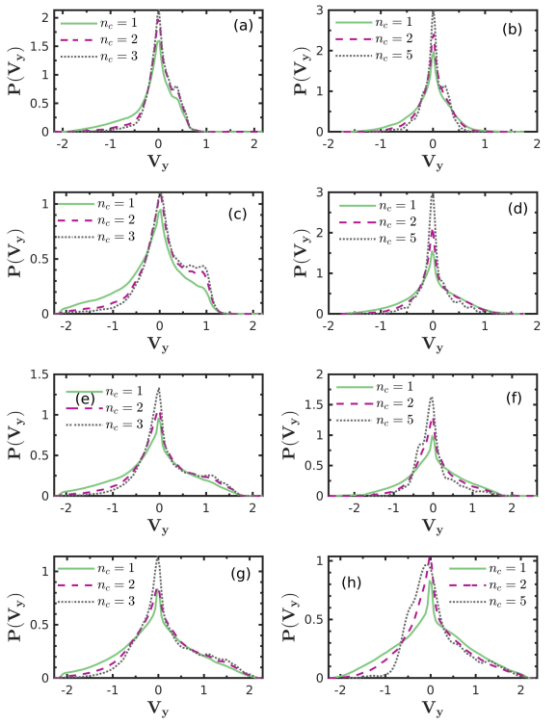

Figure 4.16 Probability density distribution of translational velocity under different gas velocity for AR-2 and AR-4 particles. (a,b) U_{mf}; (c,d) $1.4U_{mf}$; (e,f) $1.8U_{mf}$; (g,h) $2.2U_{mf}$.

According to the particles configuration obtained from Figure 4.3, in what follows, we put special efforts on analyzing the super-particles with $n_c = 2$ and 3 for AR-2 particles, and $n_c = 2$ and 5 for AR-4 particles. Figure 4.16 shows the velocity distributions of these super-particles for AR-2 and AR-4 particles under different gas velocities. At $V_y > 0$ there are no significant differences between super-particles of

different sizes for both AR-2 and AR-4. However, at $V_y < 0$, the disparity between different sized super-particles grows wider. That is to say, in the particle rising stage in the fluidized bed, there is no big difference in the velocity of different particle configurations, but in the particle falling stage, the larger super-particles fall slower.

4.5 Summary

In this chapter, we investigated the configuration and dynamics of nonspherical particles with various aspect ratios and gas velocities using experimental measurements. Major results are as follows:

(1) By analyzing the coordination number, it becomes apparent that the larger the aspect ratio, the larger the exclusion volume, and the greater the possibility of contact with other particles. This highlights the significant impact that particle shape has on the heat transfer behavior of the fluidized bed.

(2) Three ordered structures belonging to two configurations (two particles parallel or perpendicular to each other) are identified by combining the radial distribution function and order parameter analysis. We explain this ordering phenomenon through entropy. Interestingly, rod-like particles tend to align within a distance of one particle length. As the superficial gas velocity and aspect ratio increase, with no preference for

a specific configuration, eventually forming a disordered structure. The interlocking between particles significantly affects fluid flow within the bed.

(3) Comparing the scaled drag force of different configurations at various angles and Re number, we found that different particle configurations have a significant impact on drag force, with an enormous difference in drag force between different particle configurations. Therefore, it is crucial to consider the influence of different particle configurations when evaluating drag force.

(4) The dynamics of the particle configuration are studied, including size distribution, lifetime, time fraction, frequency and the velocity distribution.

i. The size distribution of the super-particles satisfies the power law at a small size regime. A striking difference between negative vertical velocity is found for three ordered structures. The particle configurations behave differently in the upward and downward cycles. Their lifetime is affected by the aspect ratio.

ii. Analysis of time fraction and frequency reveals that AR-2 super-particles are more likely to occur than AR-4 particles. Additionally, at higher gas velocities, super-particles tend to have smaller sizes and shorter lifetime.

5 The Flow Characteristics of Bubbles

5.1 Introduction

Bubble generation is a crucial feature in the operation of bubbling fluidized beds. As a typical meso-scale structure, bubbles contain a large amount of dynamic characteristic information related to particle motion, which is not only affected by the interaction between particles, but also a critical factor to the heat/mass transfer process[75,282-284]. While research on the formation, development, and movement of bubbles in fluidized beds with spherical particles is well-established, the study of bubble characteristics of nonspherical particles in fluidized beds is still limited.

In this chapter, we will conduct a study on the motion behavior and mechanism of bubbles in fluidization of rod-like particles. We analyze the effects of fluidization gas velocity and particle shape on various bubble characteristics such as bubble volume, bubble velocity, bubble aspect ratio, and particle motion around the bubble.

5.2 Bubble characterization and analysis

The main objective of studying bubbles is to first detect their presence. In our experiment, Voronoi analysis is used to obtain the local concentration of particles in the bed at a certain instant[285-287], and then coarse-grained treatment is used to obtain the

distribution space of instantaneous solid phase concentration in the bed, enabling the characterization and analysis of bubbles in the bubbling bed.

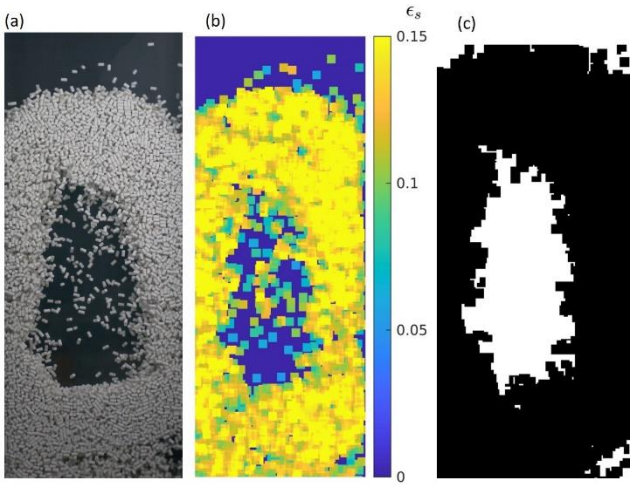

Figure 5.1 Image processing for determination of bubbles: (a)raw image; (b) solid concentration distributions; (c) bubble distributions obtained from figure (a) and (b).

The process of bubble determination in the bubbling bed is illustrated in Figure 5.1. with (a) showing the original image, while (b) displaying the corresponding spatial distribution of solid phase concentration, and (c) representing the binary image corresponding to (a) and (b). The area, centroid coordinates, and aspect ratio of the bubble are then obtained by further processing.

The bubble volume (V_B) is determined by multiplying the bubble area (A_B) by the bubble thickness, which is assumed to be the same as the bed thickness (25mm) in the calculation.

Tracking the centroid position of the bubble in successive frames is a common method to determine the bubble rising velocity in fluidized bed experiments. The centroid position is the center of mass of the binary image corresponding to the bubble. By comparing the centroid positions of the bubble in several successive frames with a time interval of Δt, the bubble velocity can be calculated as the displacement of the centroid position divided by the time interval. In this study, the time interval is $\Delta t = 0.02s$, and 6000 frames are analyzed for each video. The bubble rising velocity is tracked on average for 200-300 frames[288-290].

$$V_b = \frac{\sqrt{(x_i - x_{i-1})^2 + (y_i - y_{i-1})^2}}{\Delta t} \tag{5.1}$$

where $(x_i,\ y_i)$ and $(x_{i-1},\ y_{i-1})$ are the coordinates of the subsequent positions of the bubble, Δt is the time interval between pictures.

The aspect ratio (χ_b) of the bubble is used to characterize the shape information of the bubble, which is defined as[291],

$$\chi_b = \frac{y_{max}}{x_{max}} \tag{5.2}$$

where y_{max} and x_{max} are vertical and horizontal lengths of the bubble, as shown in Fig. 5.2.

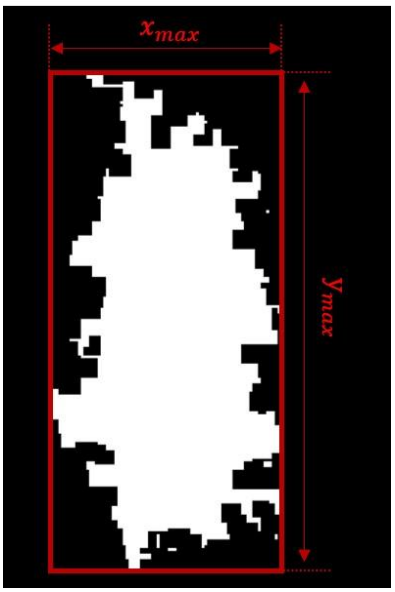

Figure 5.2 Example of bubble aspect ratio.

5.3 Effect of superficial gas velocity

5.3.1 Bubble volume

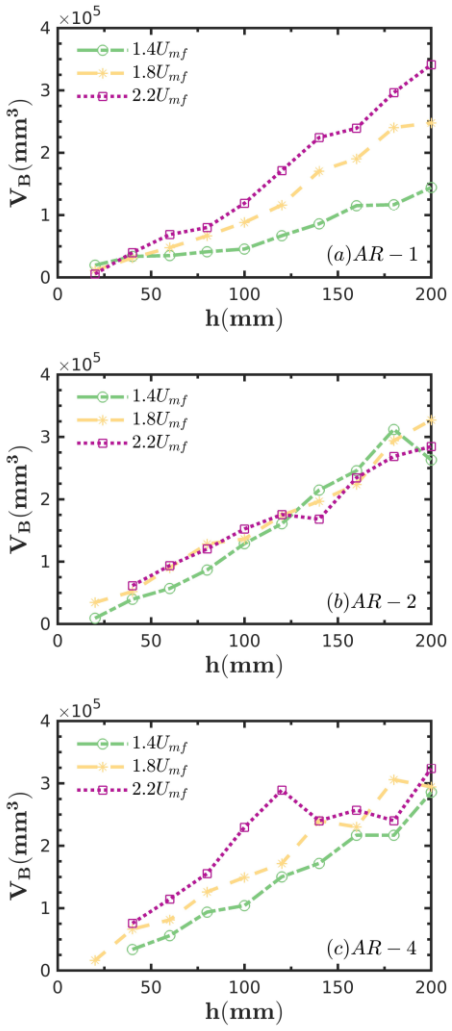

Figure 5.3 Bubble volume V_B as a function of distance above the gas distribution under different gas velocity for (a)AR-1 particles, (b)AR-2 particles and (c)AR-4 particles.

Bubble size is an important factor affecting reactor performance[292]. Therefore, we investigated the impact of gas velocity on bubble volume V_B. As shown in Figure 5.3, V_B increases with axial height due to continuous bubble coalescence throughout the bed. Additionally, V_B is positively correlated with gas velocity. Due to the rise in superficial gas velocity, the amount of gas passing through the bed per unit time increases, while there is a limitation to the increase of gas velocity between emulsion

phases, resulting in a higher amount of gas passing through the bed with the bubble phase, so V_B increases with an increase in gas velocity. Increasing gas velocity also reduces the distance between bubbles, promoting higher bubble contact and coalescence rates.

Compared to the observations in Figure 5.3(a, b, c), it is evident that rod-like particles exhibit a less pronounced sensitivity to the increase in superficial gas velocity. This may be because cylindrical particles are more likely to lead to channels with lower resistance, thus causing the gas to pass through and resulting in decreased gas content of the bubble phase. Hence, the change in V_B with superficial gas velocity is not as prominent as that observed for spherical particles. As the height of the bed increases, the volume of bubbles gradually increases, implying that the size of bubbles grows as they rise due to bubble growth and condensation. However, the curve exhibits fluctuations at higher bed heights, indicating that, in the middle and lower part of the bed, bubbles primarily grow and coalesce, leading to a gradual increase in bubble size. Conversely, in the upper section of the bed, the change in bubble volume with gas velocity becomes more intricate due to the breakup and condensation of bubbles.

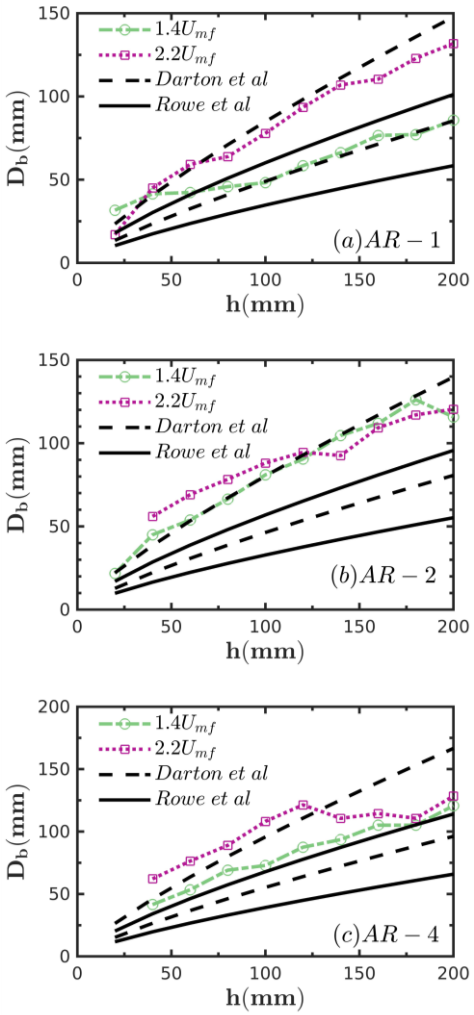

Figure 5.4 Bubble diameter along the height above the distributor for different particle shape, the block lines representing different correlations.

Fig.15 presents a comparison of the experimental data with two popular literature correlations, in which the Darton model[293] expression is

$$D_b = \left(u - U_{mf}\right)^{0.4}(H + H_d)^{0.8}\mathrm{g}^{-1/5} \tag{5.3}$$

u represents the gas velocity, while U_{mf} refers to the minimum fluidization velocity. H denotes the bed height, H_d is the distribut plate parameter (which is set

to 0 for the sintered version of this experiment), and g represents the acceleration due to gravity. The Rowe model[294] expression is

$$D_b = \left(u - U_{mf}\right)^{0.4}(H + H_d)^{0.75}\mathrm{g}^{-0.25} \tag{5.4}$$

The comparison in Figure 5.4 shows that the Darton model provides better predictions for spherical particles, whereas the Rome model consistently underestimates the experimental values. For rod-like particles, the Rome model also underestimates the experimental results, while the Darton model performs well at higher gas velocities but slightly underestimates the experimental values at lower gas velocities. However, at a gas velocity of $2.2U_{mf}$ and higher bed heights, the predicted results of the Darton model are larger than the experimental data. The probable reason is that the model is limited to considering the bubble growth pattern resulting from the coalescence of bubbles but without considering any mechanism related to bubble splitting and breakage.

5.3.2 Bubble shape parameters

The shape characteristics of bubbles are essential parameters that strongly influence the fluidization behavior and the efficiency of heat and mass transfer between the gas and solid phases. The aspect ratio, as an important factor, provides information on the approximate shape of the bubble. According to the definition of aspect ratio in

section 5.2 , bubbles that are vertically stretched will have an aspect ratio greater than 1, while those that are horizontally stretched will have an aspect ratio less than 1[224,290,295,296].

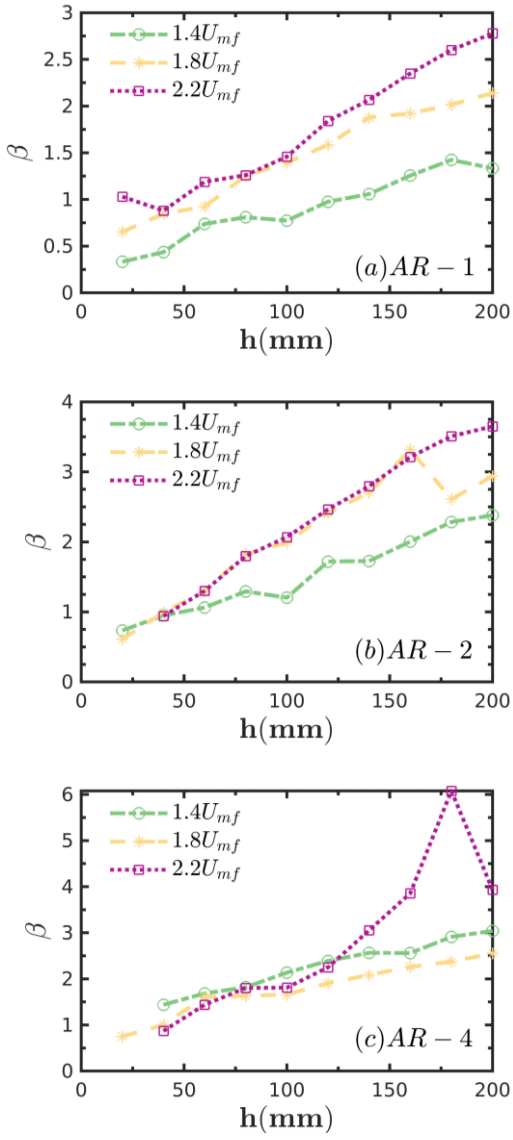

Figure 5.5 Bubble aspect ratio χ_b as a function of distance above the gas distribution under different gas velocity for (a)AR-1 particles, (b)AR-2 particles and (c)AR-4 particles.

Studying the variation of bubble aspect ratio under different gas velocities can

provide insights into how changes in flow conditions affect the shape of the bubbles. Figure 5.5 illustrates bubble aspect ratio χ_b under different gas velocities for AR-1 particles, AR-2 particles and AR-4 particles. The figure shows that the aspect ratio of bubbles for all particle shapes increases with increasing gas velocity. At lower velocities, the bubble shape is nearly spherical, but as the gas velocity increases, the shape becomes more elongated. The bubble aspect ratio is small, and bubble stretches horizontally at the bottom of the bed. As bed height increases, the bubble aspect ratio also increases, leading the bubble to transition from a flat shape to an elongated shape. This is because as the bed height increases, the bubble volume gradually expands (as shown in Figure 5.3), but due to the limitation of the bed width. To balance the volume expansion resulting from gas velocity or bubble coalescence, the bubble can only expand longitudinally. This discovery is consistent with the outcomes reported in previous literature. This discovery is consistent with the results reported in the literature[297,298].

5.4 Effect of particle shape

5.4.1 Bubble volume

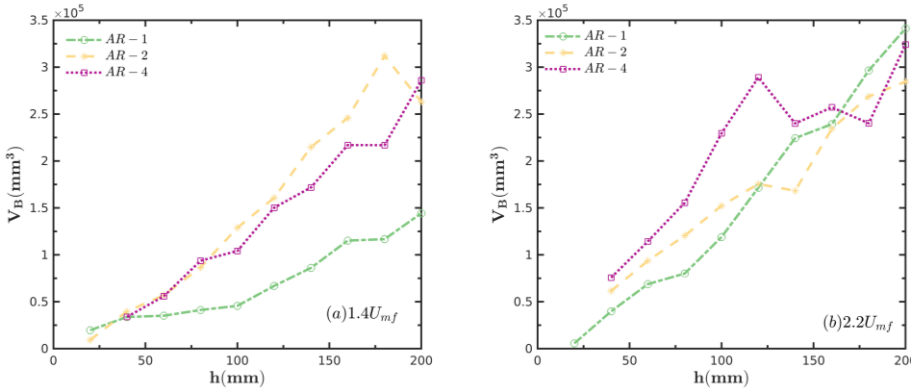

Figure 5.6 Bubble volume V_B as a function of distance above the gas distribution under different particle shape for (a)$1.4U_{mf}$, (b) $2.2U_{mf}$.

Figure 5.6 illustrates the variation in bubble volume (V_B) with respect to particle shape. As depicted in Figure 5.6(a), when the gas velocity is $1.4U_{mf}$, V_B of AR-2 particles is greater than that of AR-4 particles, indicating that the particles with smaller aspect ratio have a lesser inhibitory effect on bubbles, resulting in a larger bubble volume at low gas velocities. As gas velocity increases, the difference in V_B between rod-like particles decreases, indicating that the influence of particle shape on the production and development of bubbles becomes smaller when the gas velocity is higher. Compared to rod-like particles, AR-1 particles have the smallest bubble volume, indicating that rod-like particles are more conducive to bubble production and development. It is likely that bubbles develop better in cases with a smaller aspect ratio, which can be attributed to the influence of minimum fluidization velocity. This study yielded similar results to those reported in literature[227], where a lower minimum

fluidization velocity leads to a larger bubble volume and less gas leakage[222]. According to Figure 3.2, AR-2 has the smallest U_{mf} and the largest bubble volume.

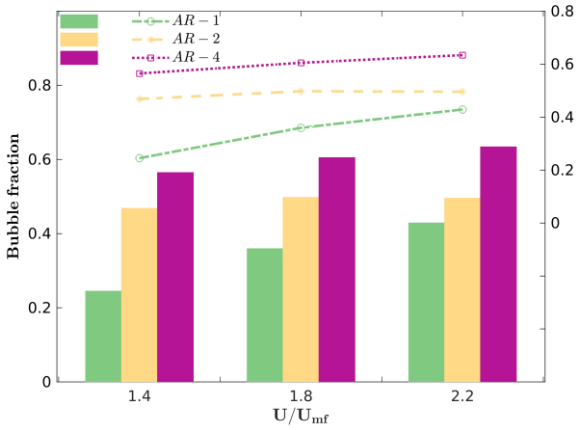

Figure 5.7 The bubble fraction distribution under different fluidization gas velocities for AR-1, AR-2, and AR-4 particles.

Figure 5.7 shows the bubble fraction distribution of the three types of particles. The bubble fraction is determined by calculating the ratio of the bubble area to the total instantaneous bed area, which is the combined area occupied by the bubbles and solids during the fluidization process. As shown in the figure, the bubble fraction increases gradually as gas velocity or aspect ratio increases.

5.4.2 Bubble velocity

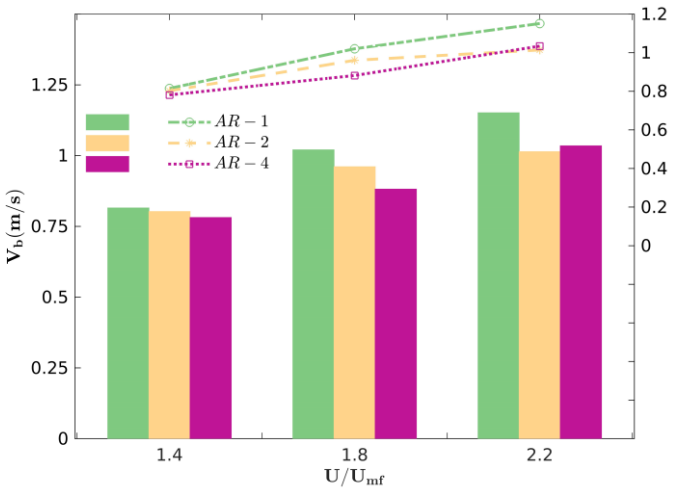

Figure 5.8 Bubble vertical velocity distribution under different fluidization gas velocities for AR-1, AR-2, and AR-4 particles.

Figure 5.8 depicts the relationship between bubble velocity and superficial gas velocity for AR-1, AR-2, and AR-4 particles. It is evident from the figure that as the gas velocity increases, the bubble velocity also increases gradually. As explained earlier, an increase in gas velocity generates more bubbles with larger size, which experience greater buoyancy, leading to an increase in bubble velocity. This results in more frequent interactions between bubbles and faster coalescence, resulting in a higher bubble velocity. However, as the aspect ratio increases, the bubble velocity decreases. It is evident from Figure 5.6 that the bubble volume of spherical particles is the smallest under the same conditions. Combining this observation with the earlier analysis, it can be inferred that larger bubbles experience greater velocity. However, Figure 5.8 indicates that the bubble velocity decreases as the shape of the particles deviates from the sphere, and the bubble velocity of AR-1 particles is the largest. Therefore, we

speculate that for rod-like particles, several particle configurations exist inside the bed, and the bubbles need to overcome the interlocking between the particles and allow them to rotate in the preferred direction, thereby consuming a portion of the energy and reducing the bubble velocity. The above analysis emphasizes the significant influence of particle shape on the rise of bubbles within the bed.

5.4.3 Bubble shape parameter

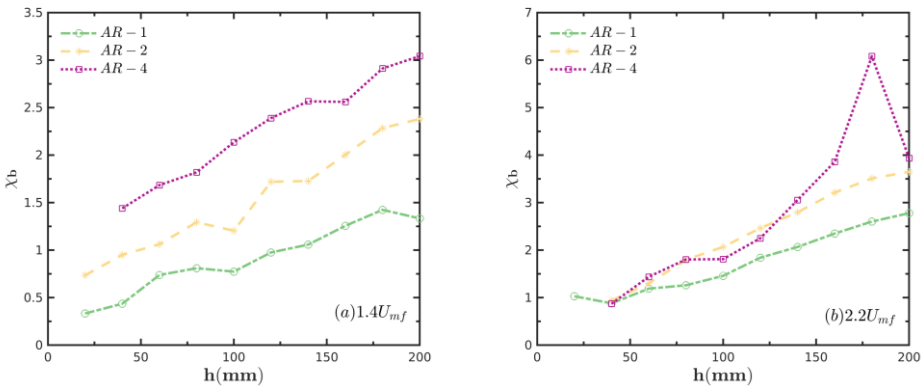

Figure 5.9 Effects of the particle shape on the aspect ratio of bubble under different fluidization gas velocities.

Figure 5.9 illustrates the effect of particle shape on the aspect ratio of the bubbles. As depicted in the figure, as the aspect ratio of the particles increases, so does the aspect ratio of the bubbles, and the bubble shape becomes more elongated as the particle shape deviates from a sphere. However, the impact of particle shape on bubble shape is reduced with the increase of the gas velocity. In most regions of the bed, the bubbles of

AR-1 particles are more spherical. This phenomenon could be attributed to the particle arrangement within the rod-like particles, which creates greater resistance for bubbles to move. To overcome this resistance, the bubbles tend to stretch vertically along the bed, leading to a more elongated shape.

5.5 Particle motion around bubbles

As previously discussed, the dynamics of bubbles are significantly influenced by particle shape. In this section, the qualitative analysis of the movement state of the particles around the bubbles in the bubbling bed is carried out, and the movement laws of the particles at different positions are studied.

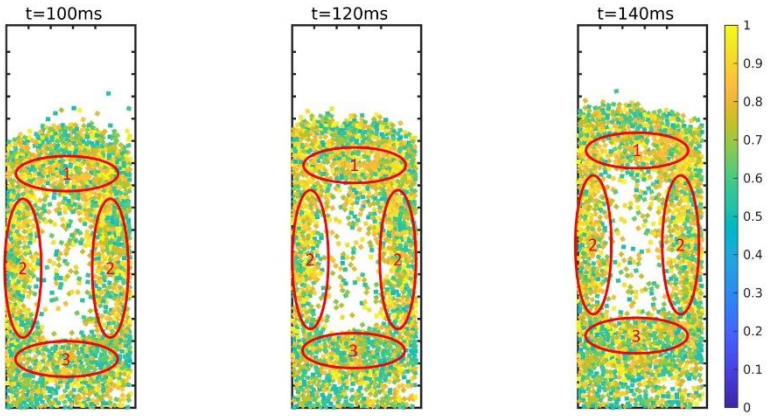

Figure 5.10 Spatial distributions of particle orientations at $1.4U_{mf}$ for AR-2 particles.

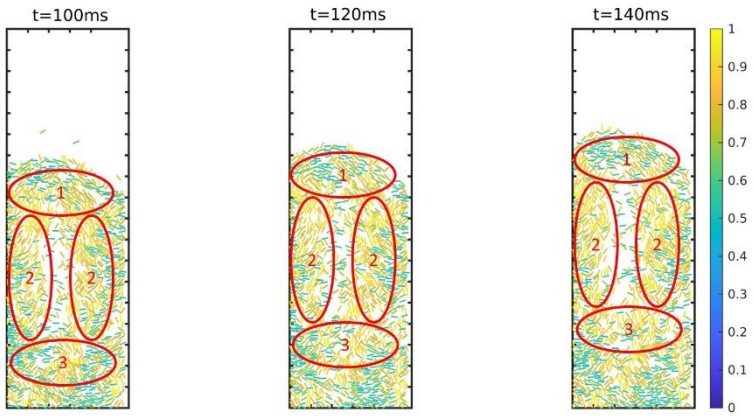

Figure 5.11 Spatial distributions of particle orientations at $1.4U_{mf}$ for AR-4 particles.

Figure 5.10-Figure 5.11 illustrates the spatial distribution of particle orientation at three consecutive moments. The value 1 denotes vertical orientation of particles, i.e., parallel to the direction of fluid flow, while 0 represents horizontal orientation of particles, i.e., direction perpendicular to the fluid flow. The depicted time period corresponds to the process of bubble rising. It can be observed that the orientation of particles around the bubble undergoes continuous changes as the bubble rises, and the particles tend to be positioned side by side or overlapping with each other. In the case of AR-2 and AR-4 particles, most of the particles on either side of the bubble are vertically oriented, while the particles above the bubble are horizontally oriented.

In order to investigate the correlation between particle orientation and bubble characteristics in more detail, the bubble is divided into three sections, referred to as Part1, Part2, and Part3, as illustrated in Figure 5.10-Figure 5.11. Here, the particles are all around the bubbles.

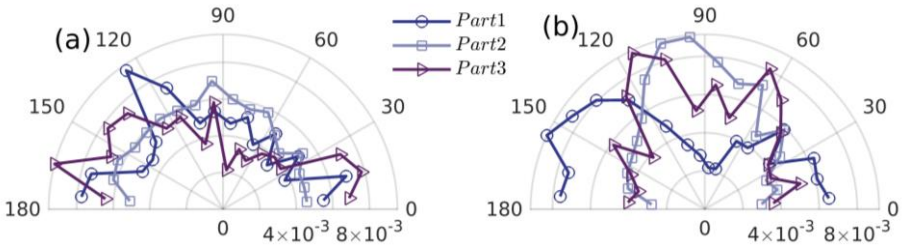

Figure 5.12 particle orientation of different positions for (a)AR-2 and (b)AR-4 particles at $1.4U_{mf}$.

The analysis reveals that the rod-like particles located in Part1 tend to orient horizontally with a peak angle between 120-180°, whereas those in Part2 are inclined towards the vertical direction with a peak angle of approximately 90°. However, the impact of particle shape on gas-solid fluidization characteristics is more pronounced for AR-4 particles. This is because the strong solid shear force due to collision during the rapid falling of particles makes them tend to be arranged vertically, and the boundary effect further promotes this vertical arrangement. These findings indicate that, in bubbling beds, particle shape has a significant impact on gas-solid fluidization characteristics, with rod-like particles favoring horizontal orientation above the bubble and vertical orientation on both sides, which highlights the importance of considering particle shape in designing and optimizing fluidized bed processes. The analysis of orientation distribution provides further support to the observations presented in Figure 5.11. However, for Part3, the orientation distribution differs between AR-2 and AR-4

particles, with AR-2 particles tending to be horizontally aligned and AR-4 particles vertically aligned. This indicates that particle orientation begins to change under the influence of particle-particle and particle-fluid interaction forces as the bubble moves and rises through the bed. The bubble first breaks the particle configuration between rod particles, forcing them to align strongly with the flow direction. As the bubble rises, the horizontally oriented particles experience greater fluid dynamics and rotate to a position with lower fluid resistance, while the bubble exerts an axial shear force on the particles, forcing them to align with the flow direction. This is because particles in the vertical direction have a lower projection area perpendicular to the direction of fluid flow compared to the other directions.

5.6 Summary

In this chapter, we used image processing technology to extract static and dynamic bubble characteristic parameters of particles with different aspect ratios. We investigated the effects of superficial gas velocity and particle shape on bubble volume, motion velocity, and bubble shape parameters. The main findings and conclusions are summarized below:

(1) The results showed that the bubble volume (V_B) increases with the bubble location (h), and V_B is positively correlated with the apparent velocity. Additionally,

under the same conditions, the V_B of rod particles was found to be larger than that of spherical particles. At any position in the bed, the bubble formed by spherical particles was found to be more round compared to rod-like particles, and the aspect ratio of the bubble increases with the increase of gas velocity.

(2) The bubble velocity V_b increases gradually with the increase of superficial gas velocity, while it is negatively correlated with the aspect ratio. Specifically, the bubble velocity decreases with the increase of the aspect ratio. Compared to spherical particles, rod-like particles have lower bubble velocities due to the need for bubbles to overcome the interlocking between particles and allow them to rotate in their preferred direction.

(3) Particle orientation analysis revealed that when particles are located above the bubble, they tend to be oriented perpendicular to the airflow direction, whereas on both sides of the bubble, particles tend to be oriented parallel to the airflow direction.

6 Conclusions and Further Studies

6.1 Conclusions

The current work investigates the hydrodynamic characteristics of nonspherical particles by using rod-like particles as the research object. The following are the main conclusions of this paper:

(1) Particles with a larger aspect ratio, such as AR-4 particles, have a tendency to form channeling flows, whereas particles with a smaller aspect ratio smoothly transit to a bubbling regime. The aspect ratio also affects the minimum fluidization velocity and bed expansion rate, which exhibits a first decrease and then increase as the aspect ratio increases. Furthermore, the shape of particles plays a crucial role in determining their movement behavior: Decreasing aspect ratios lead to the formation of regular internal circulations; Velocity distributions of the particle velocity, especially the rotational component, deviate from Maxwellian velocity distribution, and high-velocity-tail are observed. The joint probability density function of V_r and V_y are asymmetric. V_r is positively associated with V_y. The translational energy is almost 2 orders higher than rotational； Particles tend to be horizontally oriented at lower gas velocity. With increasing gas velocity, the vertical orientation becomes more dominant. For AR-2 particles, the horizontally oriented particles dominate, while for AR- 4 particles,

vertically oriented grains predominate.

(2) Three ordered structures belonging to two configurations (two particles parallel or perpendicular to each other) are identified by combining the radial distribution function and the local nematic order parameter analysis. We explain this ordering phenomenon through entropy. By analyzing the configuration dynamics of particles, it becomes evident that particle configurations behave differently in the upward and downward cycles. Their lifetime is affected by the aspect ratio. The size distribution of the super-particles satisfies the power law at a small size regime. A striking difference between negative vertical velocity is found for three ordered structures. The coordination number generally increases with the aspect ratio. We also compare the scaled drag force of different configurations at various angles and Re numbers. there is an enormous difference in drag force between different particle configurations, suggesting further research is needed on constructing a configuration-dependent drag force.

(3) On the meso-scale, the influence of particle shape and superficial gas velocity on bubble shape and motion is discussed, and the mechanism of rod-like particles on bubbles is revealed. In all cases, the volume of bubbles (V_B) increases proportionately with the height of the bubbles (h_B) and shows a positive correlation with superficial gas velocity. Rod-like particles were found to have a larger bubble volume compared to

spherical particles, but the bubbles formed by spherical particles are more circular in shape. Additionally, for rod-like particles, an interlocking structure inside the bed resulted in directional particles and a negative correlation between V_b and aspect ratio. Analyzing the motion of particles around the bubble revealed that the rising bubble must break the interlocking between particles and promote their rotation towards their preferred direction, thereby requiring a certain amount of energy consumption that ultimately reduces the velocity of the bubble.

In summary, the aspect ratio and superficial gas velocity of rod particles have an important influence on the fluidity of particles. These findings are expected to improve the understanding of the hydrodynamic characteristics of nonspherical particles and have guiding significance for the fluidization of nonspherical particles. In the design and optimization of fluidized bed reactor, the above factors need to be considered comprehensively to achieve the purpose of improving efficiency, reducing energy consumption, and optimizing performance.

6.2 Original contributions

The novel aspects of this study are as follows:

(1) A systematic study was conducted to investigate the flow behavior of rod-like particles in a bubbling bed, which provided insights into the fluidization characteristics

of nonspherical particles. The study revealed how rod-like particles' behavior varied with particle shape and operating conditions.

(2) This paper quantifies the particle interlocking phenomenon using parameters such as radial distribution function and order parameter. The study identified three ordered structures in the bed and found that these configurations have an impact on bubble dynamics. By analyzing bubble dynamics, the study revealed how these structures affect the behavior of bubbles in the system.

6.3 Future work

According to the research content of this paper, the future research work mainly includes the following aspects:

(1) This study obtained a comprehensive understanding of the gas-solid flow process of rod-like particles, and the mechanism behind these laws was elaborated. However, these laws are predominantly qualitative. In the next step, the study will focus on quantitatively analyzing these laws and establishing correlations among the key parameters to enhance the understanding of particle behavior in gas-solid flow processes.

(2) This experimental study selected one shape of the particles, the next step can choose a variety of shapes of particles for experimental research; In this experiment,

the research regime is limited to bubbling bed, and other regimes are not involved. Experimental research on other regimes can be carried out to improve the experimental work and deepen the understanding of nonspherical particle fluidization.

(3) Biomass and combustible solid waste are mostly co-fluidized with fluidized media in a fluidized bed in the form of nonspherical particles. Therefore, the next step should be based on the experiment in this paper, adding fluidized media to study the co-fluidization process of multi-component particles.

References

[1] GAO X, YU J, LU L, LI C, ROGERS W A. Development and validation of SuperDEM-CFD coupled model for simulating non-spherical particles hydrodynamics in fluidized beds[J]. Chemical Engineering Journal, 2020, 420: 127654.

[2] ZHONG W, YU A, LIU X, TONG Z, ZHANG H. DEM/CFD-DEM modelling of non-spherical particulate systems: theoretical developments and applications[J]. Powder Technology, 2016, 302: 108-152.

[3] GUPTA C K, SATHIYAMOORTHY D. Fluid Bed Technology in Materials Processing[M]. first. the United States: CRC press, 1998.

[4] DEWETTINCK K, HUYGHEBAERT A. Fluidized bed coating in food technology[J]. Trends in Food Science & Technology, 1999, 10(4-5): 163-168.

[5] ZIYANI L, FATAH N. Use of experimental designs to optimize fluidized bed granulation of maltodextrin[J]. Advanced Powder Technology, 2014, 25(3): 1069-1075.

[6] ZHANG J, JIANG X, PIAO G, YANG H, ZHONG Z. Simulation of a fluidized bed electrode direct carbon fuel cell[J]. International Journal of Hydrogen Energy, 2015, 40(8): 3321-3331.

[7] CUI T, HOU Y, FENG H, WU S, LI W, LI Z. Granulation process analysis technologies and potential applications in traditional Chinese medicine[J]. Acupuncture and Herbal Medicine, 2022, 2(1): 9-24.

[8] ZHU R, CHEN Y, WANG W. Particle tracking velocimetry study of the nonequilibrium characteristics of a fluidized bed[J]. AIChE Journal, 2023, : e18043.

[9] WANG H, CHEN Y, WANG W. Particle-level dynamics of clusters: Experiments in a gas-fluidized bed[J]. AIChE Journal, 2021, 68(3): e17525.

[10] ANICIC B, LU B, LIN W, WU H, DAM-JOHANSEN K, WANG W. CFD simulation of mixing and segregation of binary solid mixtures in a dense fluidized bed[J]. The Canadian Journal of Chemical Engineering, 2019, 98(1): 412-420.

[11] DEEN N G, VAN SINT ANNALAND M, VAN DER HOEF M A, KUIPERS J A M. Review of discrete particle modeling of fluidized beds[J]. Chemical Engineering Science, 2007, 62(1-2): 28-44.

[12] GOLDSCHMIDT M J V, LINK J M, MELLEMA S, KUIPERS J A M. Digital image analysis measurements of bed expansion and segregation dynamics in

dense gas-fluidised beds[J]. Powder Technology, 2003, 138(2-3): 135-159.

[13] DE JONG J F, ODU S O, VAN BUIJTENEN M S, DEEN N G, VAN SINT ANNALAND M, KUIPERS J A M. Development and validation of a novel Digital Image Analysis method for fluidized bed Particle Image Velocimetry[J]. Powder Technology, 2012, 230: 193-202.

[14] REZAEI H, LIM C J, LAU A, SOKHANSANJ S. Size, shape and flow characterization of ground wood chip and ground wood pellet particles[J]. Powder Technology, 2016, 301: 737-746.

[15] HALLETT W L H, WIENS E, BUSIGIN M K, BERDUSCO D, SKIFFINGTON R. Packed bed combustion of binary mixtures of wood particles of different shapes and sizes[J]. Fuel, 2022, 328: 125289.

[16] CHUNG Y-C, YEH C-H, LIAO C-C. Experimental investigation into the wet non-spherical granular segregation and mixing in rotating drums[J]. Powder Technology, 2022, 409: 117844.

[17] CHEN L M, LIN Q, ZHU Z Z. Simulation and Analysis of Attitude of Non-Spherical Particles in Drum Granulation[J]. Advanced Materials Research, 2014, 889-890: 170-173.

[18] WAKEFIELD J P, LATTANZI A M, PECHA M B, CIESIELSKI P N, CAPECELATRO J. Fast estimation of reaction rates in spherical and non-spherical porous catalysts[J]. Chemical Engineering Journal, 2023, 454: 139637.

[19] ZHANG Y, JIN B, ZHONG W. Experimental investigation on mixing and segregation behavior of biomass particle in fluidized bed[J]. Chemical Engineering and Processing: Process Intensification, 2009, 48(3): 745-754.

[20] CHEN W-H, LIN B-J, LIN Y-Y, CHU Y-S, UBANDO A T, SHOW P L, ONG H C, CHANG J-S, HO S-H, CULABA A B, PéTRISSANS A, PéTRISSANS M. Progress in biomass torrefaction: principles, applications and challenges[J]. Progress in Energy and Combustion Science, 2021, 82: 100887.

[21] HöLZER A, SOMMERFELD M. New simple correlation formula for the drag coefficient of non-spherical particles[J]. Powder Technology, 2008, 184(3): 361-365.

[22] SANJEEVI S K P, KUIPERS J A M, PADDING J T. Drag, lift and torque correlations for non-spherical particles from Stokes limit to high Reynolds numbers[J]. International Journal of Multiphase Flow, 2018, 106: 325-337.

[23] JIANG Y, GUO Y, YU Z, HUA X, LIN J, WASSGREN C R, CURTIS J S. Discrete element method–computational fluid dynamics analyses of flexible fibre fluidization[J]. Journal of Fluid Mechanics, 2021, 910: A8.

[24] MAHAJAN V V, PADDING J T, NIJSSEN T M J, BUIST K A, KUIPERS J A M. Nonspherical particles in a pseudo-2D fluidized bed: Experimental study[J].

AIChE Journal, 2018, 64(5): 1573-1590.

[25] MEMA I, BUIST K A, KUIPERS J A M, PADDING J T. Fluidization of spherical versus elongated particles: Experimental investigation using magnetic particle tracking[J]. AIChE Journal, 2019, 66(4): e16895.

[26] MA H, ZHAO Y. Investigating the fluidization of disk-like particles in a fluidized bed using CFD-DEM simulation[J]. Advanced Powder Technology, 2018, 29(10): 2380-2393.

[27] LU G, THIRD J R, MüLLER C R. Discrete element models for non-spherical particle systems: From theoretical developments to applications[J]. Chemical Engineering Science, 2015, 127: 425-465.

[28] ZHU H P, ZHOU Z Y, YANG R Y, YU A B. Discrete particle simulation of particulate systems: Theoretical developments[J]. Chemical Engineering Science, 2007, 62(13): 3378-3396.

[29] ZHU H P, ZHOU Z Y, YANG R Y, YU A B. Discrete particle simulation of particulate systems: A review of major applications and findings[J]. Chemical Engineering Science, 2008, 63(23): 5728-5770.

[30] FULLMER W D, HRENYA C M. The clustering instability in rapid granular and gas-solid flows[J]. Annual Review of Fluid Mechanics, 2017, 49(1): 485-510.

[31] GAO X, YU J, LU L, LI C, ROGERS W A. Development and validation of SuperDEM-CFD coupled model for simulating non-spherical particles hydrodynamics in fluidized beds[J]. Chemical Engineering Journal, 2021, 420: 127654.

[32] SHAO Y, ZHONG W, CHEN X, CHEN Y, JIN B. Spouting of non-spherical particles in conical-cylindrical spouted bed[J]. The Canadian Journal of Chemical Engineering, 2014, 92(4): 742-746.

[33] FREIREICH B, KUMAR R, KETTERHAGEN W, SU K, WASSGREN C, ZEITLER J A. Comparisons of intra-tablet coating variability using DEM simulations, asymptotic limit models, and experiments[J]. Chemical Engineering Science, 2015, 131: 197-212.

[34] FREIREICH B, KETTERHAGEN W R, WASSGREN C. Intra-tablet coating variability for several pharmaceutical tablet shapes[J]. Chemical Engineering Science, 2011, 66(12): 2535-2544.

[35] GAO X, YU J, LI C, PANDAY R, XU Y, LI T, ASHFAQ H, HUGHES B, ROGERS W A. Comprehensive experimental investigation on biomass-glass beads binary fluidization: A data set for CFD model validation[J]. AIChE Journal, 2019, 66(2): e16843.

[36] GELDART D. Types of gas fluidization[J]. Powder Technology, 1973, 7(5):

285-292.

[37] CROWE C T. Multiphase Flow Handbook[M]. first. Boca Raton: CRC press, 2005.

[38] RüDISüLI M, SCHILDHAUER T J, BIOLLAZ S M A, VAN OMMEN J R. Scale-up of bubbling fluidized bed reactors — A review[J]. Powder Technology, 2012, 217: 21-38.

[39] YANG W-C. Handbook of Fluidization and Fluid-particle Systems[M]. first. New York : CRC press, 2003.

[40] CARDOSO J, SILVA V, EUSéBIO D, BRITO P, TARELHO L. Improved numerical approaches to predict hydrodynamics in a pilot-scale bubbling fluidized bed biomass reactor: A numerical study with experimental validation[J]. Energy Conversion and Management, 2018, 156: 53-67.

[41] HEIDENREICH S, FOSCOLO P U. New concepts in biomass gasification[J]. Progress in Energy and Combustion Science, 2015, 46: 72-95.

[42] COUTO N, SILVA V B, BISPO C, ROUBOA A. From laboratorial to pilot fluidized bed reactors: Analysis of the scale-up phenomenon[J]. Energy Conversion and Management, 2016, 119: 177-186.

[43] WANG S, SHEN Y. CFD-DEM study of biomass gasification in a fluidized bed reactor: Effects of key operating parameters[J]. Renewable Energy, 2020, 159: 1146-1164.

[44] KONG D, WANG S, LUO K, HU C, LI D, FAN J. Three-dimensional simulation of biomass gasification in a full-loop pilot-scale dual fluidized bed with complex geometric structure[J]. Renewable Energy, 2020, 157: 466-481.

[45] RADMANESH R, CHAOUKI J, GUY C. Biomass gasification in a bubbling fluidized bed reactor: Experiments and modeling[J]. AIChE Journal, 2006, 52(12): 4258-4272.

[46] MOTTA I L, MIRANDA N T, MACIEL FILHO R, WOLF MACIEL M R. Biomass gasification in fluidized beds: A review of biomass moisture content and operating pressure effects[J]. Renewable and Sustainable Energy Reviews, 2018, 94: 998-1023.

[47] RAVELLI S, PERDICHIZZI A, BARIGOZZI G. Description, applications and numerical modelling of bubbling fluidized bed combustion in waste-to-energy plants[J]. Progress in Energy and Combustion Science, 2008, 34(2): 224-253.

[48] RAMOS A, MONTEIRO E, SILVA V, ROUBOA A. Co-gasification and recent developments on waste-to-energy conversion: A review[J]. Renewable and Sustainable Energy Reviews, 2018, 81: 380-398.

[49] LUPA C J, RICKETTS L J, SWEETMAN A, HERBERT B M. The use of commercial and industrial waste in energy recovery systems - A UK preliminary

study[J]. Waste Manag, 2011, 31(8): 1759-1764.

[50] KONG D, LUO K, WANG S, YU J, FAN J. Particle behaviours of biomass gasification in a bubbling fluidized bed[J]. Chemical Engineering Journal, 2022, 428: 131847.

[51] TOKMURZIN D, NAM J Y, PARK S J, YOON S J, MUN T-Y, YOON S M, MOON J H, LEE J G, LEE D H, RA H W, SEO M W. Three-Dimensional CFD simulation of waste plastic (SRF) gasification in a bubbling fluidized bed with detailed kinetic chemical model[J]. Energy Conversion and Management, 2022, 267: 115925

[52] MA H, ZHOU L, LIU Z, CHEN M, XIA X, ZHAO Y. A review of recent development for the CFD-DEM investigations of non-spherical particles[J]. Powder Technology, 2022, 412: 117972.

[53] RILEY N A. Projection sphericity[J]. Journal of Sedimentary Research, 1941, 11(2): 94-95.

[54] CRUZ-MATíAS I, AYALA D, HILLER D, GUTSCH S, ZACHARIAS M, ESTRADé S, PEIRó F. Sphericity and roundness computation for particles using the extreme vertices model[J]. Journal of Computational Science, 2019, 30: 28-40.

[55] ZHAO B, WANG J. 3D quantitative shape analysis on form, roundness, and compactness with μCT[J]. Powder Technology, 2016, 291: 262-275.

[56] WADELL H. Volume, shape, and roundness of quartz particles[J]. The Journal of Geology, 1935, 43(3): 250-280.

[57] LOTH E. Drag of non-spherical solid particles of regular and irregular shape[J]. Powder Technology, 2008, 182(3): 342-353.

[58] ERIKSSON M, ALDERBORN G, NYSTRöM C, PODCZECK F, NEWTON J M. Comparison between and evaluation of some methods for the assessment of the sphericity of pellets[J]. International Journal of Pharmaceutics, 1997, 148(2): 149-154.

[59] BOUWMAN A M, BOSMA J C, VONK P, WESSELINGH J A, FRIJLINK H W. Which shape factor(s) best describe granules?[J]. Powder Technology, 2004, 146(1-2): 66-72.

[60] LIU B, ZHANG X, WANG L, HONG H. Fluidization of non-spherical particles: Sphericity, Zingg factor and other fluidization parameters[J]. Particuology, 2008, 6(2): 125-129.

[61] HEYWOOD H. Uniform and non-uniform motion of particles in fluids[C]. Proceedings of the Symposium on Interactions Between Fluids and Particles, 1962 : 1-8.

[62] WADELL H. The coefficient of resistance as a function of Reynolds number for solids of various shapes[J]. Journal of the Franklin Institute, 1934, 217(4): 459-490.

[63] BUIST K A, VAN DER GAAG A C, DEEN N G, KUIPERS J A M. Improved magnetic particle tracking technique in dense gas fluidized beds[J]. AIChE Journal, 2014, 60(9): 3133-3142.

[64] GUíO-PéREZ D C, PRöLL T, HOFBAUER H. Solids residence time distribution in the secondary reactor of a dual circulating fluidized bed system[J]. Chemical Engineering Science, 2013, 104: 269-284.

[65] HOOMANS B P B, KUIPERS J A M, MOHD SALLEH M A, STEIN M, SEVILLE J P K. Experimental validation of granular dynamics simulations of gas-fluidised beds with homogenous in-flow conditions using Positron Emission Particle Tracking[J]. Powder Technology, 2001, 116(2-3): 166-177.

[66] WINDOWS-YULE C R K, SEVILLE J P K, INGRAM A, PARKER D J. Positron emission particle tracking of granular flows[J]. Annual review of chemical and biomolecular engineering, 2020, 11: 367-396.

[67] DEPYPERE F, PIETERS J G, DEWETTINCK K. PEPT visualisation of particle motion in a tapered fluidised bed coater[J]. Journal of Food Engineering, 2009, 93(3): 324-336.

[68] MOSTOUFI N, CHAOUKI J. Local solid mixing in gas–solid fluidized beds[J]. Powder Technology, 2001, 114(1-3): 23-31.

[69] MOSTOUFI N, CHAOUKI J. Flow structure of the solids in gas–solid fluidized beds[J]. Chemical Engineering Science, 2004, 59(20): 4217-4227.

[70] TRIBEDI T, PILLAJETTI P, KUMARI R, PANT H J, TIWARI P, UPADHYAY R K. Measurements of solid velocity in a pilot-scale Geldart's group B circulating fluidized bed using a radioactive particle tracking technique[J]. Industrial & Engineering Chemistry Research, 2022, 61(25): 9110-9121.

[71] WANG H, CHEN Y, WANG W. Scale-dependent nonequilibrium features in a bubbling fluidized bed[J]. AIChE Journal, 2018, 64(7): 2364-2378.

[72] BRüCKER C. Study of vortex breakdown by particle tracking velocimetry (PTV)[J]. Experiments in Fluids, 1993, 14(1-2): 133-139.

[73] CARLOS VARAS A E, PETERS E A J F, KUIPERS J A M. Experimental study of full field riser hydrodynamics by PIV/DIA coupling[J]. Powder Technology, 2017, 313: 402-416.

[74] ELSINGA G E, SCARANO F, WIENEKE B, VAN OUDHEUSDEN B W. Tomographic particle image velocimetry[J]. Experiments in Fluids, 2006, 41(6): 933-947.

[75] LAVERMAN J A, ROGHAIR I, ANNALAND M V S, KUIPERS H.

Investigation into the hydrodynamics of gas–solid fluidized beds using particle image velocimetry coupled with digital image analysis[J]. The Canadian Journal of Chemical Engineering, 2008, 86(3): 523-535.

[76] CHEN X, ZHONG W, HEINDEL T J. Orientation of cylindrical particles in a fluidized bed based on stereo X-ray particle tracking velocimetry (XPTV)[J]. Chemical Engineering Science, 2019, 203: 104-112.

[77] MEMA I, WAGNER E C, VAN OMMEN J R, PADDING J T. Fluidization of spherical versus elongated particles - experimental investigation using X-ray tomography[J]. Chemical Engineering Journal, 2020, 397: 125203.

[78] CAI J, LI Q, YUAN Z. Orientation of cylindrical particles in gas–solid circulating fluidized bed[J]. Particuology, 2012, 10(1): 89-96.

[79] BOER L, BUIST K A, DEEN N G, PADDING J T, KUIPERS J A M. Experimental study on orientation and de-mixing phenomena of elongated particles in gas-fluidized beds[J]. Powder Technology, 2018, 329: 332-344.

[80] CUNDALL P A, STRACK O D L. A discrete numerical model for granular assemblies[J]. Géotechnique, 1979, 29(1): 47-65.

[81] TSUJI Y, KAWAGUCHI T, TANAKA T. Discrete particle simulation of two-dimensional fluidized bed[J]. Powder Technology, 1993, 77(1): 79-87.

[82] XU B H, YU A B. Numerical simulation of the gas-solid flow in a fluidized bed by combining discrete particle method with computational fluid dynamics[J]. Chemical Engineering Science, 1997, 52(16): 2785-2809.

[83] VU-QUOC L, ZHANG X, WALTON O R. A 3-D discrete-element method for dry granular flows of ellipsoidal particles[J]. Computer Methods in Applied Mechanics and Engineering, 2000, 187(3-4): 483-528.

[84] FRAIGE F Y, LANGSTON P A, CHEN G Z. Distinct element modelling of cubic particle packing and flow[J]. Powder Technology, 2008, 186(3): 224-240.

[85] FAVIER J F, ABBASPOUR-FARD M H, KREMMER M, RAJI A O. Shape representation of axi-symmetrical, non-spherical particles in discrete element simulation using multi-element model particles[J]. Engineering Computations, 1999, 16(4): 467-480.

[86] ABBASPOUR-FARD M H. Theoretical validation of a multi-sphere, discrete element model suitable for biomaterials handling simulation[J]. Biosystems Engineering, 2004, 88(2): 153-161.

[87] KRUGGEL-EMDEN H, ELSKAMP F. Modeling of Screening Processes with the Discrete Element Method Involving Non-Spherical Particles[J]. Chemical Engineering & Technology, 2014, 37(5): 847-856.

[88] LIU X, GAN J, ZHONG W, YU A. Particle shape effects on dynamic behaviors in a spouted bed: CFD-DEM study[J]. Powder Technology, 2020, 361: 349-362.

[89] GUO Y, WASSGREN C, KETTERHAGEN W, HANCOCK B, CURTIS J. Some computational considerations associated with discrete element modeling of cylindrical particles[J]. Powder Technology, 2012, 228: 193-198.

[90] GOVENDER N, WILKE D N, KOK S, ELS R. Development of a convex polyhedral discrete element simulation framework for NVIDIA Kepler based GPUs[J]. Journal of Computational and Applied Mathematics, 2014, 270: 386-400.

[91] G. NEZAMI E, M. A. HASHASH Y, ZHAO D, GHABOUSSI J. Shortest link method for contact detection in discrete element method[J]. International Journal for Numerical and Analytical Methods in Geomechanics, 2006, 30(8): 783-801.

[92] ZHONG W, JIN B, ZHANG Y, WANG X, XIAO R. Fluidization of biomass particles in a gas−solid fluidized bed[J]. Energy & Fuels, 2008, 22(6): 4170-4176.

[93] ZHAO Y, XIAO H, UMBANHOWAR P B, LUEPTOW R M. Simulation and modeling of segregating rods in quasi-2D bounded heap flow[J]. AIChE Journal, 2018, 64(5): 1550-1563.

[94] LU G, THIRD J R, MüLLER C R. Critical assessment of two approaches for evaluating contacts between super-quadric shaped particles in DEM simulations[J]. Chemical Engineering Science, 2012, 78: 226-235.

[95] KRUGGEL-EMDEN H, VOLLMARI K. Flow-regime transitions in fluidized beds of non-spherical particles[J]. Particuology, 2016, 29: 1-15.

[96] ZHOU Z Y, PINSON D, ZOU R P, YU A B. Discrete particle simulation of gas fluidization of ellipsoidal particles[J]. Chemical Engineering Science, 2011, 66(23): 6128-6145.

[97] NAN W, WANG Y, WANG J. Numerical analysis on the fluidization dynamics of rodlike particles[J]. Advanced Powder Technology, 2016, 27(5): 2265-2276.

[98] GAN J, ZHOU Z, YU A. CFD-DEM modeling of gas fluidization of fine ellipsoidal particles[J]. AIChE Journal, 2016, 62(1): 62-77.

[99] MEMA I, BUIST K A, KUIPERS J A M, PADDING J T. Fluidization of spherical versus elongated particles: Experimental investigation using magnetic particle tracking[J]. AIChE Journal, 2019, 66(4): e16895.

[100] HILTON J E, CLEARY P W. The influence of particle shape on flow modes in pneumatic conveying[J]. Chemical Engineering Science, 2011, 66(3): 231-240.

[101] ZHONG W Q, ZHANG Y, JIN B S, ZHANG M Y. Discrete element method simulation of cylinder-shaped particle flow in a gas-solid fluidized bed[J]. Chemical Engineering & Technology, 2009, 32(3): 386-391.

[102] VOLLMARI K, OSCHMANN T, WIRTZ S, KRUGGEL-EMDEN H. Pressure

drop investigations in packings of arbitrary shaped particles[J]. Powder Technology, 2015, 271: 109-124.

[103] GAN J, ZHOU Z, ZOU R, YU A. Discrete element modeling of gas fluidization of fine ellipsoidal particles[C]. AIP Conference Proceedings, 2013 : 1130-1133.

[104] ZHOU Z-Y, ZOU R-P, PINSON D, YU A-B. Dynamic simulation of the packing of ellipsoidal Particles[J]. Industrial & Engineering Chemistry Research, 2011, 50(16): 9787-9798.

[105] MA H, XU L, ZHAO Y. CFD-DEM simulation of fluidization of rod-like particles in a fluidized bed[J]. Powder Technology, 2017, 314: 355-366.

[106] MAHAJAN V V, NIJSSEN T M J, KUIPERS J A M, PADDING J T. Non-spherical particles in a pseudo-2D fluidised bed: Modelling study[J]. Chemical Engineering Science, 2018, 192: 1105-1123.

[107] VOLLMARI K, JASEVIČIUS R, KRUGGEL-EMDEN H. Experimental and numerical study of fluidization and pressure drop of spherical and non-spherical particles in a model scale fluidized bed[J]. Powder Technology, 2016, 291: 506-521.

[108] LIU L X, LITSTER J D. The effect of particle shape on the spouting properties of non-spherical particles[J]. Powder Technology, 1991, 66(1): 59-67.

[109] ABDULLAH M Z, HUSAIN Z, YIN PONG S L. Analysis of cold flow fluidization test results for various biomass fuels[J]. Biomass and Bioenergy, 2003, 24(6): 487-494.

[110] CUI H, GRACE J R. Fluidization of biomass particles: A review of experimental multiphase flow aspects[J]. Chemical Engineering Science, 2007, 62(1-2): 45-55.

[111] SI C, GUO Q. Fluidization Characteristics of Binary Mixtures of Biomass and Quartz Sand in an Acoustic Fluidized Bed[J]. Industrial & Engineering Chemistry Research, 2008, 47(23): 9773-9782.

[112] ESCUDERO D, HEINDEL T J. Bed height and material density effects on fluidized bed hydrodynamics[J]. Chemical Engineering Science, 2011, 66(16): 3648-3655.

[113] PAUDEL B, FENG Z-G. Prediction of minimum fluidization velocity for binary mixtures of biomass and inert particles[J]. Powder Technology, 2013, 237: 134-140.

[114] SHAO Y, REN B, JIN B, ZHONG W, HU H, CHEN X, SHA C. Experimental flow behaviors of irregular particles with silica sand in solid waste fluidized bed[J]. Powder Technology, 2013, 234: 67-75.

[115] R. RAO T, RAM. BHEEMARASETTI J V. Minimum fluidization velocities of mixtures of biomass and sands[J]. Energy, 2001, 26(6): 633-644.

[116] OLIVEIRA T J P, CARDOSO C R, ATAíDE C H. Bubbling fluidization of biomass and sand binary mixtures: Minimum fluidization velocity and particle segregation[J]. Chemical Engineering and Processing: Process Intensification, 2013, 72: 113-121.

[117] KAGE H, AGARI M, OGURA H, MATSUNO Y. Frequency analysis of pressure fluctuation in fluidized bed plenum and its confidence limit for detection of various modes of fluidization[J]. Advanced Powder Technology, 2000, 11(4): 459-475.

[118] JAIBOON O-A, CHALERMSINSUWAN B, MEKASUT L, PIUMSOMBOON P. Effect of flow pattern on power spectral density of pressure fluctuation in various fluidization regimes[J]. Powder Technology, 2013, 233: 215-226.

[119] KODAM M, BHARADWAJ R, CURTIS J, HANCOCK B, WASSGREN C. Cylindrical object contact detection for use in discrete element method simulations. Part I-Contact detection algorithms[J]. Chemical Engineering Science, 2010, 65(22): 5852-5862.

[120] KODAM M, BHARADWAJ R, CURTIS J, HANCOCK B, WASSGREN C. Cylindrical object contact detection for use in discrete element method simulations, Part II-Experimental validation[J]. Chemical Engineering Science, 2010, 65(22): 5863-5871.

[121] S P E. Effect of particle shape on free settling rates of isometric particles[J]. Chemical Engineering Progress, 1948, 44: 157-172.

[122] HAIDER A, LEVENSPIEL O. Drag coefficient and terminal velocity of spherical and nonspherical particles[J]. Powder Technology, 1989, 58(1): 63-70.

[123] MARCHILDON E K, CLAMEN A, GAUVIN W H. Drag and oscillatory motion of freely falling cylindrical particles[J]. The Canadian Journal of Chemical Engineering, 1964, 42(4): 178-182.

[124] HUNER B, HUSSEY R G. Cylinder drag at low Reynolds number[J]. Physics of Fluids, 1977, 20(8): 1211-1218.

[125] UI T J, HUSSEY R G, ROGER R P. Stokes drag on a cylinder in axial motion[J]. Physics of Fluids, 1984, 27(4): 787-795.

[126] UNNIKRISHNAN A, CHHABRA R P. An experimental study of motion of cylinders in newtonian fluids: Wall effects and drag coefficient[J]. The Canadian Journal of Chemical Engineering, 1991, 69(3): 729-735.

[127] PHAN-THIEN N, DOU H-S. Viscoelastic flow past a cylinder: drag coefficient[J]. Computer Methods in Applied Mechanics and Engineering, 1999, 180(3-4): 243-266.

[128] CHHABRA R P, RAMI K, UHLHERR P H T. Drag on cylinders in shear thinning viscoelastic liquids[J]. Chemical Engineering Science, 2001, 56(6):

2221-2227.

[129] GABITTO J, TSOURIS C. Drag coefficient and settling velocity for particles of cylindrical shape[J]. Powder Technology, 2008, 183(2): 314-322.

[130] JOSSIC L, MAGNIN A. Drag of an isolated cylinder and interactions between two cylinders in yield stress fluids[J]. Journal of Non-Newtonian Fluid Mechanics, 2009, 164(1-3): 9-16.

[131] REN B, ZHONG W, JIN B, LU Y, CHEN X, XIAO R. Study on the drag of a cylinder-shaped particle in steady upward gas flow[J]. Industrial & Engineering Chemistry Research, 2011, 50(12): 7593-7600.

[132] SQUIRES W. The Sedimentation of Thin Discs[D]. Doctoral Thesis, Massachusetts Institute of Technology, Department of Chemical Engineering, 1936.

[133] WILLMARTH W W, HAWK N E, HARVEY R L. Steady and unsteady motions and wakes of freely falling disks[J]. Physics of Fluids, 1964, 7(2): 197-208.

[134] SHAIL R, NORTON D J. On the slow broadside motion of a thin disc along the axis of a fluid-filled circular duct[J]. Mathematical Proceedings of the Cambridge Philosophical Society, 2008, 65(3): 793-802.

[135] DAVIS P. Application of optical chaos to temporal pattern search in a nonlinear optical resonator[J]. Japanese Journal of Applied Physics, 1990, 29(7A): L1238.

[136] RAJITHA P, CHHABRA R P, SABIRI N E, COMITI J. Drag on non-spherical particles in power law non-Newtonian media[J]. International Journal of Mineral Processing, 2006, 78(2): 110-121.

[137] MADHAV G V, CHHABRA R P. Drag on non-spherical particles in viscous fluids[J]. International Journal of Mineral Processing, 1995, 43(1-2): 15-29.

[138] AGARWAL N, CHHABRA R P. Settling velocity of cubes in Newtonian and power law liquids[J]. Powder Technology, 2007, 178(1): 17-21.

[139] LASKOVSKI D, STEVENSON P, GALVIN K P. Lift and drag forces on an isolated cubic particle in pipe flow[J]. Chemical Engineering Research and Design, 2009, 87(12): 1573-1581.

[140] CHEN Y, THIRD J R, MüLLER C R. A drag force correlation for approximately cubic particles constructed from identical spheres[J]. Chemical Engineering Science, 2015, 123: 146-154.

[141] WANG J, QI H, YOU C. Experimental study of sedimentation characteristics of spheroidal particles[J]. Particuology, 2009, 7(4): 264-268.

[142] JAYAWEERA K O L F, MASON B J. The behaviour of freely falling cylinders and cones in a viscous fluid[J]. Journal of Fluid Mechanics, 2006, 22(04): 709-720.

[143] ROGER R P. Stokes drag on a flat annular ring[J]. Physics of Fluids, 1982, 25(6):

915-922.

[144] THOMPSON T L, CLARK N N. A holistic approach to particle drag prediction[J]. Powder Technology, 1991, 67(1): 57-66.

[145] CHIEN S-F. Settling velocity of irregularly shaped particles[J]. SPE Drilling & Completion, 1994, 9(04): 281-289.

[146] GANSER G H. A rational approach to drag prediction of spherical and nonspherical particles[J]. Powder Technology, 1993, 77(2): 143-152.

[147] HARTMAN M, TRNKA O, SVOBODA K, VESELý V. Influence of particle shape on the drag coefficient for isometric particles[J]. Collection of Czechoslovak Chemical Communications, 1994, 59(12): 2583-2594.

[148] MADHAV G V, CHHABRA R P. Settling velocities of non-spherical particles in non-Newtonian polymer solutions[J]. Powder Technology, 1994, 78(1): 77-83.

[149] LEITH D. Drag on nonspherical objects[J]. Aerosol Science and Technology, 1987, 6(2): 153-161.

[150] SWAMEE P K, OJHA C S P. Drag coefficient and fall velocity of nonspherical particles[J]. Journal of Hydraulic Engineering, 1991, 117(5): 660-667.

[151] TRAN-CONG S, GAY M, MICHAELIDES E E. Drag coefficients of irregularly shaped particles[J]. Powder Technology, 2004, 139(1): 21-32.

[152] DIOGUARDI F, MELE D. A new shape dependent drag correlation formula for non-spherical rough particles. Experiments and results[J]. Powder Technology, 2015, 277: 222-230.

[153] ZASTAWNY M, MALLOUPPAS G, ZHAO F, VAN WACHEM B. Derivation of drag and lift force and torque coefficients for non-spherical particles in flows[J]. International Journal of Multiphase Flow, 2012, 39: 227-239.

[154] MANDø M, ROSENDAHL L. On the motion of non-spherical particles at high Reynolds number[J]. Powder Technology, 2010, 202(1-3): 1-13.

[155] MEMA I, MAHAJAN V V, FITZGERALD B W, PADDING J T. Effect of lift force and hydrodynamic torque on fluidisation of non-spherical particles[J]. Chemical Engineering Science, 2019, 195: 642-656.

[156] HöLZER A, SOMMERFELD M. Lattice Boltzmann simulations to determine drag, lift and torque acting on non-spherical particles[J]. Computers & Fluids, 2009, 38(3): 572-589.

[157] RICHTER A, NIKRITYUK P A. New correlations for heat and fluid flow past ellipsoidal and cubic particles at different angles of attack[J]. Powder Technology, 2013, 249: 463-474.

[158] OUCHENE R, KHALIJ M, TANIèRE A, ARCEN B. Drag, lift and torque coefficients for ellipsoidal particles: From low to moderate particle Reynolds

numbers[J]. Computers & Fluids, 2015, 113: 53-64.

[159] OUCHENE R, KHALIJ M, ARCEN B, TANIèRE A. A new set of correlations of drag, lift and torque coefficients for non-spherical particles and large Reynolds numbers[J]. Powder Technology, 2016, 303: 33-43.

[160] BUCHALTER B J, BRADLEY R M. Orientational order in random packings of ellipses[J]. Physical Review A, 1992, 46(6): 3046-3056.

[161] VILLARRUEL F X, LAUDERDALE B E, MUETH D M, JAEGER H M. Compaction of rods: relaxation and ordering in vibrated, anisotropic granular material[J]. Physical Review E, 2000, 61(6): 6914.

[162] ZITOUN K B, SASTRY S K, GUEZENNEC Y. Investigation of three dimensional interstitial velocity, solids motion, and orientation in solid–liquid flow using particle tracking velocimetry[J]. International Journal of Multiphase Flow, 2001, 27(8): 1397-1414.

[163] MOR R, GOTTLIEB M, MONDY L A, GRAHAM A L. Effect of surfaces on the static distribution of orientations in suspensions of rod-like particles[J]. Journal of Rheology, 2003, 47(1): 19-35.

[164] STOKELY K, DIACOU A, FRANKLIN S V. Two-dimensional packing in prolate granular materials[J]. Physical Review E, 2003, 67(5): 051302.

[165] LUMAY G, VANDEWALLE N. Compaction of anisotropic granular materials: experiments and simulations[J]. Physical Review E, 2004, 70(5): 051314.

[166] MARTINEZ-RATON Y, VELASCO E, MEDEROS L. Orientational ordering in hard rectangles: The role of three-body correlations[J]. The Journal of Chemical Physics, 2006, 125(1): 014501.

[167] ARANSON I S, VOLFSON D, TSIMRING L S. Swirling motion in a system of vibrated elongated particles[J]. Physical Review E, 2007, 75(5): 051301.

[168] KU X-K, LIN J-Z. Motion and orientation of cylindrical and cubic particles in pipe flow with high concentration and high particle to pipe size ratio[J]. Journal of Zhejiang University-SCIENCE A, 2008, 9(5): 664-671.

[169] LUNDELL F, CARLSSON A. Heavy ellipsoids in creeping shear flow: transitions of the particle rotation rate and orbit shape[J]. Physical Review E, 2010, 81(1): 016323.

[170] MARCHIOLI C, FANTONI M, SOLDATI A. Orientation, distribution, and deposition of elongated, inertial fibers in turbulent channel flow[J]. Physics of Fluids, 2010, 22(3): 033301.

[171] DELANEY G W, HILTON J E, CLEARY P W. Defining random loose packing for nonspherical grains[J]. Physical Review E, 2011, 83(5): 051305.

[172] OSCHMANN T, HOLD J, KRUGGEL-EMDEN H. Numerical investigation of mixing and orientation of non-spherical particles in a model type fluidized

bed[J]. Powder Technology, 2014, 258: 304-323.

[173] CAI J, PENG Z, WU C, ZHAO X, YUAN Z, MOGHTADERI B, DOROODCHI E. Numerical study of the orientation of cylindrical particles in a circulating fluidized bed[J]. Industrial & Engineering Chemistry Research, 2016, 55(50): 12806-12817.

[174] BUIST K A, JAYAPRAKASH P, KUIPERS J A M, DEEN N G, PADDING J T. Magnetic particle tracking for nonspherical particles in a cylindrical fluidized bed[J]. AIChE Journal, 2017, 63(12): 5335-5342.

[175] LI X, JIANG M, HUANG Z, ZHOU Q. Effect of particle orientation on the drag force in random arrays of oblate ellipsoids in low-Reynolds-number flows[J]. AIChE Journal, 2020, 65(8): e16621.

[176] SHRESTHA S, KUANG S B, YU A B, ZHOU Z Y. Orientation of spheroidal particles in single jet bubbling fluidized beds[J]. Powder Technology, 2020, 361: 363-373.

[177] ROMERO-VALLE M A, GONIVA C, NIRSCHL H. Modeling of non-spherical particle flows: Movement and orientation behavior[J]. Powder Technology, 2021, 382: 351-363.

[178] SANJEEVI S K P, PADDING J T. On the orientational dependence of drag experienced by spheroids[J]. Journal of Fluid Mechanics, 2017, 820: R1.

[179] CAI J, ZHAO X, LI Q, YUAN Z. Number concentration of cylindrical particles in a fluidized bed[J]. Chinese Journal of Chemical Engineering, 2013, 21(1): 94-103.

[180] HIDALGO R C, ZURIGUEL I, MAZA D, PAGONABARRAGA I. Granular packings of elongated faceted particles deposited under gravity[J]. Journal of Statistical Mechanics: Theory and Experiment, 2010, 2010(06): P06025.

[181] MA H, ZHAO Y, CHENG Y. CFD-DEM modeling of rod-like particles in a fluidized bed with complex geometry[J]. Powder Technology, 2019, 344: 673-683.

[182] MA H, ZHAO Y. CFD-DEM investigation of the fluidization of binary mixtures containing rod-like particles and spherical particles in a fluidized bed[J]. Powder Technology, 2018, 336: 533-545.

[183] YAN S-N, WANG T-Y, TANG T-Q, REN A-X, HE Y-R. Simulation on hydrodynamics of non-spherical particulate system using a drag coefficient correlation based on artificial neural network[J]. Petroleum Science, 2019, 17(2): 537-555.

[184] YANG S, HU S, ZHANG W. Mixing and dispersion behaviours of ellipsoid particles in a bubbling fluidized bed[J]. Powder Technology, 2022, 396: 210-223.

[185] LIU R, ZHOU Z, XIAO R, YU A. CFD-DEM modelling of mixing of granular materials in multiple jets fluidized beds[J]. Powder Technology, 2020, 361: 315-325.

[186] FOTOVAT F, CHAOUKI J, BERGTHORSON J. Distribution of large biomass particles in a sand-biomass fluidized bed: Experiments and modeling[J]. AIChE Journal, 2014, 60(3): 869-880.

[187] FOTOVAT F, ANSART R, HEMATI M, SIMONIN O, CHAOUKI J. Sand-assisted fluidization of large cylindrical and spherical biomass particles: Experiments and simulation[J]. Chemical Engineering Science, 2015, 126: 543-559.

[188] CHEN X, ZHONG W, HEINDEL T J. Using stereo XPTV to determine cylindrical particle distribution and velocity in a binary fluidized bed[J]. AIChE Journal, 2018, 65(2): 520-535.

[189] REN A-X, WANG T-Y, TANG T-Q, HE Y-R. Non-spherical particle mixing behaviors by spherical inert particles assisted in a fluidized bed[J]. Petroleum Science, 2019, 17(2): 509-524.

[190] REN B, ZHONG W, JIN B, SHAO Y, YUAN Z. Numerical simulation on the mixing behavior of corn-shaped particles in a spouted bed[J]. Powder Technology, 2013, 234: 58-66.

[191] BINDAL A K, DAS A, DAS A. Study on effect of particle shape on interlocking[C]. Advances in Computer Methods and Geomechanics: IACMAG Symposium 2019 Volume 2, 2020 : 455-466.

[192] YANG R Y, ZOU R P, YU A B. Computer simulation of the packing of fine particles[J]. Physical Review E, 2000, 62(3): 3900.

[193] BLOUWOLFF J, FRADEN S. The coordination number of granular cylinders[J]. Europhysics Letters, 2006, 76(6): 1095-1101.

[194] WOUTERSE A, WILLIAMS S R, PHILIPSE A P. Effect of particle shape on the density and microstructure of random packings[J]. Journal of Physics: Condensed Matter, 2007, 19(40): 406215.

[195] FU Y, XI Y, CAO Y, WANG Y. X-ray microtomography study of the compaction process of rods under tapping[J]. Physical Review E, 2012, 85(5): 051311.

[196] NGUYEN D H, AZEMA E, RADJAI F, SORNAY P. Effect of size polydispersity versus particle shape in dense granular media[J]. Physical Review E, 2014, 90(1): 012202.

[197] GAN J Q, ZHOU Z Y, YU A B. Micromechanical analysis of flow behaviour of fine ellipsoids in gas fluidization[J]. Chemical Engineering Science, 2017, 163: 11-26.

[198] ZHAO J, LI S, ZOU R, YU A. Dense random packings of spherocylinders[J].

Soft Matter, 2012, 8(4): 1003-1009.

[199] AOSHIMA M, SATOH A. Two-dimensional Monte Carlo simulations of a colloidal dispersion composed of rod-like ferromagnetic particles in the absence of an applied magnetic field[J]. Journal of colloid and interface science, 2006, 293(1): 77-87.

[200] KANZAKI T, HIDALGO R C, MAZA D, PAGONABARRAGA I. Cooling dynamics of a granular gas of elongated particles[J]. Journal of Statistical Mechanics-Theory and Experiment, 2010, 2010(06): P06020.

[201] DENG X L, DAVé R N. Dynamic simulation of particle packing influenced by size, aspect ratio and surface energy[J]. Granular Matter, 2013, 15(4): 401-415.

[202] KANTOROVICH S, PYANZINA E, SCIORTINO F. The influence of shape anisotropy on the microstructure of magnetic dipolar particles[J]. Soft Matter, 2013, 9(29): 6594-6603.

[203] PYANZINA E S, KANTOROVICH S S, DE MICHELE C. Nematic phase characterisation of the self-assembling sphere-cylinders based on the theoretically calculated RDFs[J]. The European Physical Journal E, 2015, 38(7): 1-6.

[204] GAN J Q, YU A B, ZHOU Z Y. DEM simulation on the packing of fine ellipsoids[J]. Chemical Engineering Science, 2016, 156: 64-76.

[205] GAO Y, FARKAS V, DULLENS R P A, AARTS D. Structural disorder, filament growth and self-poisoning in short rods confined onto a flat wall[J]. Soft Matter, 2017, 13(46): 8678-8683.

[206] GONZALEZ-PINTO M, BORONDO F, MARTINEZ-RATON Y, VELASCO E. Clustering in vibrated monolayers of granular rods[J]. Soft Matter, 2017, 13(14): 2571-2582.

[207] WALSH L, MENON N. Ordering and dynamics of vibrated hard squares[J]. Journal of Statistical Mechanics: Theory and Experiment, 2016, 2016(8): 083302.

[208] SáNCHEZ R, AGUIRRE-MANZO L A. Concentric tetratic orientational order in a confined quasi-2D tubular system[J]. Physica Scripta, 2015, 90(9): 095002.

[209] HIDALGO R C, KADAU D, KANZAKI T, HERRMANN H J. Granular packings of cohesive elongated particles[J]. Granular Matter, 2011, 14(2): 191-196.

[210] HIDALGO R C, ZURIGUEL I, MAZA D, PAGONABARRAGA I. Role of particle shape on the stress propagation in granular packings[J]. Physical Review Letters, 2009, 103(11): 118001.

[211] GENG J, SELINGER J V. Theory and simulation of two-dimensional nematic and tetratic phases[J]. Physical Review E, 2009, 80(1): 011707.

[212] NARAYAN V, MENON N, RAMASWAMY S. Nonequilibrium steady states in a vibrated-rod monolayer: tetratic, nematic, and smectic correlations[J]. Journal of Statistical Mechanics: Theory and Experiment, 2006, 2006(01): P01005-P01005.

[213] DONEV A, BURTON J, STILLINGER F H, TORQUATO S. Tetratic order in the phase behavior of a hard-rectangle system[J]. Physical Review B, 2006, 73(5): 054109.

[214] ZHANG W, THOMPSON K E, REED A H, BEENKEN L. Relationship between packing structure and porosity in fixed beds of equilateral cylindrical particles[J]. Chemical Engineering Science, 2006, 61(24): 8060-8074.

[215] BLAAK R, FRENKEL D, MULDER B M. Do cylinders exhibit a cubatic phase?[J]. The Journal of Chemical Physics, 1999, 110(23): 11652-11659.

[216] HAMID A, ARSHAD A B, MEHDI S, QASIM M D, ULLAH A, MOLINA J J, YAMAMOTO R. A numerical study of sedimentation of rod like particles using smooth profile method[J]. International Journal of Multiphase Flow, 2020, 127: 103263.

[217] JALALINEJAD F, BI X T, GRACE J R. Effect of electrostatics on interaction of bubble pairs in a fluidized bed[J]. Advanced Powder Technology, 2015, 26(1): 329-334.

[218] SUNDARESAN S. Instabilities in fluidized beds[J]. Annual Review of Fluid Mechanics, 2003, 35(1): 63-88.

[219] YANG N, WANG W, GE W, LI J. Choosing structure-dependent drag coefficient in modeling gas-solid two-phase flow[J]. China Particuology, 2003, 1(1): 38-41.

[220] BUSCIGLIO A, VELLA G, MICALE G, RIZZUTI L. Analysis of the bubbling behaviour of 2D gas solid fluidized beds: Part I. Digital image analysis technique[J]. Chemical Engineering Journal, 2008, 140(1-3): 398-413.

[221] BUSCIGLIO A, VELLA G, MICALE G, RIZZUTI L. Analysis of the bubbling behaviour of 2D gas solid fluidized beds Part II. Comparison between experiments and numerical simulations via Digital Image Analysis Technique[J]. Chemical Engineering Journal, 2009, 148(1): 145-163.

[222] NIEUWLAND J J, VEENENDAAL M L, KUIPERS J A M, VAN SWAAIJ W P M. Bubble formation at a single orifice in gas-fluidised beds[J]. Chemical Engineering Science, 1996, 51(17): 4087-4102.

[223] OLAOFE O O, VAN DER HOEF M A, KUIPERS J A M. Bubble formation at a single orifice in a 2D gas-fluidized bed[J]. Chemical Engineering Science, 2011, 66(12): 2764-2773.

[224] LU Y, HUANG J, ZHENG P. A CFD–DEM study of bubble dynamics in

fluidized bed using flood fill method[J]. Chemical Engineering Journal, 2015, 274: 123-131.

[225] HE Y, YAN S, WANG T, JIANG B, HUANG Y. Hydrodynamic characteristics of gas-irregular particle two-phase flow in a bubbling fluidized bed: An experimental and numerical study[J]. Powder Technology, 2016, 287: 264-276.

[226] SHRESTHA S, KUANG S, YU A, ZHOU Z. Bubble dynamics in bubbling fluidized beds of ellipsoidal particles[J]. AIChE Journal, 2019, 65(11): e16736.

[227] SHRESTHA S, KUANG S, YU A, ZHOU Z. Particle shape effect on bubble dynamics in central air jet pseudo-2D fluidized beds: A CFD-DEM study[J]. Chemical Engineering Science, 2019, 201: 448-466.

[228] ESGANDARI B, GOLSHAN S, ZARGHAMI R, SOTUDEH-GHAREBAGH R, CHAOUKI J. CFD-DEM analysis of the spouted fluidized bed with non-spherical particles[J]. The Canadian Journal of Chemical Engineering, 2021, 99(11): 2303-2319.

[229] REN A, TANG T, HE Y. Evolution of mesoscale structure in fluidized beds with non-spherical dry and wet particles[J]. Advanced Powder Technology, 2022, 33(11): 103794.

[230] JOHN B S, JUHLIN C, ESCOBEDO F A. Phase behavior of colloidal hard perfect tetragonal parallelepipeds[J]. The Journal of Chemical Physics, 2008, 128(4): 044909.

[231] TORQUATO S, STILLINGER F H. Jammed hard-particle packings: From Kepler to Bernal and beyond[J]. Reviews of Modern Physics, 2010, 82(3): 2633-2672.

[232] YU A B. Discrete element method: An effective way for particle scale research of particulate matter[J]. Engineering Computations, 2004, 21(2/3/4): 205-214.

[233] STEINHARDT P J, NELSON D R, RONCHETTI M. Bond-orientational order in liquids and glasses[J]. Physical Review B, 1983, 28(2): 784-805.

[234] VEERMAN J A, FRENKEL D. Phase behavior of disklike hard-core mesogens[J]. Physical Review A, 1992, 45(8): 5632-5648.

[235] LIU L, LU P, MENG L, JIN W, LI S. Order metrics and order maps of octahedron packings[J]. Physica A: Statistical Mechanics and its Applications, 2016, 444: 870-882.

[236] ZHONG W, JIN B, ZHANG Y, WANG X, ZHANG M, XIAO R. Description of Dynamic Behavior of a Fluidized Bed with Biomass Fuels by Shannon Entropy Increment Analysis[J]. Energy & Fuels, 2009, 23(6): 3167-3171.

[237] GELDART D. Gas Fluidization Technology[M]. first. New York: Wiley & Son, 1986.

[238] KUNII D, LEVENSPIEL O. Fluidization Engineering[M]. second. Boston:

Butterworth-Heinemann, 1991.

[239] PENG Y, FAN L T. Hydrodynamic characteristics of fluidization in liquid-solid tapered beds[J]. Chemical Engineering Science, 1997, 52(14): 2277-2290.

[240] LIM K, ZHU J, GRACE J. Hydrodynamics of gas-solid fluidization[J]. International Journal of Multiphase Flow, 1995, 21: 141-193.

[241] JIANG Y, GUO Y, YU Z, HUA X, LIN J, WASSGREN C R, CURTIS J S. Discrete element method–computational fluid dynamics analyses of flexible fibre fluidization[J]. Journal of Fluid Mechanics, 2021, 910.

[242] WANG D G, SINGH SADHAL S, CAMPBELL C S. Particle rotation as a heat transfer mechanism[J]. International Journal of Heat and Mass Transfer, 1989, 32(8): 1413-1423.

[243] WU X, WANG Q, LUO Z, FANG M, CEN K. Theoretical and experimental investigations on particle rotation speed in CFB riser[J]. Chemical Engineering Science, 2008, 63(15): 3979-3987.

[244] GONIVA C, KLOSS C, DEEN N G, KUIPERS J A M, PIRKER S. Influence of rolling friction on single spout fluidized bed simulation[J]. Particuology, 2012, 10(5): 582-591.

[245] ROUYER F, MENON N. Velocity fluctuations in a homogeneous 2D granular gas in steady state[J]. Physical Review Letters, 2000, 85(17): 3676-3679.

[246] VAN ZON J S, MACKINTOSH F C. Velocity distributions in dissipative granular gases[J]. Physical Review Letters, 2004, 93(3): 038001.

[247] HARTH K, KORNEK U, TRITTEL T, STRACHAUER U, HOME S, WILL K, STANNARIUS R. Granular gases of rod-shaped grains in microgravity[J]. Physical Review Letters, 2013, 110(14): 144102.

[248] YU P, SCHROTER M, SPERL M. Velocity Distribution of a Homogeneously Cooling Granular Gas[J]. Physical Review Letters, 2020, 124(20): 208007.

[249] LUNGU M, WANG H, WANG J, YANG Y, CHEN F. Two-fluid model simulations of the national energy technology laboratory bubbling fluidized bed challenge problem[J]. Industrial & Engineering Chemistry Research, 2016, 55(17): 5063-5077.

[250] CODY G D, GOLDFARB D J, STORCH G V, NORRIS A N. Particle granular temperature in gas fluidized beds[J]. Powder Technology, 1996, 87(3): 211-232.

[251] CAMPBELL C S. Granular material flows-An overview[J]. Powder Technology, 2006, 162(3): 208-229.

[252] WANG T, HE Y, KIM D R. Granular temperature and rotational characteristic analysis of a gas–solid bubbling fluidized bed under different gravities using discrete hard sphere model[J]. Powder Technology, 2015, 271: 35-48.

[253] JIANG Z, HAGEMEIER T, BüCK A, TSOTSAS E. Experimental

measurements of particle collision dynamics in a pseudo-2D gas-solid fluidized bed[J]. Chemical Engineering Science, 2017, 167: 297-316.

[254] JUNG J, GIDASPOW D, GAMWO I K. Measurement of two kinds of granular temperatures, stresses, and dispersion in bubbling beds[J]. Industrial & Engineering Chemistry Research, 2005, 44(5): 1329-1341.

[255] CAHYADI A, ANANTHARAMAN A, YANG S, KARRI S B R, FINDLAY J G, COCCO R A, CHEW J W. Review of cluster characteristics in circulating fluidized bed (CFB) risers[J]. Chemical Engineering Science, 2017, 158: 70-95.

[256] HORIO M, CLIFT R. A note on terminology-clusters and agglomerates[J]. Powder Technology, 1992, 70(3): 196-196.

[257] COCCO R, SHAFFER F, HAYS R, REDDY KARRI S B, KNOWLTON T. Particle clusters in and above fluidized beds[J]. Powder Technology, 2010, 203(1): 3-11.

[258] RAKOTONIRINA A D, DELENNE J-Y, RADJAI F, WACHS A. Grains3D, a flexible DEM approach for particles of arbitrary convex shape—Part III: extension to non-convex particles modelled as glued convex particles[J]. Computational Particle Mechanics, 2018, 6(1): 55-84.

[259] CLEARY P W. The effect of particle shape on simple shear flows[J]. Powder Technology, 2008, 179(3): 144-163.

[260] HUILIN L, QIAOQUN S, YURONG H, YONGLI S, DING J, XIANG L. Numerical study of particle cluster flow in risers with cluster-based approach[J]. Chemical Engineering Science, 2005, 60(23): 6757-6767.

[261] HORIO M, KUROKI H. Three-dimensional flow visualization of dilutely dispersed solids in bubbling and circulating fluidized beds[J]. Chemical Engineering Science, 1994, 49(15): 2413-2421.

[262] DONEV A, CISSE I, SACHS D, VARIANO E A, STILLINGER F H, CONNELLY R, TORQUATO S, CHAIKIN P M. Improving the density of jammed disordered packings using ellipsoids[J]. Science, 2004, 303(5660): 990-993.

[263] CHAIKIN P M, DONEV A, MAN W, STILLINGER F H, TORQUATO S. Some observations on the random packing of hard ellipsoids[J]. Industrial & Engineering Chemistry Research, 2006, 45(21): 6960-6965.

[264] SMITH W O, FOOTE P D, BUSANG P F. Packing of homogeneous spheres[J]. Physical Review, 1929, 34(9): 1271-1274.

[265] ONSAGER L. The effects of shape on the interaction of colloidal particles[J]. Annals of the New York Academy of Sciences, 1949, 51(4): 627-659.

[266] GAN J, YU A. DEM simulation of the packing of cylindrical particles[J]. Granular Matter, 2020, 22: 1-19.

[267] ASTE T, SAADATFAR M, SAKELLARIOU A, SENDEN T J. Investigating the geometrical structure of disordered sphere packings[J]. Physica A: Statistical Mechanics and its Applications, 2004, 339(1-2): 16-23.

[268] WU Y, AN X, YU A B. DEM simulation of cubical particle packing under mechanical vibration[J]. Powder Technology, 2017, 314: 89-101.

[269] GIDASPOW D, HUILIN L. Equation of state and radial distribution functions of FCC particles in a CFB[J]. AIChE Journal, 1998, 44(2): 279-293.

[270] FRENKEL D. Order through entropy[J]. Nature Materials, 2015, 14(1): 9-12.

[271] W. W K, FRENKEL D. Tetratic phase in the planar hard square system?[J]. Computational Methods in Science and Technology, 2004, 10(2): 235-255.

[272] ZHAO K, HARRISON C, HUSE D, RUSSEL W B, CHAIKIN P M. Nematic and almost-tetratic phases of colloidal rectangles[J]. Physical Review E, 2007, 76(4): 040401.

[273] MULLER T, DE LAS HERAS D, REHBERG I, HUANG K. Ordering in granular-rod monolayers driven far from thermodynamic equilibrium[J]. Physical Review E, 2015, 91(6): 062207.

[274] WANG W, LU B, GENG J, LI F. Mesoscale drag modeling: a critical review[J]. Current Opinion in Chemical Engineering, 2020, 29: 96-103.

[275] TIAN Y, LU B, LI F, WANG W. A steady-state EMMS drag model for fluidized beds[J]. Chemical Engineering Science, 2020, 219: 115616.

[276] GENG J, TIAN Y, WANG W. Exploring a unified EMMS drag model for gas-solid fluidization[J]. Chemical Engineering Science, 2022, 251: 117444.

[277] TIAN Y J, GENG J W, WANG W. On the choice of mesoscale drag markers[J]. AIChE Journal, 2022, 68(4): e17558.

[278] BASURTO E, GURIN P, VARGA S, ODRIOZOLA G. Ordering, clustering, and wetting of hard rods in extreme confinement[J]. Physical Review Research, 2020, 2(1): 013356.

[279] SUN X, KOB W, BLUMENFELD R, TONG H, WANG Y, ZHANG J. Friction-Controlled Entropy-Stability Competition in Granular Systems[J]. Physical Review Letters, 2020, 125(26): 268005.

[280] SHARMA A K, TUZLA K, MATSEN J, CHEN J C. Parametric effects of particle size and gas velocity on cluster characteristics in fast fluidized beds[J]. Powder Technology, 2000, 111(1-2): 114-122.

[281] MANYELE S. Characterizing particle aggregates in a high-density and high-flux CFB riser[J]. Chemical Engineering Journal, 2002, 88(1-3): 151-161.

[282] WARDAG A N K, LARACHI F. Bubble behavior in corrugated-wall bubbling fluidized beds-Experiments and CFD simulations[J]. AIChE Journal, 2012, 58(7): 2045-2057.

[283] SMOLDERS K, BAEYENS J. Gas fluidized beds operating at high velocities: a critical review of occurring regimes[J]. Powder Technology, 2001, 119(2-3): 269-291.

[284] WANG J, VAN DER HOEF M A, KUIPERS J A M. The role of scale resolution versus inter-particle cohesive forces in two-fluid modeling of bubbling fluidization of Geldart A particles[J]. Chemical Engineering Science, 2011, 66(18): 4229-4240.

[285] ZHANG C, ZHAO S, ZHAO J, ZHOU X. Three-dimensional Voronoi analysis of realistic grain packing: An XCT assisted set Voronoi tessellation framework[J]. Powder Technology, 2021, 379: 251-264.

[286] ZHAO S, ZHAO J, GUO N. Universality of internal structure characteristics in granular media under shear[J]. Physical Review E, 2020, 101(1): 012906.

[287] ZHAO S, EVANS T M, ZHOU X. Three-dimensional Voronoi analysis of monodisperse ellipsoids during triaxial shear[J]. Powder Technology, 2018, 323: 323-336.

[288] TIAN Z, CHENG Y, LI X, WANG L. Bubble shape and rising velocity in viscous liquids at high temperature and pressure[J]. Experimental Thermal and Fluid Science, 2019, 102: 528-538.

[289] BAI T, SUN Z, GUO Z, ZHU J, BARGHI S. Bubble dynamics in a binary Gas-Solid fluidization system of Geldart B and Geldart D particles[J]. Chemical Engineering Science, 2022, 258.

[290] OKHOVAT-ALAVIAN S M, BEHIN J, MOSTOUFI N. Investigating bubble dynamics in a semi-cylindrical gas-solid fluidized bed[J]. Powder Technology, 2020, 370: 129-136.

[291] VERMA V, PADDING J T, DEEN N G, KUIPERS J A M. Bubble formation at a central orifice in a gas–solid fluidized bed predicted by three-dimensional two-fluid model simulations[J]. Chemical Engineering Journal, 2014, 245: 217-227.

[292] ZHOU Y, XU J, ZHU J. Different bubble behaviors in gas-solid fluidized bed of Geldart group A and group C+ particles[J]. Powder Technology, 2021, 384: 431-441.

[293] D D R L R D J H. Bubble growth due to coalescence in fluidised beds[J]. Transactions of the Institution of Chemical Engineers, 1977, 55(4): 274-280.

[294] ROWE P N. Prediction of bubble size in a gas fluidised bed[J]. Chemical Engineering Science, 1976, 31(4): 285-288.

[295] LIM K S, AGARWAL P K. Conversion of pierced lengths measured at a probe to bubble size measures: An assessment of the geometrical probability approach and bubble shape models[J]. Powder Technology, 1990, 63(3): 205-219.

[296] CAICEDO G R, MARQUéS J J P, RUíZ M G A, SOLER J G. A study on the

behaviour of bubbles of a 2D gas–solid fluidized bed using digital image analysis[J]. Chemical Engineering and Processing: Process Intensification, 2003, 42(1): 9-14.

[297] YANG S, WANG H, WEI Y, HU J, CHEW J W. Numerical investigation of bubble dynamics during biomass gasification in a bubbling fluidized bed[J]. ACS Sustainable Chemistry & Engineering, 2019, 7(14): 12288-12303.

[298] ZHANG R, KU X, LUO K, LIN J. Bubble Dynamics and Particle Orientation in a Binary Fluidized Bed Containing Spherocylinders and Spheres[J]. Industrial & Engineering Chemistry Research, 2022, 61(30): 11209-11225.

Acknowledgments

As I write this thesis, I have come to the realization that my doctoral studies are coming to an end, I would like to express my sincere gratitude to all those who have provided invaluable assistance and support during this period.

First and foremost, I would like to express my deepest gratitude to my supervisors, Professor Wei Wang, Professor Tomohiko Furuhata, and Associate Professor Yanpei Chen, for their invaluable guidance, encouragement, and support throughout the course of my research. Without their expertise, patience, I would not have been able to complete this thesis.

I would like to thank laboratory members, Dr. Renshui Zhu, Dr. Zhuo Yang, , Dr. Xing Zhao, Dr. Qingzhan Li, Dr. Jingwei Geng, Dr. Chunhua Zhang, Dr. Chenyang Sun, Mr. Chengzhe Du, Mr. Yadong Wang, Miss Mengjie Yang, Miss Wenya Zhou, and other laboratory colleagues for their kind help. The company of these students has brought color and vibrancy to my otherwise monotonous experimental life.

I would also like to thank the faculty and staff of Institute of Process Engineering, Chinese and Academy of Sciences and Gunma Universituy, for providing a stimulating and supportive environment for my academic pursuits. The resources and opportunities offered by these department have been invaluable in helping me achieve my goals.

Finally, I am grateful to my parents, girlfriend, and sister for their unwavering love, support, and encouragement throughout my academic journey. Their belief in me has been a constant source of motivation and inspiration, and I could not have achieved this without them.

2023.5

List of Publications

1. Zhang, C., Zhu, R., Chen, Y., Wang, W., & Furuhata, T. Configuration-dependent dynamics of non-spherical particles in a gas-solid fluidized bed[J]. Chemical Engineering Journal, 2023,465: 142969.